Developing Advanced Atomic Force Microscopy Techniques for Probing Coupled Phenomena in Functional Materials

Ehsan Nasr Esfahani

A dissertation
submitted in partial fulfillment of the
requirements for the degree of

Doctor of Philosophy

University of Washington

2018

Reading Committee:

Jiangyu Li, Chair

Stuart B. Adler

Marco Salviato

Program Authorized to Offer Degree:
Aeronautics and Astronautics

University of Washington

Abstract

Developing Advanced Atomic Force Microscopy Techniques for Probing Coupled Phenomena in Functional Materials

Ehsan Nasr Esfahani

Chair of the Supervisory Committee:
Professor Jiangyu Li
Mechanical Engineering

In the last decades, nanotechnology has built great expectations because of its unique capabilities in engineering materials with tailored properties. Exhibiting enhanced physical and chemical properties at length scale on the order of 1–10 nm, nanostructured materials have contributed more than ever, ranging from energy generation, storage, and conversion with applications in lithium ion battery electrodes, solid oxide fuel cell electrodes, thermoelectric heat recovery, and perovoskite solar cells. Recent findings suggest that the composition, structure, and properties of multifunctional materials are governed at nanoscale and are substantially different than of the bulk properties. While the chemical and phase composition of these materials can be mapped with atomic and sub-atomic resolution, the structural mappings do not provide significant information on nanoscale physical properties. Indeed, there is still a lack of techniques that can effectively probe local phenomena and link the nanoscale properties to bulk performance and microstructure of material.

Atomic Force Microscope (AFM) is a versatile tool for imaging, measurements, and manipulation of matter with nanometer spatial resolution and picometer detection accuracy. Over the last three decades, advanced AFM modes and functionalized probes were developed and employed in magnetic and ferroelectric studies, electrochemical characterizations, viscoelastic measurements, and quantum transport imaging. Despite the tremendous im-

provements in AFM platforms, functionalized probes, and imaging techniques, AFM measurements are not without challenges. For instance, the signal formation mechanism is complex and consists of several contributions. The resonance-enhanced techniques used for intrinsic characterization of functional materials are prone to topography and feedback cross-talks and often results in unreliable measurements. Obtaining quantitative measurements that can directly link to the probed physical phenomena is a non-trivial job.

The first goal of this dissertation was to develop advanced excitation, detection, and data analysis techniques that can measure nonlinear phenomena, resolve topographic and feedback cross-talks, and extract intrinsic properties. A multi-harmonic dual resonance tracking technique is implemented on a commercial AFM system, nonlinear resonance-enhanced AFM responses are obtained, and the intrinsic properties are determined and visualized. The other developed technique is an open-loop sequential excitation that performs a series of single frequency lock-in measurement. Finally, a method based on acquisition of highly sampled time domain AFM signals was developed and implemented. Multivariate statistical analysis, such as principal component analysis (PCA), is performed on AFM data to enhance signal-to-noise ratio and statistically relevant modes of the data. The first few modes of the data contain relevant information while the rest of the modes only contain noise. The low-rank reconstructed data further analyzed via wavelet-based time-frequency analysis as well physics-based methods and intrinsic properties are revealed.

The second part of the dissertation deals with novel AFM imaging modes on the foundation of excitation and detection schemes explained in the previous part. Currently, the state-of-the-art AFM imaging modes used to characterize ferroelectric and ionic and material systems are known as piezoresponse force microscopy (PFM) and electrochemical strain microscopy (ESM). PFM and ESM are identical in implementation and are based on application of an alternating bias to the probe tip in contact with the material and measurement of the induced dynamic strain by AFM cantilever motion. It is virtually impossible to dis-

tinguish the ionic, ferroelectric, and electrostatic contributions while scanning a material. Scanning thermo-ionic microscopy (STIM) was proposed and developed by measuring the dynamic deflection induced by simultaneous oscillations of local hydrostatic stress and temperature at the probe tip. The probe tip is not charged and the signal formation originates from ionic diffusion and does not consist of piezoelectric and electrostatic effects. The signal formation mechanism was examined on an ionically conductive sample Sm-doped ceria and not ionically conductive PTFE sample. STIM was implemented using two excitation methods: resistive heating and photo-thermal excitations. Having local control on nanoscale heat transfer, a method was introduced to quantitatively measure the thermal conductivity of the sample through a combination of experimental and numerical calibration studies. Thermal conductivity can be measured with good accuracy and high spatial resolution. The method was applied on a three-phase thermoelectric sample and is a powerful tool to optimize the conversion efficiency of thermoelectric materials.

The measurements in AFM are mostly indirect as the characterization techniques are based on measurements of surface displacements that are often not accurate. Recently developed charge gradient microscopy was also used to directly characterize ferroelectric surface charge kinetics, and domain and domain wall formations. The method is based on fast scanning with high contact forces using while the current between the tip and sample is measured. It is shown that the measured current signals are proportional to AFM speed and, as opposed to conventional PFM measurements, increasing the scan speed enhances the current signals. The origin of the method is further studied by obtaining temperature-dependent currents and performing PCA analysis to enhance the SNR. The measured current was used to calculate the collected charge and estimate the polarization coefficient and surface charge density directly.

Finally, the dissertation conclusion and future works for the continuation of this work are discussed in the last chapter.

TABLE OF CONTENTS

LIST OF FIGURES

LIST OF TABLES

ACKNOWLEDGMENTS

First of all, I would like to thank my family for their unlimited support throughout all the years. I shall express my deepest gratitude to my parents without whose unconditional, selfless, and perpetual supports, I would not be even close to where I am now. Words would not be able to convey the true degree of my appreciations and thanks for their dedications.

I am deeply indebted to my advisor Prof. Jiangyu Li for his continuous support of my Ph.D. study and related research, for his patience, motivation, immense knowledge, and gracious manners.

Besides my advisor, I would like to thank the rest of my thesis committee: Prof. Stuart Adler, Prof. Lucien N. Brush, Prof. Mehran Mesbahi, Prof. Marko Salviato, and Prof. Anthony Waas for their insightful comments and encouragement. I am also deeply indebted to Late Prof. Kuen Y. Lin for his enlightening advices.

A spacial thank you to the members of the Multifunctional Material Laboratory for all the discussions and friendship during the past four years. I would also like to acknowledge UW Clean Energy Institute and Shenzhen Institutes of Advanced Technology for their financial support.

Last but not least, all my benevolent friends and people whose help sustained me with hope and passion during my studies have to be particularly thanked.

Chapter 1
INTRODUCTION

1.1 Motivation

Energy has one of the most, if not the most, profound effects on our lives, from what we wear and what we eat to the economic growth and political stability of regions. The rapid growth of human society and the tendency for living longer lives call for higher and broader sources of energy. The world energy crisis and concerns over the environmental effects have aroused a great deal of interest in developing sustainable energy systems, *i.e.*, a systems that serve needs of the present without compromising the ability of future generations to meet their needs. Renewable energy sources and technologies that are designed to improve the efficiency of energy utilization are called twin pillars of sustainable energy system.

In the last decades, nanotechnology has built great expectations because of its unique capabilities in engineering materials with tailored properties and nanostructured materials have contributed more than ever to various sustainable energy systems. Today, advanced multifunctional materials play a substantially important role in our modern society. Multifunctional materials are essentially composite materials, and the rapid growth in application of nanocomposites stemmed from multifunctional design requirements.

Despite the strong growth in production of multifunctional materials, there still lacks effective methods to characterize and measure the highly coupled transport phenomena at nanoscale. This can be illustrated by the hybrid perovskite $CH_3NH_3PbI_3$, widely pursued for the next generation of solar cells. The microscopic processes in $CH_3NH_3PbI_3$ are highly complex, involving generation, transport, and recombination of photo-carriers, ionic migration and defects, and possible polarization domain and switching, which all interact with light,

heat, and electric field as well as with each other on various time and length scales. The development of techniques to characterize multifunctional materials for use in high efficiency energy generation, storage, and recovery remains a major topic of interest in the research community.

1.2 Atomic Force Microscopy

Development of advanced functional material systems is impossible without characterization of physical, structural, and chemical properties at micro-, nano-, and atomic scales. Characterization of local electronic properties became possible after the invention of scanning tunneling microscopy (STM) by Binning and Rohrer in 1981 [5]. STM, a Nobel Prize winning technique, was based on quantum tunneling effect between sample and an atomically sharp conductive tip and was the first instrument to image surfaces with atomic resolution. In 1986, the concept of atomic force microscope (AFM) was introduced based on mechanical detection of Van der Waals forces between a micro-cantilever and sample [6]. Soon after, researchers realized that the AFM concept can be extended to map not only mechanical forces, but also electrostatic and magnetic forces. AFM was accepted as a versatile tool for concurrent probing of forces and currents with nanoscale resolution. Over the last two decades, various modes and techniques as well functionalized probes were developed for AFM. The techniques include Kelvin probe force microscopy (KPFM), electrostatic force microscopy (ESM), magnetic force microscopy (MFM), scanning thermal microscopy (SThM), conductive atomic force microscopy (cAFM), piezoelectric force microscopy (PFM) and other techniques for probing near-filed optical properties. AFM allows imaging, control and modification of materials at nanoscale and has been applied in broad spectrum of fields such chemistry, material science, life sciences and condensed matter physics.

The concept of AFM consists of three main parts: (1) an elastic micro-cantilever with a tip radius of curvature on the order of nanometers, (2) precise x-y-z positioners, and (3) a deflection detection system (Figure 1.1). While the tip is being brought into the sample surface, forces between the tip and sample result in cantilever deflection. The curvature or

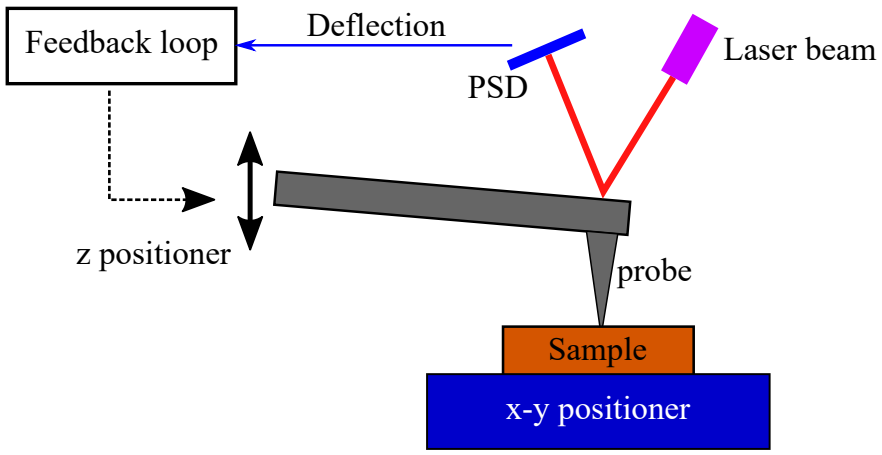

Figure 1.1: Schematic of atomic force microscope (AFM).

the displacement of the cantilever is accurately measured by an optical beam or an interferometer and converted to electrical signals. Therefore, the the cantilever deflection signal is used as AFM force sensor. Depending on the AFM mode and probe type, the deflection may be due to mechanical forces, Van der Waals forces, electrostatic forces, chemical bonding, and magnetic forces. Along with forces, additional information (*e.g.*, voltage, current, temperature) may be acquired. For AFM imaging, the tip raster scans the sample surface to obtain local information along an x-y grid. As the scan proceeds, the cantilever deflection remains constant through a feedback loop control of z positioning of the cantilever. Based on the feedback information, the height variation of sample is obtained.

The first generation of AFMs were based on detection of static signals with applications in contact mode topography scanning or scanning tunneling microscopy. The DC detection imposed severe limitations in terms of scanning time, accuracy, and resolution of signals. The dynamic AFM modes overcome these difficulties by exciting and detecting the cantilever motion at particular frequencies. Heterodyne detection approaches such as lock-in amplifier measurements are employed to extract signal information with a known carrier frequency from an extremely noisy signal. The method was successfully applied in tapping mode topography, Kelvin probe force microscopy, piezoresponse force microscopy, scanning thermoionic microscopy, electrostatic force microscopy and electrochemical strain microscopy and

continues to be used in all modern AFMs to this day.

1.3 Dynamic Strain-based SPM

In the last two decades, dynamic strain-based scanning probe microscopy has emerged as a powerful tool to investigate electromechanical and electrochemical coupling at the nanoscale. Two voltage-modulated techniques are developed based on AFM, known as piezoresponse force microscopy (PFM) for piezoelectrics and ferroelectrics, and as electrochemical strain microscopy (ESM) for electrochemical materials. These techniques work by exciting electromechanical strain of the sample via a modulated bias applied through a conductive AFM probe tip and measuring the resulted dynamic strain. These AFM techniques provided invaluable insights into nanoscale mechanisms of advanced materials and stimulated the development of nanostructure fabrication. In the next sections, a general overview of methods and mechanism are provided, scientific merits are explained and the corresponding challenges are emphasized.

1.3.1 Bias-induced Phenomena in AFM

The charged AFM probe may introduce a wide range of electromechinical and electrochemical phenomena based on the nature of material under the probe. In this section relevant physical mechanisms are reviewed.

Piezoresponse Force Microscopy

Piezoresponse force microscopy is an AFM contact mode based on the detection of the converse piezoelectric effect. Under applied electric field of probe, the piezoelectric sample may elongate, contract, or undergo shear deformation. The induced strain S_j under the electric field E_i is [7]:

$$S_j = d_{ij} E_i, \tag{1.1}$$

where d_{ij} is the third order piezoelectric tensor in Voigt notation. For a single-domain ferroelectric, polarization coefficient is linearly correlated to spontaneous polarization P_s as [8]:

$$d_{ij} = \epsilon_{im} Q_{jmk} P_{sk}, \tag{1.2}$$

where ϵ_{im} is the dielectric constant and Q_{jmk} is the electrostriction coefficient. In PFM measurements with a probe tip voltage $V_{dc}+V_{ac}cos(\omega t)$, the tip displacements D is approximated as [9]:

$$D_P = d_{eff} V_{dc} + d_{eff} V_{ac} \cos(\omega t + \phi) \tag{1.3}$$

where D_P is the AFM tip displacements due to the piezoelectric effect, d_{eff} is the the effective converse piezoelectric coefficient of the sample, ω is the frequency of excitation, and ϕ is the phase lag of deflection signal with respect to the excitation. The AC component of piezoelectric displacement is correlated to d_{eff}, while the phase of displacement ϕ reflects the piezoelectric coefficients of opposite sign and thus proportional to the direction of the domain polarization. The elctromechanical response to the applied tip bias is a vector having three independent components. Detection of vertical and lateral components of cantilever motion in successive scans and orientation of sample ideally allow for determination of qualitative piezoelectric properties.

PFM can be also used to control and modify ferroelectric materials at nanoscale. In early 2000, researchers showed that bias pulses applied to the probe tip result in nucleation and growth of ferroelectric domains [10]. The emergence of remnant states was explored both analytically and via phase field modeling [11, 12]. Switching Spectroscopy PFM (SS-PFM) was introduced [13], where a triangular DC bias waveform is applied to the probe to coercively switch the domain polarization orientation while the superposed AC bias is used to measures the instantaneous piezoelectric magnitude and orientation. In order to minimize electrostatic interactions between the charged probe and sample and PFM amplitude, the instantaneous PFM amplitudes are measured and averaged in short periods when the DC bias is stepped back to zero (off-state). The resulted hysteresis loops were measured over a

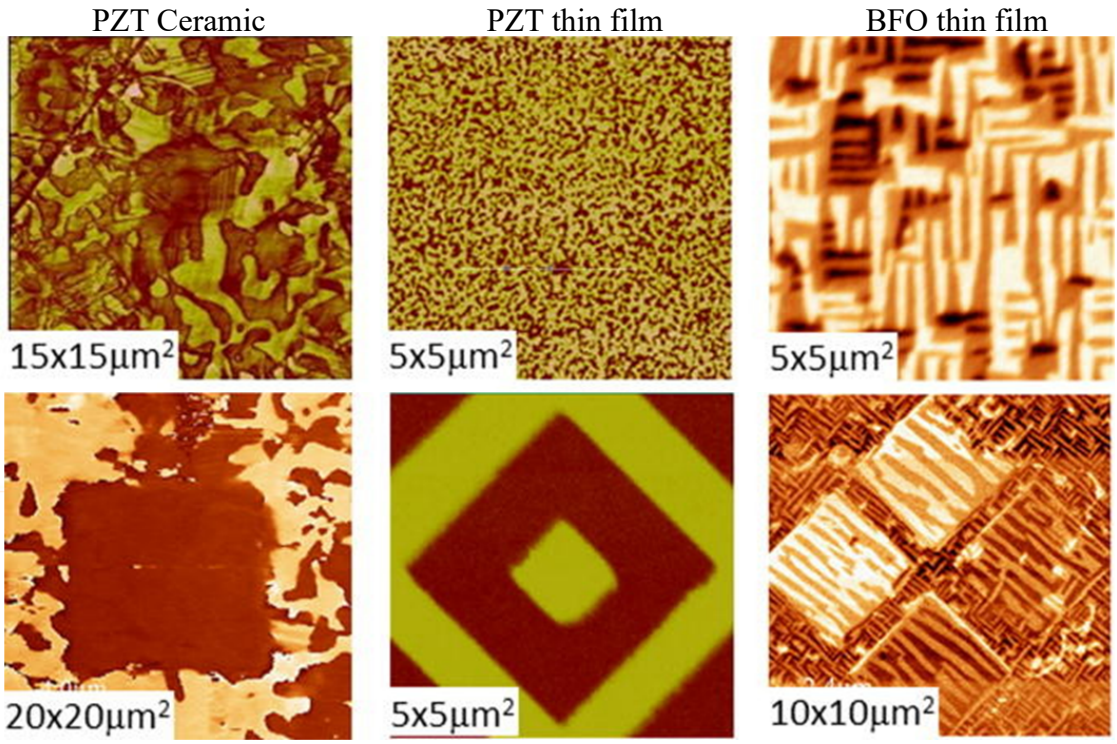

Figure 1.2: Typical applications of PFM in ferroelectric and piezoelectric materials. PFM phase images of ceramic and thin films (upper row) before manipulation and (lower row) after PFM manipulation of domains. Images reprinted from [1] .

x-y grid points and can be analyze to reveal the ferroelectric properties such as spontaneous polarization and coercive and nucleation bias.

Based on the observed contrast in PFM, several electromechanical models were proposed over the years. The models described analytical solution for a piezoelectric indentation of AFM probe [14–16], the behavior of antiparallel domains and domain walls under PFM [17, 18], dependence of PFM signals on piezoelectric domain orientation [19], and the piezoresponse spectrocopy [20]. It was observed that in some cases, the quantified displacement of the AFM probe is close (within an order of magnitude) to the longitudinal piezoelectric coefficient d_{33} of the material [10]. The ease of PFM application and the straightforward models resulted in broad application of PFM by ferroelectric community. PFM experiments revealed high-resolution imaging of ferroelectric domains in nanostrctures

of $PbZr_xTi_{1-x}O_3$ (PZT), $SrBi_2Ta_2O_9$ (SBT), $BiFeO_3$ (BFO) and $BaTiO_3$ (BTO) [21–23]. PFM was utilized to study and display polarization relaxation, domain wall motion, and domain faceting [21, 24–26]. Rodriguez *et al.* performed sequential PFM scans to obtain the vertical and lateral piezoelectric displacements and demonstrated the 3D polarization reconstruction in PZT capacitors [27]. PFM also revealed piezoelectricity in biological systems such as butterfly wings, bones, wood, and tissues [28–32]. Majority of these behavior are averaged out in macroscopic measurement, however were easily observed thanks to PFM localized measurements. Some of the results are illustrated in Figure 1.2.

Electrochemical Strain Microscopy

Electrochemical reactions such as intercalation of ions induce molar volume changes in the host compound. The coupling between species concentration and strain allows for development of strain-based AFM techniques that can probe local concentration. Recently, electrochemical strain microscopy (ESM) was proposed based on measurement of Vegard strain induced by a charged AFM tip. The method is similar to PFM in implementation, however the phenomena is based on diffusion . An alternating bias applied to the probe tip in contact with an ionically conductive material induces ionic motion, and in turn, the ionic motion results in surface displacement due to Vegard strain which can be accurately measured by AFM deflection signal.

ESM responses were modeled based on purely diffusional transport phenomena [33–35], and it was found that the surface displacement is linearly correlated to $\beta D_{ion}/\sqrt{\omega}$, where D_{ion} is the species diffusion constant, β is the Vegard coefficient, and ω is drive frequency. The characteristic time scale of diffusion phenomena is $\tau = R^2/D_{ion}$, where R is the characteristic systems size [33]. As such, high frequency excitation results in diffusion length smaller than size of tip while low frequency excitation results in diverging diffusion lengths over time and in turn ionic migration. Analogous to PFM, time- and bias-spectroscopic studies were performed to study ionic motion and ionic migration phenomena [35–38]. It is important to note that in variety of materials the induced Vegard strains is larger than the piezoresponses

and therefore it is important to consider this mechanisim where relavant [1].

Electrochemical Dipoles

The strong electric field E under the probe sharp tip results in deformation of dielectrics due to electrostrictive effect given by $\epsilon = QP^2$, where Q is electrostrictive coefficient and $P = \chi E + P_S$ is the polarization consists of induced polarization χE and spontaneous polarization P_S, and χ is the dielectric susceptibility. The strain under the probe tip is given by [2]:

$$\epsilon \propto Q(\chi^2(E_0^2 + E_a^2 \exp(i2\omega t) + 2E_0 E_a \exp(i\omega t)) + P_S^2 + 2\chi(E_0 + E_a \exp(i\omega t)P_S), \quad (1.4)$$

where E_0 and E_a are the DC and AC electric fields applied to the probe tip and ω is the frequency of excitation. During AFM measurements, the deflection response is high-pass filtered resulting in a strain in form of:

$$\epsilon \propto 2Q\chi E_{ac}(\chi E_0 + P_S) \exp(i\omega t) + Q\chi^2 E_{ac}^2 \exp(i2\omega t)). \quad (1.5)$$

Based on Equation 1.5, the resulted deformation has two harmonics. The first harmonic response (first term on RHS of Equation 1.5) is due to the piezoelectric effect and is proportional to the applied AC bias, as well as the Polarization P_S. As explained in previous section, ferroelectric materials exhibit large spontaneous polarization and the signal formation mechanism in PFM is due to this effect. However, the second term in Equation 1.5 reveals that in case of non-ferroelectric materials one can expect a second harmonic response which is quadratic to the applied AC bias. The effects is due to polarization of mobile ion sub-system which results in double layers of dipoles.

1.3.2 Resolving Different Mechanisms in AFM

AFM measurements are complex and the signals often consists of different contributions. For instance, the electromechanical response —reviewed in the previous section— may arise

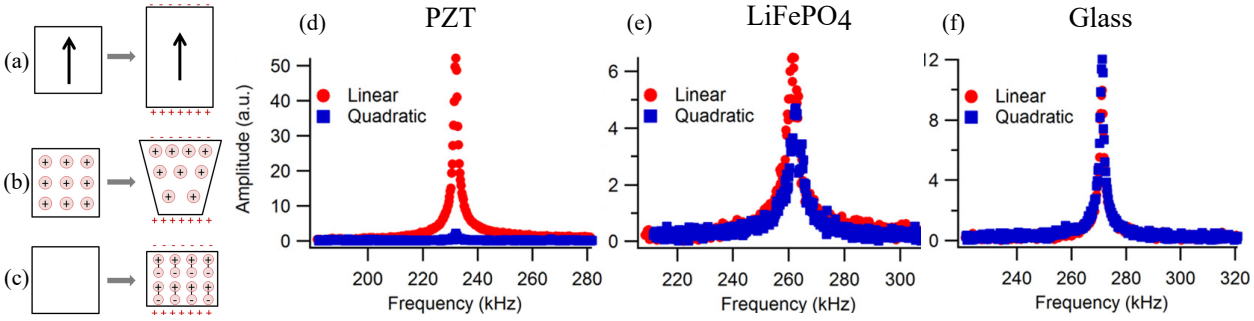

Figure 1.3: Schematic of bias induced phenomena due to (a) piezoelectric, (b) electrochemical, and (c) electrostrictive effects. The first and second harmonic of AFM deflection response on (d) PZT, (e) LFP, and (f) glass samples. The first harmonic response is dominant in piezoelectric materials while the ionic and electrostrictiv samples excibit comparable first and second harmonic responses. Images repented from [2].

due to several mechanisms. Several techniques were provided to segregate the piezoelectric contributions from electrostatic, electrochemical and electrostrctive effects.

In order to distinguish the dipole effect from the piezoelectric one, Chen *et al.* [2] performed multimodal measurements of deflection response under a charged probe tip and showed that when the spontaneous polarization is small or non-existent, the second harmonic term is dominant over the first harmonic term. Based on the proposed technique, the piezoelectric contribution can be distinguished from electrochemical and electrostrictive contributions (Figure 1.3). Another distinguished feature of ferroelectric and ionic materials is revealed by spectroscopy studies. It was observed that the shape of hysteresis loops in ionic materials are highly rate dependent while the ferroelectric materials exhibit similar hysteresis shapes under different rates [2,39]. Thus, performing voltage spectroscopy measurements with different rates can distinguish the origin of electromechanical responses.

Another technique developed by Kim *et al.* explores the frequency dependence of deflection signals [40]. Piezoelectric responses in general are not significantly dependent on excitation frequencies while the deflection responses due to ionic diffusion are highly frequency dependent. The out-of-plane strain ϵ due to induced ionic motion with a probe tip

voltage V_{ac} was found as:

$$\epsilon \propto 2(1+\nu)\beta\sqrt{D}\frac{V_{ac}}{\sqrt{\omega}}, \tag{1.6}$$

where ν is the Poisson's ratio and D is the diffusion constant. Therefore, a frequency sweep of excitation signal can distinguish between the piezoelectric and ionic origin of elecctromechanical response. It was demonstrated that the electromechanical response of PZT in the range of 10–100 kHz is frequency independent while significant dispersion was found for a ionic battery electrode material.

Over the last few years, a number of workers reported that the PFM measurements results in unrelaible estimation of d_{33} [41, 41–43]. It was realized that beside the localized piezoresponse between the tip and sample, there are additional delocalized forces. For instance, the electriostatic forces between the body of cantilever and the sample surface charges respond to the applied bias at broad range of frequencies [41, 44]. Considering the cantilever as an Euler-Bernoulli beam, the electrostatic effect acts as a distributed load over the entire span of the beam. Conventional AFM systems, measure the cantilever curvature through an optical beam deflector (OBD) and correlate the curvature to the displacement through calibration experiments. Therefore, PFM displacement measurements are very sensitive to the change of curvature and in turn to the distributed electrostatic forces that are unrelated to PFM measurements. Recently, a metrological AFM was introduced that can directly measure the cantilever displacements using a laser Doppler vibrometer (LDV) [3], eliminating the need for calibration. The idea was demonstrated by performing PFM measurements on periodically polled lithium niobate (PPLN), which exhibits ferroelctric lamellar 180° domains. Ideally, the upward and downward domains should have similar PFM amplitudes with a phase reversal of 180°. The PFM responses also should not be frequency dependent. A comparison between measured PFM responses via OBD and LDV is shown in Figure 1.4. It was demonstrated that LDV measurements of displacement over the probe tip allow for electrostatic-free and quantitative PFM measurements. Hence, the metrological AFMs are promising tools for quantitative measurements of electromechanical responses with minimal cross-talks.

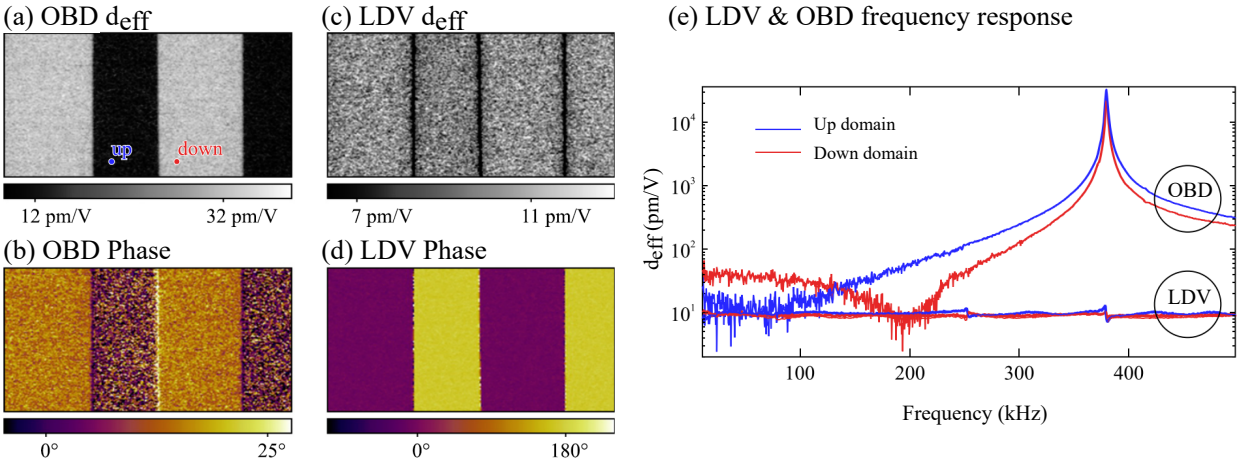

Figure 1.4: Comparison of conventional and metrological AFM. PFM amplitude (a,c) and phase (b,d) responses measured with optical beam deflector (a,b) and laser Doppler vibrometer (c,d) on a PPLN sample; (e) PFM amplitude frequency response reprinted from [3].

1.3.3 Excitation, Detection and Signal Processing in AFM

Since the electromechanical strain induced by a few volts is generally small, a common practice is to excite the system near the tip-sample contact resonance frequency ω_0, which enhances the response by orders of magnitude, enabling detection of intrinsic electromechanical displacements as small as picometers. The resonance enhanced signal is a convolution of electromechanical response and the effective tip-sample contact stiffness. Near the resonance frequency, the change in the contact condition shifts the resonance frequency and if the excitation frequency is fixed, the amplification factor is greatly changed. This may cause topography cross-talks, making the quantification of electromechanical signals complex. Note that phased-lock loop (PLL) methods cannot be used to track the resonance frequency, as the phase response depends on the domain orientation and not known in advance.

A number of different techniques were developed to address these limitations. Dual frequency resonance tracking (DFRT) [45] tracks the contact resonance by dual excitation and

measurements of the amplitude through lock-in measurements. The difference between the amplitude on two sides of the resonance peak is used as a feedback signal to track the shifts in the contact resonance. Further analysis of data based on simple harmonic oscillator model allows for extraction of Q-factor and the intrinsic amplitude (off-resonance amplitude) of cantilever oscillation as well as the resonance frequency. Later on, band excitation (BE) [46] was proposed. In BE the probe is excited by a band of selected frequencies around the contact resonance frequency. The detected cantilever motion in time domain is transformed to frequency domain, where the frequency-dependent amplitude and phase of the signal is obtained. Again, based on simple harmonic oscillator model, the Q-factor, intrinsic amplitude and resonance frequency are determined.

DFRT and BE methods allow for cross-talk free electromechanical characterization, however suffer from certain drawbacks. The lock-in amplifiers used for DFRT measurements detect the weak periodic deflection signals by demodulation and filtering through digital signal processing in real time synchronous to the AFM operation. The deflection signal from the AFM photodetector which is streamed with a bandwidth of 2–20 MHz is compressed by the lock in amplifier to 1–10 kHz. The lock-in amplifier, thus, trades off the loss of information (such as nonlinear dynamics of probe interactions, transient behaviors, higher harmonics) for higher accuracy and signal-to-noise ratio. In addition, the lock-in process is irreversible after the measurement is finished since the data is lost. Therefore, the obtained information in DFRT is limited and the post-processing analysis are based on assumption that that the resonance peak is symmetric. Also, the presence of feedback errors and dependence of amplitudes on feedback errors often result in unreliable measurements [47]. Furthermore, tracking of resonance frequency often fails when the surface roughness is high.

The BE method eliminates the need for resonance tracking, however suffers from low signal-to-noise ratio due to the spread of energy over band of excitation. The acquisition time in BE is long and the implementation requires certain instruments that are not available to all AFM users. An alternative method is developed in Section 2.5 that overcomes the problems associated with DFRT and BE by sequential excitation in a series of fast open-loop scans.

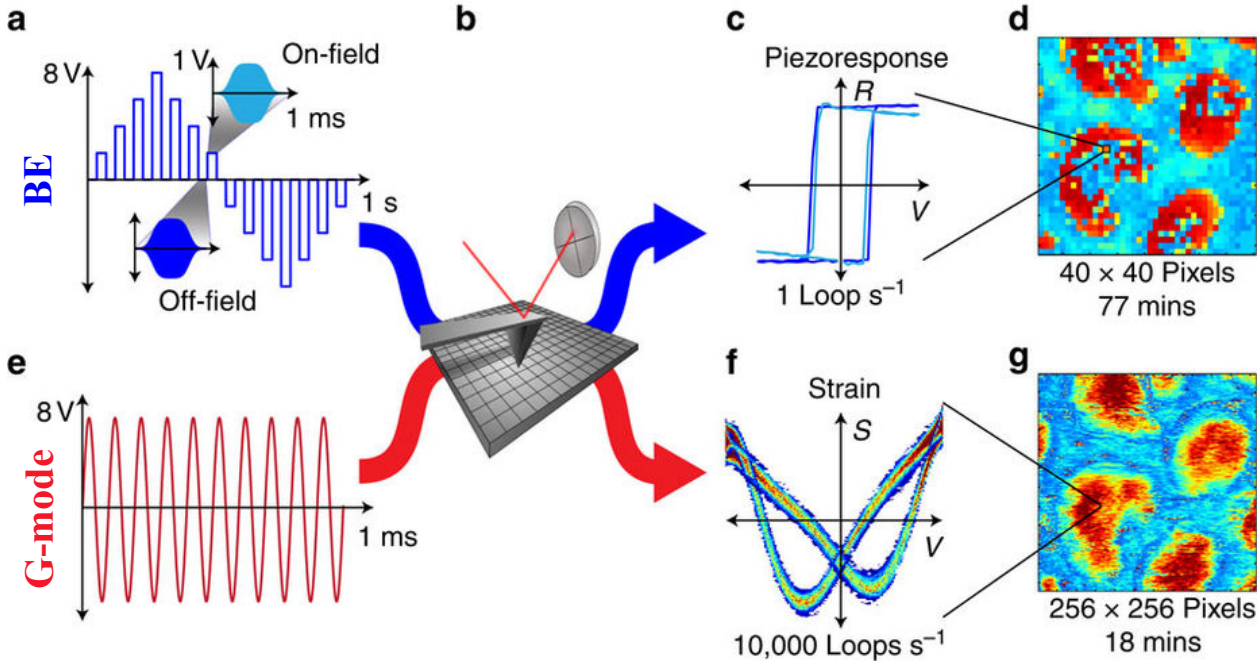

Figure 1.5: Comparison of BE and G-mode switching spectroscopy PFM. In BE a slow triangular wave induces ferroelectric switching with 1 Hz rate while in G-mode the switching is performed via a high-amplitude sinusoidal signal. The hysteresis loops are obtained via full information acquisition of cantilever deflection. Images reprinted from [4].

The main drawback in all mentioned methods is the acquisition time. This is specially important for spectroscopic studies where the measurement rates are limited by the DC switching bias frequency and are on the order of 1 Hz. Obtaining a dense map of spectroscopic information using DFRT or BE methods may take more than an hour. Recently, a method based on obtaining the full information of AFM cantilever motion with high sampling rates is developed in Oak Ridge National Lab and termed general mode scanning probe microscopy (G-mode SPM) [4, 48]. Figure 1.5 depicts an example of switching spectroscopy PFM on a PZT-nanocapacitor sample using BE and G-mode [4]. The BE performs the switching with a slow rate and obtains hysteresis loops over a sparse spatial grid in 77 minutes. In G-mode the the tip is excited with a high-amplitude sinusoidal waveform and the deflection is measured with high sampling rates in 18 minutes. Intelligent filtering of the data allows

for reconstruction of hysteresis loops over a dense spatial grid. The rich data obtained from this method can be further analyzed for ferroelectric characterizations.

1.4 Remaining Challenges

The electromechanical responses due to the piezoelectric effect and Vegard strain are fundamentally indistinguishable while a charged probe scans over a ferroelectric or an ionic conductor. This is specially the case when spontaneous polarization and ionic motion coexist in the sample. Therefore, there is an increasing need for piezoelectric and ionic characterization techniques that are not based on application of electric field to the probe tip. To this end, a novel technique based on measuring Vegard strain induced by hydrostatic stress and temperature oscillations are developed and described in Chapter 3. By elimination the bias at the tip, the strains measured via STIM are purely due to Vegard strains.

Another issue with determination of piezoelectricity through electromechanical responses is the acquisition time. A PFM scan generally takes on the order of minutes with pixel dwell times in the range of 100 μs and 10 ms, much longer than the time characteristics of ferroelectircs that are on the order of nanoseconds. As such, the surface screening and fast forming kinetics of domains and domain walls are averaged out over pixel measurements and cannot be determined. Besides, the PFM measurements are based on converse piezoelectric that is measurement of piezoelectric strain under applied electric field. It is well known in AFM community that quantifying the AFM displacements are not strightforward and faces severe problems. In order to overcome the associated problems with PFM, an alternative method based on measurements of currents is introduced in Chapter 5.

1.5 Scope of Dissertation

The dissertation covers the research materials on development of advanced AFM techniques for probing nanoscale transport phenomena for functional materials. Chapter 2 describes the development of excitation and detection schemes necessary for probing nonlinear transport phenomena in AFM characterizations. An approach for obtaining big data during AFM

measurements is developed which provides capabilities to excite, probe, acquire, and analyze multi-dimensional physical data set in time-frequency domains. The methods described here are the basis of AFM techniques developed in next chapters.

In Chapter 3 a novel technique for probing ionic concentration, scanning thermo-ionic microscopy (STIM), is developed. STIM is an outstanding method for characterization of ionic diffusion and migration in energy storage materials. The analysis, signal formation, and implementation details using various detection schemes are discussed. The technique was used to probe perovskite solar cells, battery and fuel cell electrode materials.

Chapter 4 describes the development of quantitative thermal conductivity measurements at nanoscale based on scanning thermal microscopy. The principle of the method and implementation details are explained and numerical simulation of nanoscale heat transfer are offered. Thermal and electrical conductivies of a three-phase thermoelectric material system are characterized and the effect of microstructure on thermoelectric conversion efficiency is investigated.

In Chapter 5 charge gradient microscopy (CGM), a recently developed AFM technique is utilized to image ferroelectric domains of lithium niobate based on current measured. Kinetics of screening surface charge removal is studied as a function of temperature and scan speed. The signal formation over ferroelectic domains and domain walls are used to directly estimate spontaneous polarization and surface charge density. Principal component analysis (PCA) is utilized to to enhance the signal-to-noise ratio of noisy raw data and extract the underlying mechanism in surface screening of ferroelectric materials. Finally, in Chapter 6 conclusions and future work remarks are described.

Chapter 2

RESONANCE-ENHACED AFM CANTILEVER MOTION: DETECTION SCHEMES

2.1 Introduction

Atomic Force Microscope (AFM) is a versatile instrument and a key enabler in nanoscale characterization of advanced materials. Since its invention in 1986, AFM has revolutionized local probing of a wide range of materials, devices, and systems with nanoscale resolution, and a number of imaging modes have been developed to map various physical quantities. The first generation of AFMs were mostly based on detection of static forces with applications in contact mode topography scanning or scanning tunneling microscopy [5, 49]. The DC detection imposed severe limitations in terms of scanning time, accuracy, and resolution of signals. Researchers implemented dynamic AFM modes to overcome these difficulties [50, 51]. Dynamic AFM modes utilize heterodyne detection approaches such as lock-in amplifier measurements to extract signal information with a known carrier frequency from an extremely noisy signal. To this end, researchers excited the AFM probe at a certain frequency by stimulating the material under the probe, resulting in a forced driven dynamic strain that can be accurately detected by the probe deflection. This approach has been successfully applied in tapping mode topography mode [52], Kelvin probe force microscopy [53], piezoresponse force microscopy [9], scanning thermo-ionic microscopy [54], electrostatic force microscopy [55], and electrochemical strain microscopy [56]. The method continuous to be used in all modern AFMs to this day.

While the AFM instrumentation and probe functionality were continuously developing over the last decades, the development of detection, excitation, and signal processing techniques were less recognized [57]. The majority of AFM techniques are still based on first

harmonic measurements of single or a few spectral frequency components, which do not adequately capture the complex dynamics of the probe tip-surface interactions. Multi-frequency excitation, feedback-based, band excitation (BE) and generalized mode (G-mode), and intermodulation detection approaches have been proposed [46, 48, 58–61]. However, decoding the information and correlating the obtained data with material properties remain a challenge. Furthermore, vast majority of the current techniques obtain and analyze the information based on *a-priori* postulated physical models [62]. It is still unknown whether all available information is collected.

In this chapter, the development of alternative detection and excitation schemes in AFM measurements are discussed. The multi-harmonic dual-ac resonance tracking is developed, enabling characterizations of local nonlinear physical phenomena for probing electrochemical, electromechanical, and thermomechanical effects. Another approach discussed here is the sequential excitation scanning probe microscopy (SE-SPM) technique which acquires high quality, efficient, and physically relevant data in frequency domain. Finally, a method based on full-information acquisition of probe motion and multivariate statistical analysis is provided. This allows for full characterization of linear tip-surface dynamics.

2.2 Tip-Sample Resonance and Dynamics of Simple Harmonic Oscillator

Resonance-enhanced AFM is a method that excites the probe tip-sample contact near its resonance frequency f_0 which enhances the probe deflection motion by orders of magnitude, enabling detection of quantitative information about the intrinsic material properties independent of the excitation frequency [63].

The dynamic motion of cantilever in resonance-based techniques can be viewed as a a damped simple harmonic oscillator (SHO) model [64], as schematically depicted in Figure 2.1. The SHO model mimics the deflection of probe near its natural resonance frequency by lumping the complicated cantilever motion and its interaction with the sample into a combination of a spring and dashpot. The frequency-dependent amplitude $A(f)$ and phase

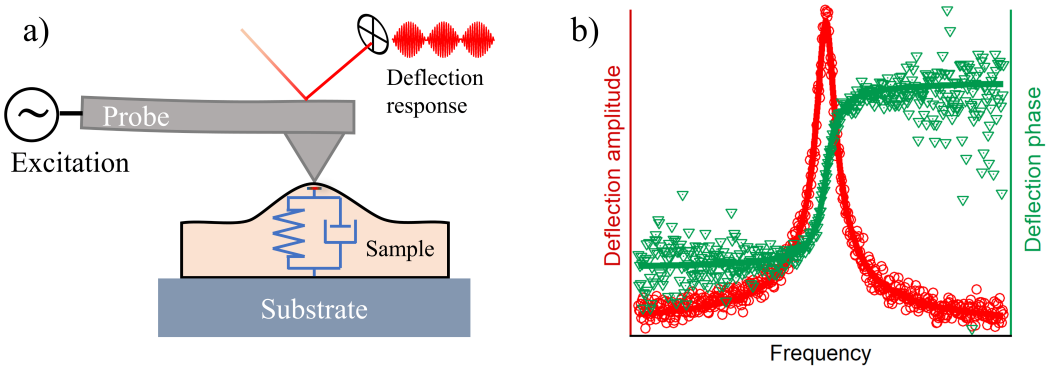

Figure 2.1: (a) The tip-sample interaction may be modeled with a simple harmonic oscillator model. (b) Regression of the amplitude and phase data based on SHO model reveals the intrinsic amplitude, phase, quality factor and resonance frequency of oscillation.

$\phi(f)$ of the cantilever motion can be written as:

$$A(f) = \frac{f_0^2 A_0}{\sqrt{(f_0^2 - f^2)^2 + (f_0 f/Q)^2}} \quad \text{and} \quad \phi(f) = \arctan\left(\frac{f_0 f}{Q(f_0^2 - f^2)}\right) + \phi_0, \tag{2.1}$$

where unknowns A_0, ϕ_0, f_0, and Q are intrinsic amplitude, phase, resonance frequency, and quality factor of oscillation, respectively. Note that f is the frequency of n^{th} order harmonic detection with an excitation frequency of f/n.

For a particular imaging mode, these parameters can yield valuable information about the dynamics of the system. For instance, in piezoelectric force microscopy, the intrinsic amplitude A_0 and phase ϕ_0 is correlated to the piezoelectric coefficient and orientation of the sample, while the quality factor Q and the resonance frequency f_0 revel information on the viscoelastic properties of the interaction [65]. In order to obtain the four unknowns A_0, ϕ_0, f_0, and Q, a discrete set of amplitude $A(f_i)$ and phase $\phi(f_i)$ data (as shown by red and green markers in Figure 2.1b) are needed to perform regressions based on Equations 2.1. However, obtaining these set of data through lock-in measurements is time-consuming (on the order of a second) and is not possible during scanning. Although the SHO model presented in this chapter pertain to the first bending mode of cantilevers, the analysis may be applied to the higher bending and torsional eigenmodes.

2.3 Data Analytic Tools

During AFM operation in resonance-enhanced mode, the dynamic motion of the cantilever is registered and digitized via the photo-sensitive detector (PSD). The PSD data contains the complex behavior of the tip-sample interaction and has a high bandwidth between 2-20 MHz (dependent on AFM electronics). Saving the PSD data for an AFM image usually results in a data-set with file sizes larger than 10 GB which is hard to handle. Classically, the PSD data is routed to lock-in amplifiers where the data is extensively compressed. Lock-in amplifiers obtain the amplitude and phase at few spectral frequencies which often results in loss of valuable information.

As an alternative method, the temporal information of PSD along with other channels of data can be stored directly to a hard drive using fast data acquisition systems. The obtained set of temporal data from PSD are, however, often redundant and hard to interpret. This section offers efficient data analytic and statistical tools to convert the data to physically meaningful set of variables. Multivariate statistical analysis such as principal component analysis are used to compress and reduce the dimensionality of the data. The truncated data are analyzed in time-frequency domain using wavelet-based analytic tools.

2.3.1 Principal Component Analysis

The AFM data-sets are post-processed by principal component analysis [66], which can decompose orthogonal components, arrange them in decreasing order of statistical significance, truncate the data, enhance signal-to-noise ratio, and highlight and separate exotic behavior with little computation effort. Consider a simple AFM scan consists of $g \times h$ pixels where full time-domain information of cantilever motion is recorded. The experimental data matrix $I_{ij} \equiv I(x_i, y_i, t_j)$ is reshaped in a way that the rows correspond to observations and columns correspond to variables. The observations (AFM cantilever motion) are repeated over all image pixels ($i = 1, ..., l = g \times h$) and the variables (in this case time t_j) are n snapshots of deflection signal ($j = 1, ..., n$) for each pixel. In turn, the i^{th} row of this matrix represents n

time-snapshots of cantilever motion for the image pixel $\#i$. Under PCA, the data set I is represented as:

$$I_{ij} = a_{ik} v_{kj}, \tag{2.2}$$

where $a_{ik} \equiv a_k(x_i, y_i)$ are the spatial expansion coefficients (known as PCA loadings) and $v_{kj} \equiv v_k(t_j)$ are corresponding eigenvectors (PCA coefficient). The eigenvectors v_k and their corresponding eigenvalues λ_k can be found from the variance-covariance matrix $\mathbf{C} = \mathbf{I^T I}$ or more efficiently by the singular value decomposition (SVD) of the experimental matrix:

$$\mathbf{I} = \mathbf{U \Sigma W^T}, \tag{2.3}$$

where $\mathbf{W}$ is a $n \times n$ unitary matrix and each column of $\mathbf{W}$ are the eigenvectors $v_k(t_j)$ in time domain, $\mathbf{\Sigma}$ is a $l \times n$ rectangular singular matrix whose singular values equal to the square root of the eigenvalues λ_k, and $\mathbf{U}$ is a $l \times l$ unitary matrix. Each column of $\mathbf{T} = \mathbf{U\Sigma}$ corresponds to the spatial expansion coefficients a_{ik}, also known as PCA loadings. The r^{th} PCA loading image $a_{ir} \equiv a_r(x_i, y_i)$ can be obtained by reshaping the r^{th} column of $\mathbf{T}$ to a matrix of $g \times h$. The scree plot of the normalized eigenvalues is obtained by expressing the fraction of each eigenvalue divided by the sum of all eigenvalues. Note that in PCA, the eigenvectors v_k are orthogonal and uncorrelated. The eigenvactor are sorted in a way that the corresponding eigenvalues λ_k are in descending order. For instance, the first eigenvector v_1 has the largest possible variance and thus, contains the most information.

Dimensionally-reduced data can be reconstructed by forming a truncated matrix $\widetilde{\mathbf{I}} = \mathbf{U_L \Sigma_L W_L^T}$, considering only the first L PCA modes (the L largest variances). This low-rank recovery of noisy experimental data (L-ranked) is obtained through hard shareholding of singular values as explained in literature [67]. The reconstructed low-rank $\mathbf{U_L}$, $\mathbf{\Sigma_L}$, and $\mathbf{W_L}$ matrices have much lower file size compared to the raw data and are saved for long-term storage.

The PCA analysis was performed using MATLAB's pca function. The function pca(I) returns the principal component variances in latent (referred here as eigenvalues), principal component scores (referred here as matrix of eigenvectors), and the principal component

coefficient (referred here as matrix of PCA loading images).

2.3.2 Continuous Wavelet Transformation

PCA eigenvectors v_k represent the behavior of each orthogonal mode of PCA in time-domian and are highly transient in nature. In order to extract the physical meaning of these mode, it is important to obtain the frequency-dependent amplitude and phase information of the eigenvectors. Continuous wavelet transforms (CWT) offers good time and frequency localization and are ideal for transforming transient temporal waveforms. Wavelet-based analysis are employed to transform the temporal eigenvectors to time-frequency domain. The CWT of a continuous function $f(t)$ is defined as:

$$C(a,b) = \int_{-\infty}^{\infty} f(t)\frac{1}{a}\psi^{\star}(\frac{t-b}{a})dt, \tag{2.4}$$

where $\psi^{\star}(t)$ is the mother wavelet in this case , a is wavelet scale (real number) , and b is the CWT translational values. The wavelet scales a are translated to the frequency while the transalational values b correspond to the amplitude of waveform. The analysis is computed using the analytic Morlet wavelet. The CWT is essentially a frequency-based filtering of the signal where the band-pass width of the filter is inversely proportional to the wavelet scale. The time-frequency representation is also a great tool for filtering in both time and frequency domain. The modified time-frequency representation is inverse transformed to the time domain through using inverse continuous wavelet transform.

Furthermore, the time-varying phase coherence between the eigenvectors and the excitation signal (or between any two signals) is analyzed by an wavelet-based approach. The wavelet coherence analysis returns magnitude-squared wavelet coherence and the phase of wavelet cross-spectrum. The coherence is a measure of the correlation between two signals and the phase is used to identify the relative lag between two signals.

The analyses are performed with MATLAB$^{\text{TM}}$'s wavelet toolbox cwt command for continues wavelet transform and wcoherence command for wavelet coherence analysis.

2.4 DART and Multi-harmonic Harmonic DART Approaches

Many AFM techniques such as piezoresponse force microscopy [68], Kelvin probe force Microscopy [53], scanning thermo-ionic microscopy [54], and electrochemical strain microscopy [33] are based on detection of the dynamic motion of cantilever deflection. In many cases, the amplitude of the cantilever deflection is on the order of 1–10 pm, and within the noise floor of the optical beam detection methods. However, the DART experiments may result in unreliable measurements. Excitation of the cantilever motion near or at the resonance frequency of the cantilever amplifies the signal, specially for cantilevers with high quality factors. However, a slight change in the dynamics of cantilever shifts the resonance frequency and thus the amplification factor would greatly change. This results in variable unknown amplification factors throughout a scan,introducing uncertainty regarding the true intrinsic amplitude detected. In order to measure the intrinsic amplitude response A_0, the amplification factor (also known as quality factor Q) should be determined and the amplified responses at the resonance f_0 should be divided by the quality factor.

The dual ac resonance tracking (DART) technique was developed for detection of cantilever motion near its resonance frequency [69]. In this technique the cantilever is excited with a bi-modal excitation sinusoidal waveform across its resonance frequency. Two lock-ins are used to measure the amplitude on the left and right sides of resonance. The difference in the amplitude is used a feedback loop to track the shifts in resonance frequency. Furthermore, by modeling the cantilever motion as a damped simple harmonic oscillator, the intrinsic properties of the motion such as intrinsic amplitude, phase, resonance frequency and quality factor can be obtained [45].

2.4.1 Multi-Harmonic Dual AC Resonance Tracking

The initial development of DART was only for first harmonic measurements, *i.e.* the response and excitation signals are linearly dependent. Notably, the different excitation sources in AFM often results in nonlinear responses. These include AFM techniques such as elec-

trostatic force microscopy [70], Kelvin probe force microscopy [53], scanning thermo-ionic microscopy [54], and scannin impedance microscopy [71]. There still lacks a method that can effectively probe the resonance-enhanced nonlinear responses and characterize the intrinsic properties. In this section, a generalized version of DART technique is developed, the details of implementation are presented and the analysis and results are provided. This technique allows measurement of nonlinear physical phenomena in contact mode and characterizes the intrinsic responses.

The schematics of multi-harmonic DART experimental setup for measurement of the n^{th} order frequency component is shown in Figure 2.2. Given the known resonance frequency of tip-sample contact f_0 in advance, two sinusoidal waveform are synthesized at frequencies f_1/n and f_2/n through an amplitude modulation process with the modulation frequency f_m and the carrier frequency $f_c = f_0/n$. The waveforms are digitally summed and converted to an analog signal, where they can be used to excite the tip-sample dynamics through electrical, mechanical, thermal, or magnetic stimulus. Due to the presence of n^{th} order nonlinear response, the deflection of probe will be modulated at frequencies $f_1 = (f_0 - f_m) \times n$ and $f_2 = (f_0 + f_m) \times n$. Two Lock-in amplifiers can isolate the response to measure the probe deflection amplitude ($A_1 \equiv A(f_1)$, $A_2 \equiv A(f_2)$) and phase ($\phi_1 \equiv \phi(f_1)$, $\phi_2 \equiv \phi(f_2)$) at the two modulation frequencies f_1 and f_2. The difference in the amplitude measurements $(A_1 - A_2)$ is used as an error signal to track the shifts in the resonance frequency. If $f_1$and f_2 are symmetrically located around the resonance peak (solid blue curve in Figure 2.2b), $A_2 = A_1$ and the error signal is zero. However, if the resonance shifts to a higher value f_0', the amplitude at lower frequency A_1 decreases to A_1' and *vice versa* for the A_2 (broken blue curve in Figure 2.2b). This results in a negative error signal. The error signal (shown by red solid curve figure 2.2b) can be used in a feedback loop to track the resonance frequency by adjusting the carrier frequency $f_c = \frac{f_0}{n}$ in order to maintain the error signal around zero. Note that the modulation frequency is kept constant throughout the experiments.

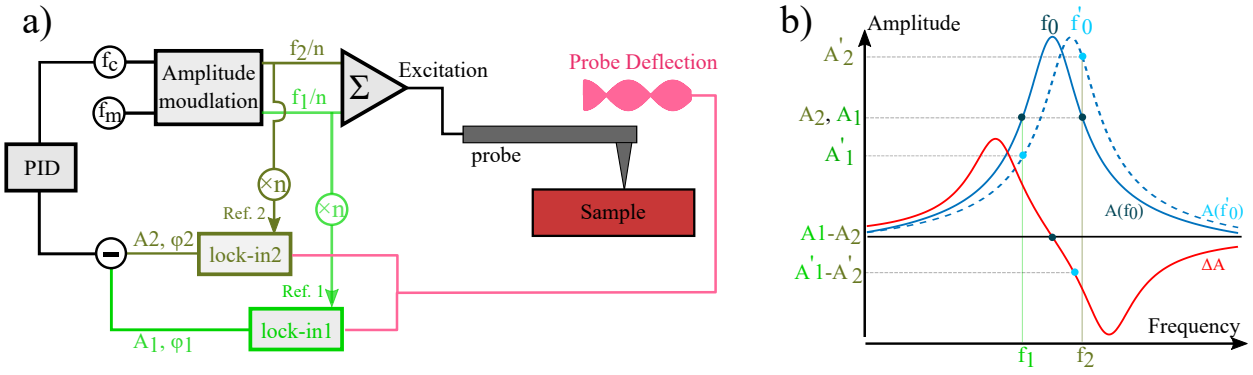

Figure 2.2: Schematic of DART measurements for n^{th} order harmonic response. (a) The detection experimental setup schematic containing dual ac synthesizer, amplitude modulation unit, lock-ins, and PID controller merged with AFM. (b) An illustration of DART feedback principle.

2.4.2 Calculation of SHO Model Parameters

The DART technique measures amplified deflection signals near the tip-sample resonance frequency. However, the DART amplitude and phase measurements at frequencies f_1 and f_2 do not reveal much physical information about properties of the sample. If modeled with SHO (as described in Section 2.2), the DART measurements (A_1, A_2, ϕ_1, ϕ_2) are sufficient to determine the four unknown parameters of SHO model (A_0, ϕ_0, f_0, and Q) which are physically meaningful parameters.

The Equations 2.1 can be rewritten as: [45]

$$\frac{X_2^2+1}{X_1^2+1} = \Omega^2 \quad \text{and} \quad \frac{X_1 - X_2}{1 + X_1 X_2} = \Phi, \tag{2.5}$$

where $\Omega = \frac{f_1 A_1}{f_2 A_2}$, $\Phi = \tan(\phi_2 - \phi_1)$ are know from DART measurements, and the dimensionless quantities X_1 and X_2 are calculated as:

$$X_i = \frac{f_0^2 - f_i^2}{f_0 f_i / Q}. \tag{2.6}$$

By solving Equations 2.5 for X_1 and X_2, the f_0 and Q are found as [45]:

$$f_0 = \sqrt{f_1 f_2 \frac{f_2 X_1 - f_1 X_2}{f_1 X_1 - f_2 X_2}} \quad \text{and} \quad Q = \frac{\sqrt{f_1 f_2 (f_2 X_1 - f_1 X_2)(f_1 X_1 - f_2 X_2)}}{f_2^2 - f_1^2}, \tag{2.7}$$

and the intrinsic amplitude A_0 and phase ϕ_0 are determined as:

$$A_0 = A_1 \frac{\sqrt{(f_0^2 - f_1^2)^2 + (f_0 f_1/Q)^2}}{f_0^2} \quad \text{and} \quad \phi_0 = \phi_1 - \arctan(\frac{f_0 f_1}{Q(f_0^2 - f_1^2)}). \tag{2.8}$$

Equation 2.1 imposes a physical constraint for phase measurements, $\phi_2 > \phi_1$ for $f_2 > f_1$. This requirement should be met in all measurement, otherwise the obtained solution is ill-posed and should be ignored.

2.4.3 Implementation

The multi-harmonic DART STIM requires addition hardware and software for implementation on an AFM. The technique is implemented on a MFP-3D bio AFM (Asylum Research) merged with an external lock-in amplifier (HF2LI, Zurich Instruments). The deflection signal is routed to the AFM controller output and connected to the input source of the lock-in amplifier while the internal oscillators of the lock-in are used as an excitation source and routed to the heated probe. The lock-in amplifier and the AFM are synchronized using external trigger signal generated by the AFM controller. The trigger signal has a high-state in the beginning of each AFM scan line, as it is shown later in Figure 2.11.

The lock-in is controlled via LabOne software. The parameters and configuration for a second harmonic STIM is shown in Figure 2.3. The lock-in has two amplitude modulation (AM) module. The first module is used to generate AM waveform with a carrier frequency of around 83 kHz and modulation frequency of 3 kHz with an amplitude of 7 V, which is routed to the lock-in output and connected to the heated probe. The second AM module has the same settings as the first AM module except that the carrier and modulation frequencies are at higher harmonics and is merely used for detection. In the example shown in Figure 2.3b, the second AM has performs second harmonic with a carrier frequency of around 166 kHz and modulation frequency of 6 kHz while output amplitude is turned off. All AM waveforms are carrier suppressed, *i.e.*, the generated signal is dual-ac. The PID unit of the lock-in performs dual-ac resonance tracking by measuring the difference between the different in the amplitude and adjusting the carrier frequency of the AM modules. Parallel to the AFM

operation, the lock-in measurements (A_1, A_2, ϕ_1, ϕ_2, and f) are recorded for each pixel and transferred to hard drive in real time. The data is post-processed and visualized with MATLAB (see Section Sec:calculSHOpar for details).

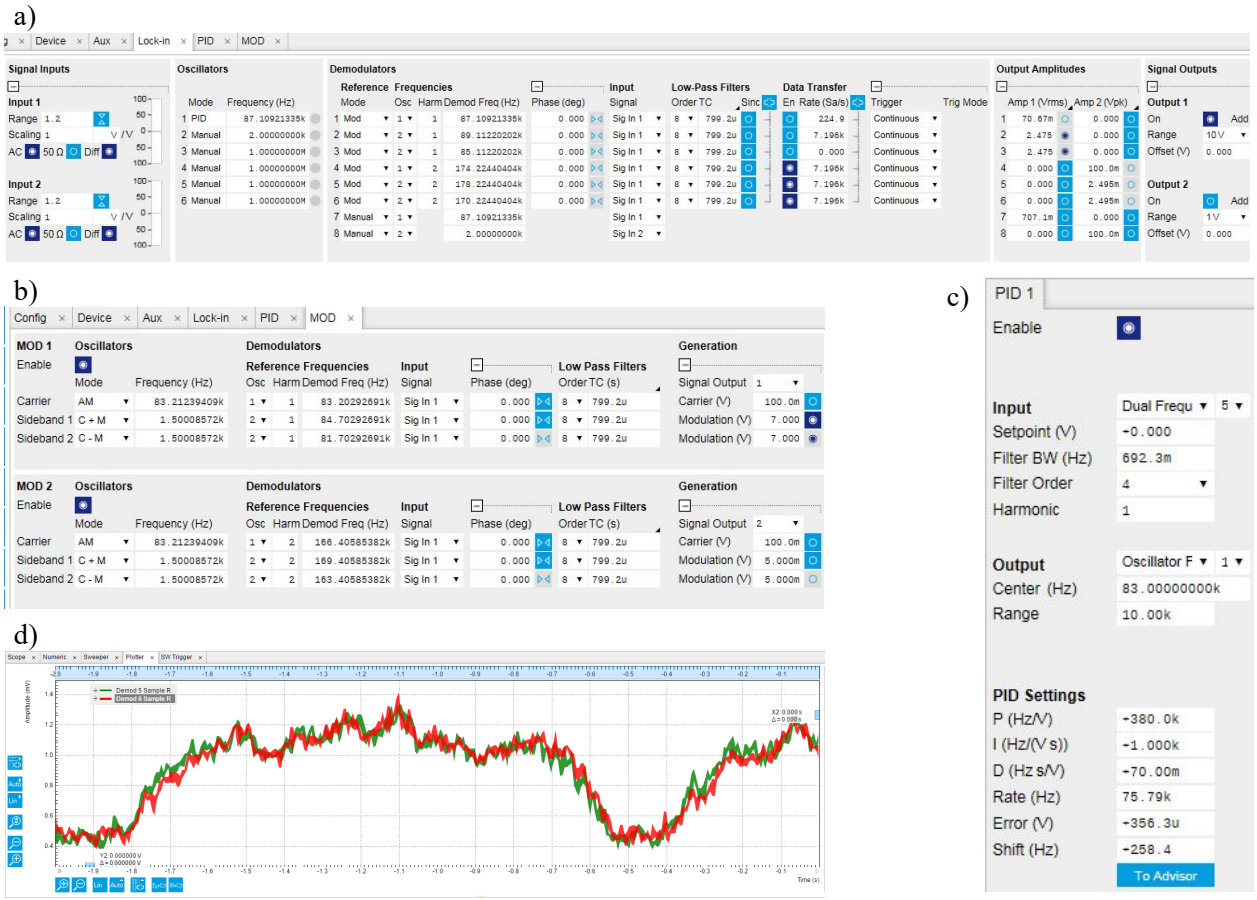

Figure 2.3: Lock-in software interface (LabOne) with configurations for 2nd harmonic STIM experiment. (a) Lock-in settings, (b) amplitude modulation configurations, (c) PID parameters, and (d) plot of A_1 and A_2 obtained from lock-in demodulators 5 and 6 within an AFM line scan.

2.4.4 Experimental Results

Figure 2.4 illustrates multi-harmonic DART measurement on a nano-crystalline ceria sample. While obtaining the topography (Figure 2.4a) in contact mode, the external lock-in amplifiers measure the deflection amplitude (Figures 2.4b,c) and phase responses (Figures 2.4e,f). The

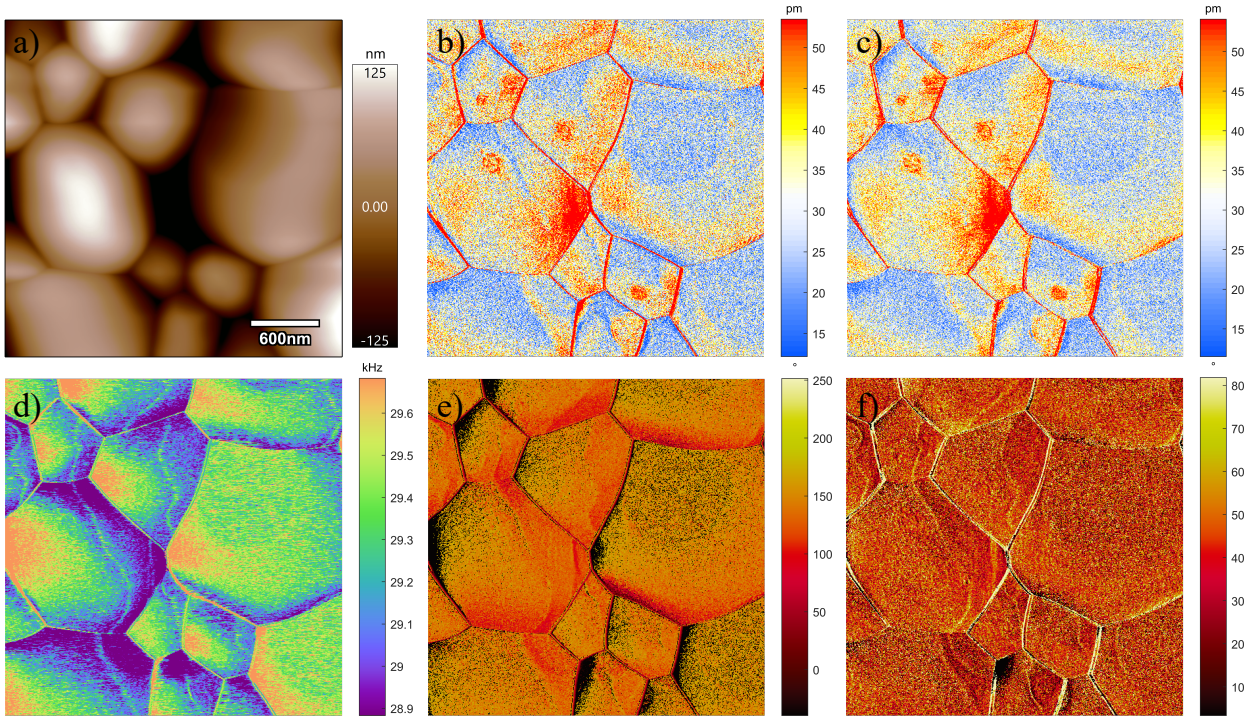

Figure 2.4: 4^{th} harmonic DART measurements in scanning therm-ionic microscopy (STIM) on a ceria sample. (a) Topography, (b) amplitude A_1 and (c) A_2, (d) carrier frequency f_c, and (e,f) phase ϕ_1 and ϕ_2 maps. The STIM measurement was performed with resistive heating implemented on a MFP-3D AFM combined with a HF2LI lock-in amplifier.

grain boundaries of ceria are expected to have a higher ionic concentration which results in higher amplitude responses in STIM mode (see Chapter 3 for STIM principle and material properties). Although both amplitude maps show higher responses on grain boundaries, drawing conclusions about the material properties from these measurements is difficult. The DART technique adjusts the carrier frequency f_c (shown in Figures 2.4d) by minimizing the difference in the amplitude responses across the resonance frequency as the AFM scan proceeds. In turn, the amplitude maps A_1 and A_2 show similar behavior, confirming the reliability of resonance tracking in DART.

In order to find the intrinsic properties, the obtained data is analyzed with the SHO model and the model parameters are mapped and depicted in Figure 2.5. The map of intrinsic

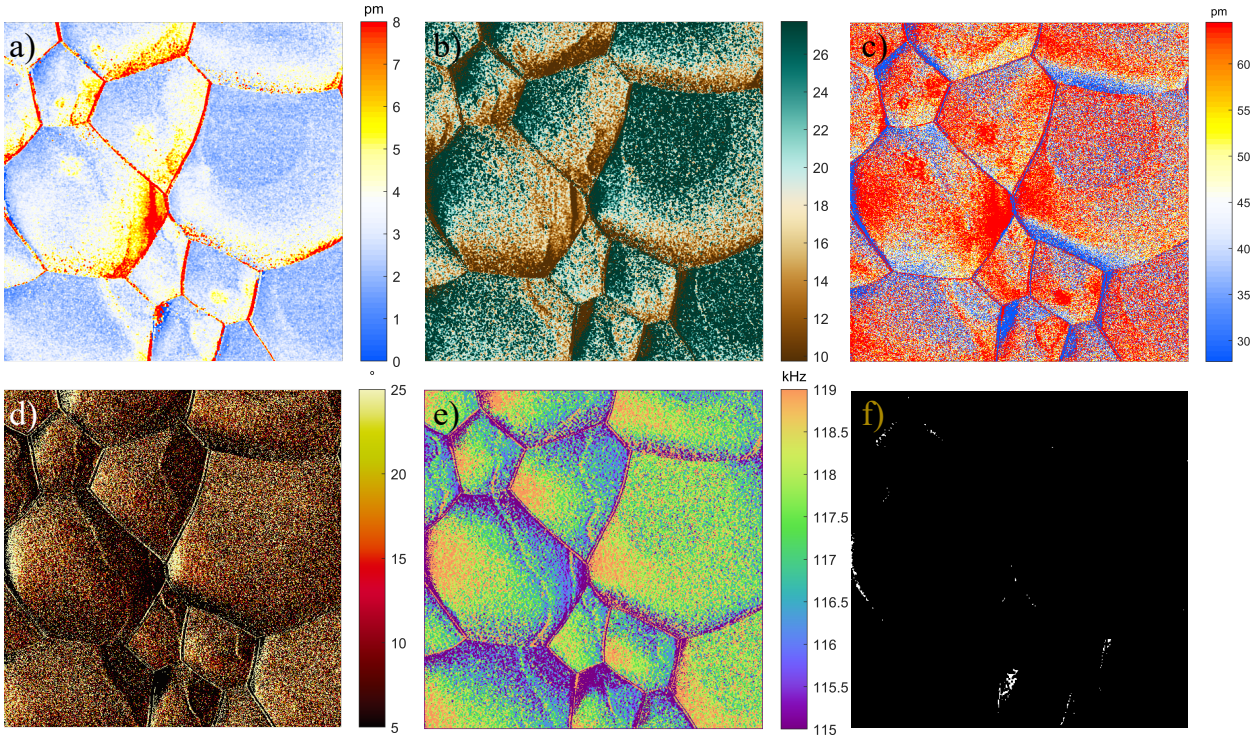

Figure 2.5: SHO model reveals properties of a ceria sample mapped by the 4$^{\text{th}}$order DART STIM. (a) Intrinsic amplitude A_0, (b) quality factor Q, (c) amplified amplitude A_0Q, (d) phase ϕ, and (e) resonance frequency mappings f_0. The while pixels in (f) shows the failures of SHO in finding a solution.

amplitude A_0 shows the frequency-independent deflection oscillation magnitude which is correlated with the ionic concentration of the surface. The quality factor map Q shows the amplification factor providing information on viscous energy dissipation of the material. Comparison between the maps of intrinsic A_0 and amplified A_0Q amplitudes reveals the importance of the SHO analysis. While A_0 shows higher responses on grain boundaries of ceria, the A_0Q map illustrates higher responses on ceria grains due to higher amplification factors on grains. The intrinsic phase ϕ_0 explains the deflection phase lag which should be uniform in STIM measurements. This is indeed observed in Figure 2.5d, where the phase variations are around 20°, where phase variations in ϕ_1 and ϕ_2 maps were more than 100°. Furthermore, the map of resonance frequency f_0 shows the detection frequency in STIM

which can be correlated to the elastic modulus of the sample. The white pixels in Figure 2.5f shows the failures of SHO model in finding a solution. This can be attributed to unstable tip-sample contact on rough areas of the surface or possibly due to poor signal to noise ratio where the responses are low. Also, the SHO failures may be caused by nonlinear responses that cannot be explained with SHO model.

This example illustrates the power of physics based models such as SHO in extracting meaningful information from the dynamic motion of cantilever measured in DART experiments. In a single scan, various information including surface roughness, viscoelastic properties, and transport properties can be obtained. In practice, however, care should be given to the limitations of SHO model in analyzing the data. It has been observed that there are discrepancies at the fringes of resonance peak, causing unreliable estimates of SHO parameters [47]. Moreover, frequency feedback may be inaccurate when the contact resonance frequency shifts dramatically over a relatively short distance. This is especially a big problem in nanostructured materials that exhibit substantial heterogeneity in mechanical properties at the nanoscale, near the grain boundaries. The feedback errors results in off-resonance measurements and unreliable estimation of intrinsic parameters. In the next sections, alternative methods are offered that can overcome the aforementioned difficulties.

2.5 Sequential Excitation Scanning Probe Microscopy

In this section, a sequential excitation scanning probe microscopy (SE-SPM) technique is proposed to solve problems associated with DART and BE measurements. In order to acquire high quality (less noisy), efficient (less redundant), and physically relevant SPM data, sequential excitation (SE) that obtains a fast sequence of images with different frequencies is relied on. The approach is demonstrated using piezoresponce force microscopy as an example in a PZT thin film. The obtained data in SE approach is enhanced by principal component analysis (PCA) and SHO-based regression analysis during post processing, allowing quantitative characterization of intrinsic material properties with minimal artifacts such as cross-correlations with topography. The SE concept can be applied to a variety of

other types of SPM imaging modes for example Kelvin probe force microscopy (KPFM), contact resonance mapping, and AFM-IR, to enable more accurate quantitative analysis. The method is easily implemented in any atomic force microscopes with one standard lock-in amplifier, without any additional hardware instrumentation.

2.5.1 SE-SPM Principle

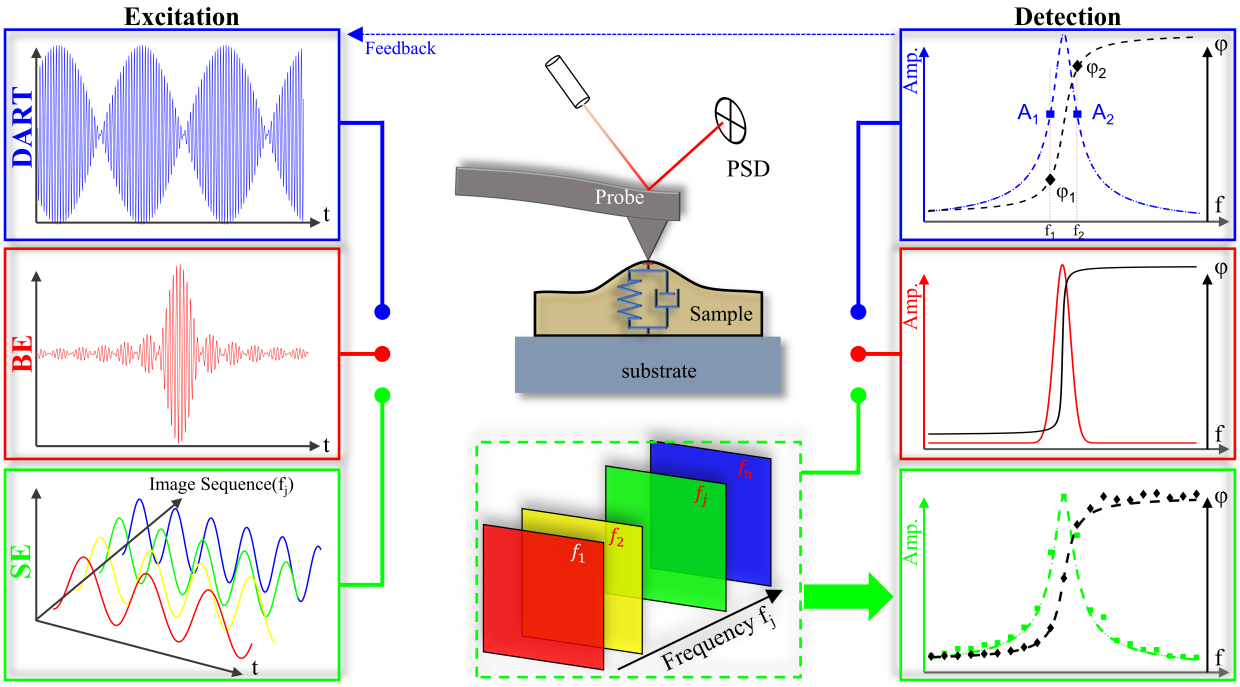

Figure 2.6: The schematics of dynamic SPM experiments based on DART, BE, and SE techniques, wherein AC waveform combining two distinct or a band of frequencies are synthesized to excite the sample under DART or BE, respectively, while a sequence of AC waveform with different frequencies f_j is used to excite the sample under SE.

The excitation and detection methods in DART, BE, and SE techniques are schematically illustrated in Figure 2.6. The DART utilizes bi-modal excitation and detection at frequencies f_1 and f_2. The difference in amplitude responses A_1 and A_2 are used in a feedback-loop to track the resonance frequency f_0. If the separation between two excitation frequencies is too small, they will easily fall out of resonance range, and resonance tracking fails. If

the separation is too large, the signals are weak. Moreover, most nanostructured materials exhibit substantial heterogeneity in mechanical properties at the nanoscale, for instance near the grain boundaries. In turn, the contact resonance frequency shifts dramatically over a relatively short distance, resulting in a failed resonance tracking.

BE can be viewed as a generalization of DART, by synthesizing a waveform using a range of frequencies within a band rather than two discrete frequencies, in turn generating a band of responses corresponding to the excitation frequencies. This can be used to solve for intrinsic responses by SHO model for each pixel of the image. If the band is wide enough, the resonance shift will not fall outside of the band, and the need to track and adjust excitation frequencies is eliminated. However, since the excitation energy is distributed over the whole band, the signal at each excitation frequency is low, which compromises signal-to-noise ratio. Furthermore, sophisticated instrumentation is needed to implement BE on a standard AFM, making it not readily accessible by research laboratories. Both methods treat each pixel response as an individual block of data without considering statistical correlations in the whole image data set.

2.5.2 SE-SPM Experimental Implementation

To demonstrate the feasibility of SE-SPM, piezoresponse force microscopy (PFM) is performed to probe electromechanical properties of a PZT thin film, wherein 42 single frequency PFM images of topography, amplitude and phase were acquired on an identical area of the sample with a scan rate of 5 Hz/line. Note that DART measurements are usually performed with a scan rate of less than 1 Hz/line. The sinusoidal bias, ranging in frequency from 320 to 400 kHz with increments of 2 kHz/scan and the drive amplitude of 3V excites the sample through a conductive Pt/Ir AFM probe tip in contact mode. The desired harmonic of amplitude and phase of deflection signal in each image are obtained through lock-in amplifier measurements. Since drifting during different scanning is inevitable, these mappings are realigned to match each other at different frequencies. The effect of drift in the series of SE images was compensated by taking the topography of the first image as a benchmark and

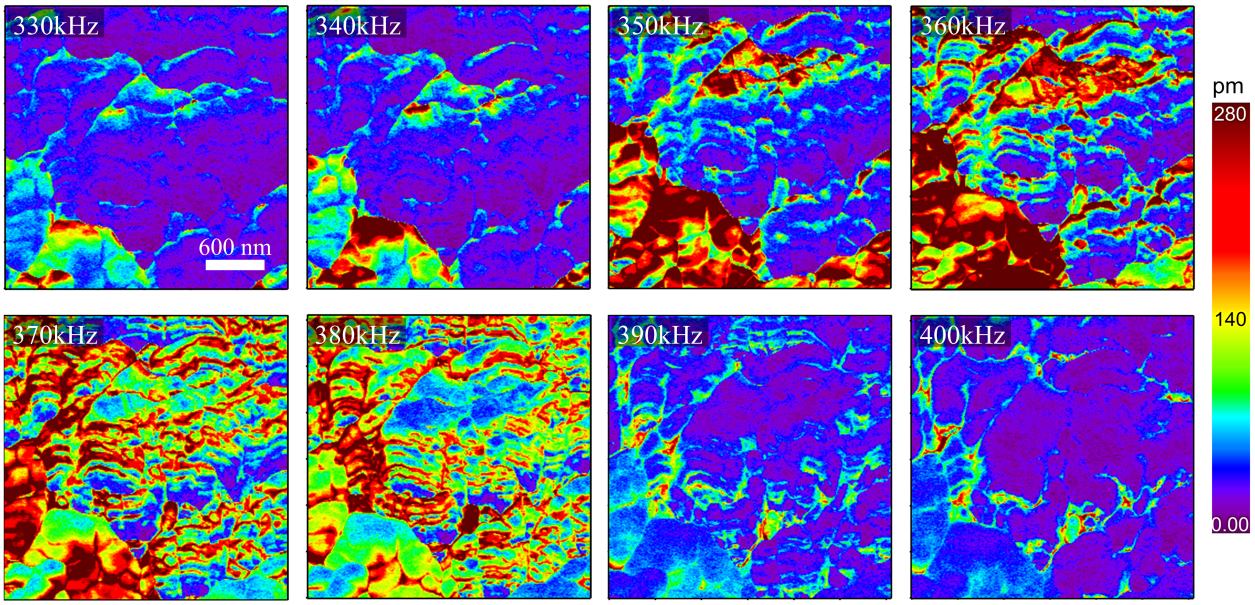

Figure 2.7: A series of representative amplitude mappings obtained at sweeping frequencies of SE-PFM

performing a 2D-cross-correlation between topography of each image and the benchmark.

The raw amplitude mappings obtained at 8 distinct frequencies are shown in Figure 2.7. It is observed that the amplitude is very sensitive to the excitation frequency, as expected, and there is substantial evolution of amplitude response as well as phase responses (not shown) when the excitation frequency varies. In addition, substantial spatial heterogeneity is observed within each mapping. This may reflect variations in the intrinsic electromechanical response, the resonance frequency, the energy dissipation, or combination of these effects.

2.5.3 DATA Analysis in SE-SPM

Principal Component Analysis

The experimental data obtained visa SE approach is post-processed by principal component analysis, as detailed in Section 2.3.1. Figure 2.8 shows an example of PCA analysis on the set of data obtained through SE-PFM. The scree plot λ_k shows a fast drop-off eigenvalues, as shown in Figure 2.8a, demonstrating that only first few modes contain significant

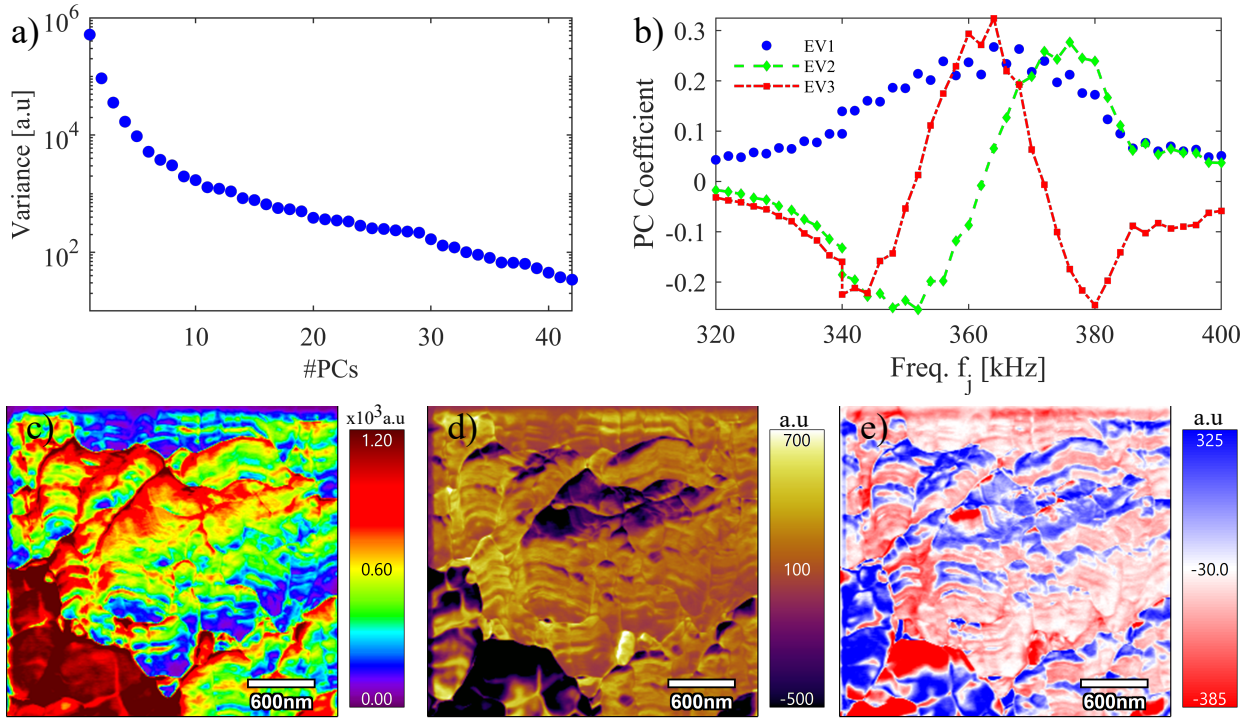

Figure 2.8: Principal component analysis of SE-PFM data; (a) the scree plot of eigenvalues, (b) the first three eigenvectors, and (c-f) corresponding first three loading maps.

information. In fact, visual examination of PCA loading maps a_k in Figures 2.8(c-e) suggests that only the first three PCA modes contain physical information and the remaining loading maps mostly contain noise. The eigenvectors shown in Figure 2.8b capture the frequency-dependent behavior of each loading map. The first eigenvector $v_1(f_j)$ respresentes the average piezoresponse, while the second eigenvector $v_2(f_j)$ and the third eigenvector $v_3(f_j)$ represnt the variation of amplitude data due to the spatial variation in resonance and quality factor,respectively. Similar behavior has been observed in PCA analysis of magnetic force microscopy [72]. The PCA analyses are computationally efficient and powerful tools for preliminary visualization of data. The analyses also enhances the signal-to-noise ratio of the data through dimensional reduction. However, due to the unsupervised nature of PCA analysis, drawing quantitative conclusions about the material properties is challenging.

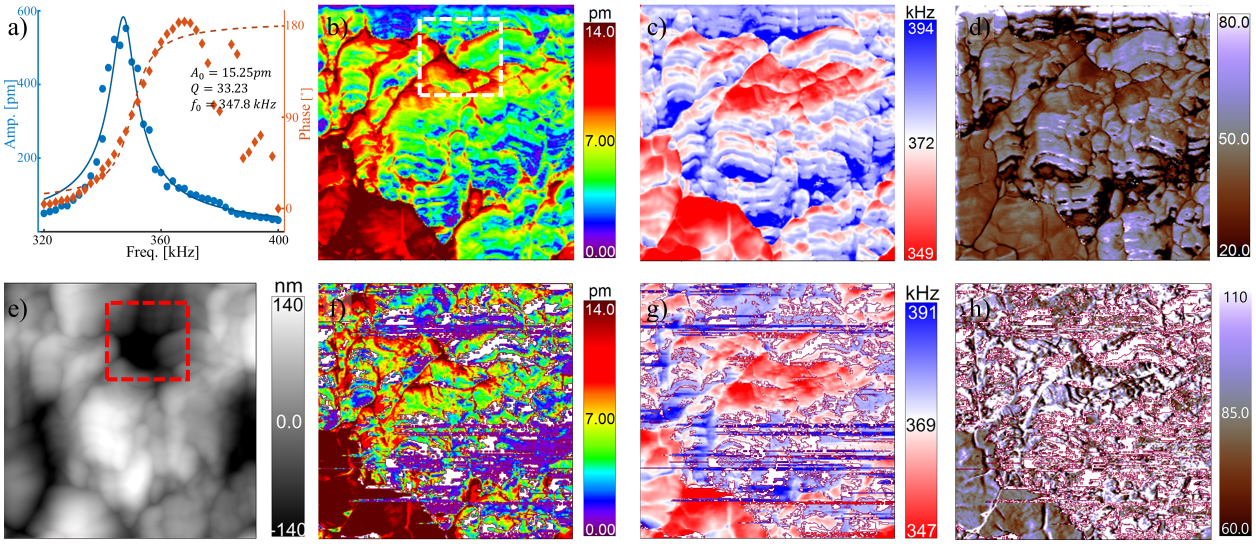

Figure 2.9: Comparison of SE-PFM and conventional DART PFM. mappings reconstructed using SHO at each pixel point; (a) SHO fittings at one representative pixel points; (e) topography; (b,f) intrinsic amplitude A_0; (c,g) resonance frequency f_0; (d, h)phase ϕ_0 obtained via SE-PFM (upper row) and DART PFM (lower row).

SHO Analysis of SE-SPM

In order to obtain clear mechanistic insights guided by the underlying physical principles, the SE data is analyzed via brute force physical model based on SHO model. This is accomplished by fitting 3D data sets of low-rank amplitude $\widetilde{A}(x, y, f_j)$ and phase $\widetilde{\phi}(x, y, f_j)$ at each pixel using SHO Equations 2.1. The low-rank experimental data matrices ($L = 3$) were found based on analysis in the previous section and the SHO regression analyses were performed using GPU-accelerated CUDA implementation of the Levenberg-Marquardt algorithm [73].

A comparison of SE-PFM and conventional DART PFM (developed by Asylum Research) intrinsic properties is provided in Figure 2.9. While the upper row in the figure shows the reconstruction results from SE-PFM while the lower ones are obtained from conventional dart PFM. The raw data and the SHO fittings for a representative pixels are illustrated in Figure 2.9a. The SHO analysis can be applied to reconstruct the mappings of intrinsic amplitude and phase, as shown in Figure 2.9b,c, and there is strong variation in amplitude

mapping, though little correlation is seen between topography and amplitude, even in regions with substantial topography variation, for example in the valley on the top part of the mapping marked by the red square. The phase mapping, on the other hand, only shows small variation, indicating more or less aligned polarization orientation. Mapping of R^2 (not shown) defined as the fitting coefficient of determination, reveals values ranging from 0.86 to 0.99 and suggests a high fidelity of SHO model, demonstrating the capability of SE-PFM even for highly inhomogeneous materials. In addition, resonant frequency mapping (Figures 2.9c) reveals substantial spatial heterogeneity in viscoelastic properties. The DAR PFM on the pther hands fails to find solution in a portion of the map (noted by white areas) and results in unreliable measurements.

2.6 Big-data AFM

2.6.1 Why Big-data AFM?

Conventional AFMs are based on sinusoidal excitation of AFM probe in the time domain and harmonic detection of probe deflection registered in AFM photosensitive detector (PSD) by lock-in amplifiers in frequency domain. Sinusoidal excitation essentially limits the probing to a specific physical process occurring at a particular time scale and harmonics. The streamed deflection data (or possibly any other channel of data) may not contain enough relevant information due to the limited excitation waveform, and the lock-in detection results in data compression by orders of magnitude. This results in permanent loss of possible valueable information during the demodulation process [74]. Such an approach is acceptable for relatively simple and well-understood physical phenomena, yet for any materials and systems that involves complicated, transient, coupled, and often competing microscopic mechanisms, especially in nonlinear regime, the data acquired is incomplete and often biased. As such, obtaining high-dimensional, deep, and smart data in AFM measurements is highly desired.

In this section, the experimental implementation for a big-data AFM technique, inspired by recently developed general-mode AFM [75], is explained and preliminary results are pro-

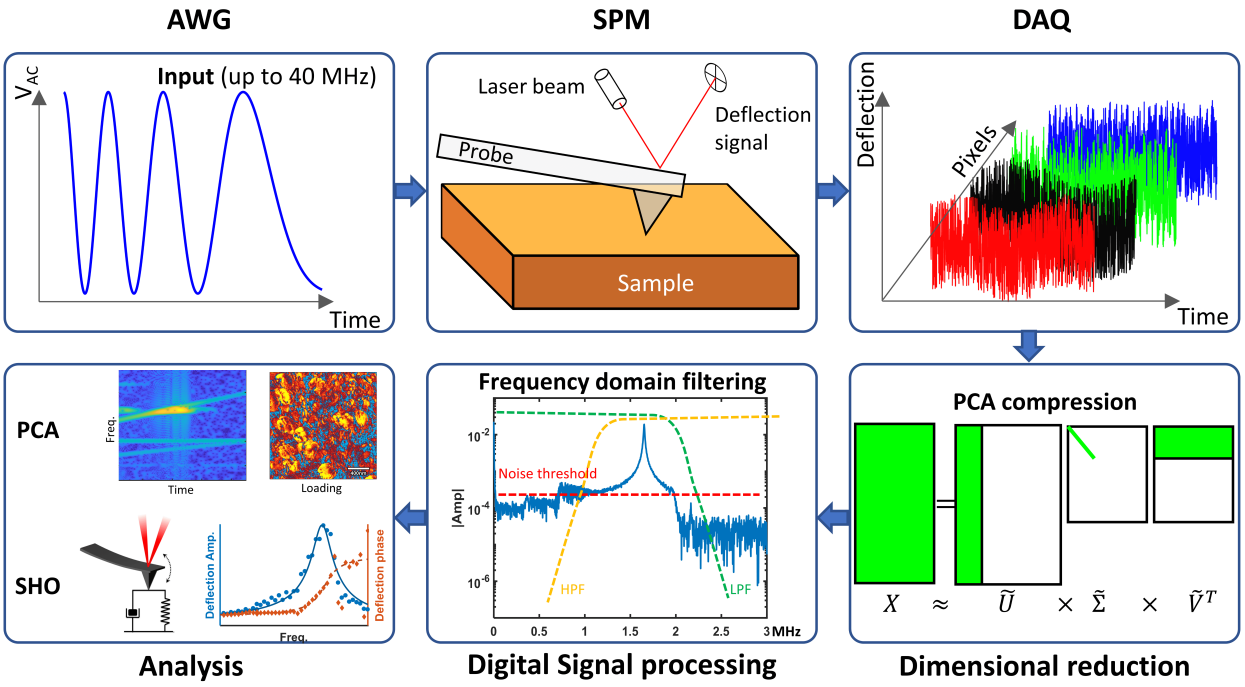

Figure 2.10: The architecture and data flow of the big-data AFM.

vided. The designed big-data AFM is capable of surveying a wide range of physical phenomena simultaneously through dual excitation with arbitrary waveform generation and acquiring highly-sampled information without pre-commitment to a particular phenomenon and time scale. Furthermore, the obtained data can be analyzed by performing multivariate statistical analysis or physical interpretation to extract dominant as well as relevant patterns.

2.6.2 Implementation of the Method

Overall Architecture of Big-data AFM

Figure 2.10 illustrates the fundamentals of the big-data AFM method, consisting of six main parts. First, the probe is excited by any waveform generated with an arbitrary waveform generator (AWG), such as single frequency excitation, band excitation or any other complex excitation forms. While the SPM is performing, the full-time domain response of two input signals (such as vertical and lateral component of deflection signals, current signals, etc.)

are recorded. The synthesized input data and the recorded deflection data has identical sampling rate and data points which allow easier data structuring and leakage-free spectral analysis during the post-processing stage. The initially saved raw data, on the order of 10 GB, is reformatted and compressed using dimensional reduction methods such as singular value decomposition (SVD) or wavelet analysis. The low-rank data matrix (file size less than a GB) is saved for long-term storage. Next, several optional filtering schemes (such as noise threshold and high-, or/and band-, or/and low-pass filters) can be applied. The filtering can be performed in time-, frequency-, or time-frequency domains based on the physics of interest. This digital signal pre-processing stage which can be done on-the-fly or later is based on the raw data from a pixel, a line, or the entire scan —unlike the lock-in filtering that is performed based on each individual pixel data— and is fully reversible as opposed to permanent loss of data after filtering in lock-in measurements. Once the data is compressed, denoised, and processed, it can be analyzed to reveal the dynamics of the cantilever motion. The first method is a physics-based approach, where a known physical behavior of probe is detected and the physical parameters are extracted based on model fitting. For example, the SHO model, which mimics the resonance behavior of probe and reveals valuable information about material under the probe, is fitted to probe deflection data around its contact resonance frequency (see section 2.2 for details). Note that as opposed to lock-in measurements where the fittings are performed with only few number of data points, the model fitting can be done with statistical significance. The other approach that can be adopted is an information-based theory analysis. Multivariate statistical analysis, such as PCA, can decompose orthogonal components, arrange them in decreasing order of statistical significance, and highlight and separate exotic behavior with little computation effort. The eigenvectors of PCA can elucidate the richness of the data while the corresponding loading maps show the spatial variation of the data, which was not possible during the lock-in measurements. The details of the implementation and analysis are offered in the following sections.

Arbitrary Wave Signaling and Synchronization

Instead of relying on sinusoidal signal generation built-in to the commercial AFM systems which are inadequate for big-data approach, an external AWG to synthesize complex arbitrary waveforms as desired is used. The waveform is converted to analog signals with an analog-to-digital conversion rate of 1.8GHz. The dual channel outputs of AWG is served to excite the probe through multiple sources including tip-sample contact excitation, photothermal laser heating, and internal piezo-actuator of the probe. This is implemented by using an AWG unit (Zurich Instruments UHFAWG, dual 600MHz Analog output, sampling rate up to 1.8GHz) in parallel with a Cypher AFM (Asylum Research). This UHFAWG can adjust the next waveform based on the state of the 32-bit digital input/output (I/O) or internal lock-in data with a time delay as small as 50 ns, ideal for real time adaptive experimental control on-the-fly.

It is critical that different excitation sources work in parallel and synchronized with the AFM cantilever motion and AFM XY scanners, essential for detecting true underlying transient dynamics. Most commercial AFM systems use analog pixel trigger signal to align the excitation with the measurement. The analog triggers have jitter time on the order of μs and often introduces dead-time between each pixel excitation and phase delays between the corresponding measurements when used with external sources. Thus, it is highly desirable to synthesize the excitation signal for an entire AFM line scan.

As shown in Figure 2.11, this is accomplished by performing the triggering with a highly sampled analog signal (200 MHz) from AFM controller. An Igor-Pro^{TM} program is developed for Asylum Research AFMs that generates trigger signals 10 ms before each scan line is started. Before scanning, the AWG generates the digital waveform and transfer the data to the waveform memory. The 128M sample waveform memory of AWG enables generation of high-resolution waveform shapes for each trace/retrace pass of AFM scan, eliminating the dead time and phase coherency errors between pixel measurements. When the AFM trigger is received (10 ms before the start of each AFM line scan), the AWG is triggered,

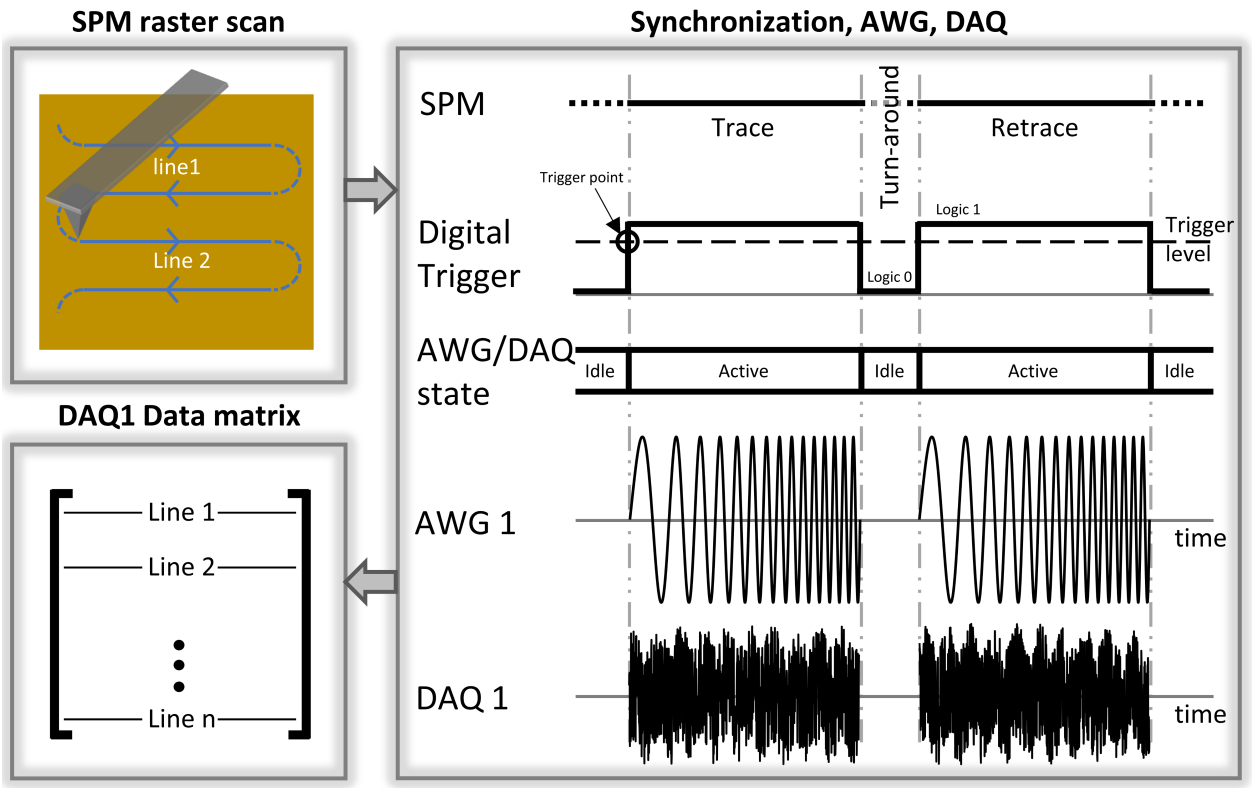

Figure 2.11: Signaling and synchronization of big-data AFM

the waveforms is sent to ADC. The digital markers associated with the excitation waveform trigger the necessary DAQ channels with a dead times less than 50 ns. The turn-around time between trace/retrace passes is more than enough for the AWG/DAQ to adjust the excitation parameters and transfer the data to hard drive. The extra saved data before the start of each line is removed later in post-processing stage.

Data Acquisition

Most commercial AFMs perform lock-in measurements to characterize the dynamics of the cantilever motion through lock-in amplifiers, reducing full time-domain information to limited frequency-domain data in terms of amplitude and phase. The lock-in trades off the loss of full information for higher signal-to-noise ratio measurements at particular frequencies. This limits the information learned to particular frequency and harmonics. In this approach,

a real-time data acquisition system (DAQ) is used to digitize and record the entire motion of the cantilever in time domain. The measurements are repeated for each AFM scan line with a high accuracy and sampling rate in parallel to AWG excitation. Rather than sweeping the excitation frequency and measuring the averaged spectral amplitudes, this method is based on fast and continuous change of frequency while recording highly sampled-signals in time domain, well suited for state-of-the-art big-data analytic tools to obtain spatial-temporal features. This is implemented using an external Zurich Instrument UHF-DIG digitizer (12-bit, 1.8GH) integrated with built-in lock-ins, phase locked loops, and PID controllers, all using synchronous clocking source along with AWG.

The number of samples in the AWG waveform for each pass (N_s) must equal to the number of samples in each measurement and equal to power of 2, to ensure (1) a leakage-free Fourier transform and (2) robust multi-resolution analysis in post-processing stage. Given the sampling rate F_s, the scan length d, and the slow-axis scan speed v, N_s can be approximated by $N_s = dF_s/v$, which usually is not an integer power of 2. It is critically important to obtain new $N_s^\star = 2^{\lfloor \log_2 N_s \rfloor}$. Since the speed of AFM X-Y scanners are selectable with high accuracy, the AFM scan speed is adjusted based on the adjusted $N_s^\star$ and is $v^\star = dF_s/N_s^\star$. The final data matrix, (Figure 2.11), is easily reshaped for any number of pixels/line without any dead-time between pixels. The digital markers associated with each AWG waveform are binary and can be easily saved along the arbitrary waveform parameters. This allows perfect reconstruction of excitation signal in post-processing stage, without the need to save the analog signal, and would allow affordable digital modulations later.

Dimensional Reduction

Dimensional reduction is performed thorough application of principal component analysis. The details of the method is explained in Section 2.3.1.

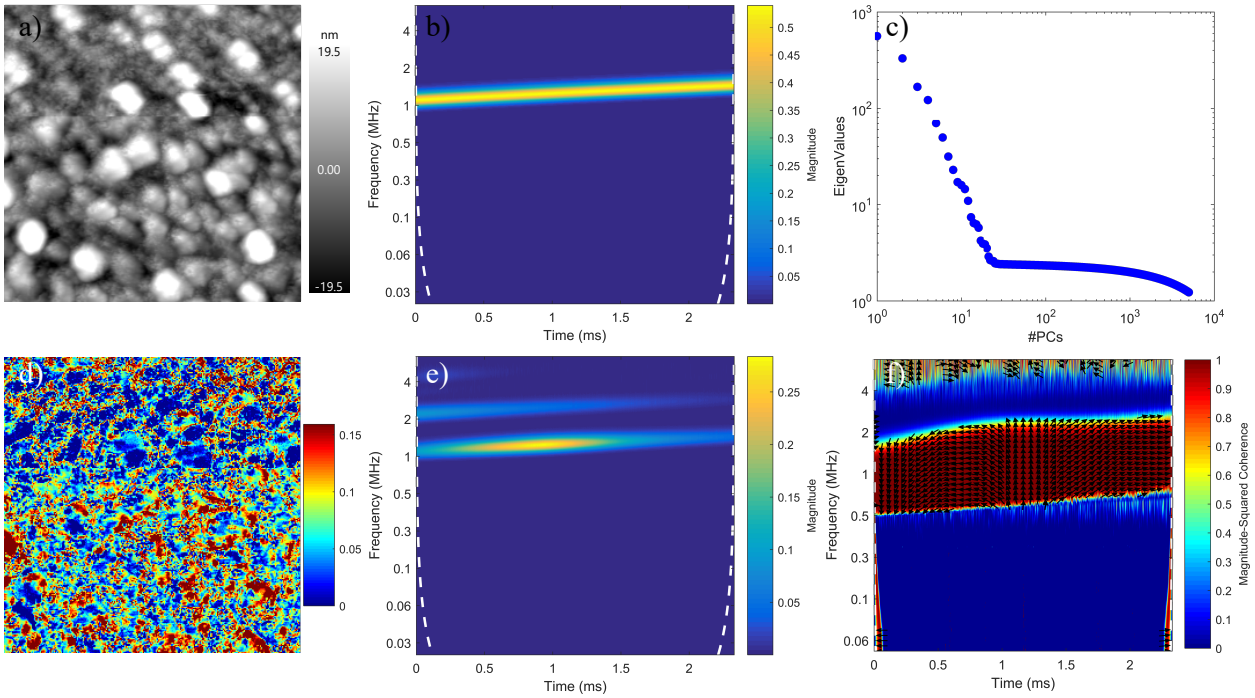

Figure 2.12: Piezoresponse force microscopy with big-data AFM. (a) Topography of BFO thin-film sample obtained via contact mode ($5 \times 5\ \mu m^2$), (b) time-frequency representation of chirp excitation, (c) eigenvalues of PCA analysis, (d) the 1st PCA loading, (e) its corresponding eigenvector represented in time-frequency, and (f) phase coherence between the eigenvector and excitation signals. The time-frequency analysis obtained through CWT.

Digital Signal Processing

In this step, several optional filtering schemes such as noise thresholds, high-, band-, or low-pass filters can be applied. It is important to note that the signals are highly transient and they should be filtered in both time and frequency domains. Such an analysis is performed through continuous wavelet transforms (CWT), which offers good time and frequency localization and are employed to transform the PCA eigenvectors. The details of the method is explained in Section 2.3.2.

2.6.3 Analysis and Example

The big-data AFM approach is demonstrated by performing piezoresponse force microscopy on a ferroelectric BFO thin-film sample on an ITO substrate, repeated with two different excitation waveforms.

In the first case study, the AFM scan is performed in contact mode (Cypher AFM, Asylum Research), where the excitation signal is routed to the probe tip (CDT-NCHR probe, Nanosensors) and the topography is shown in Figure 2.12a. The AWG unit is used to synthesize a band excitation signal to excite the tip-sample contact around its resonance frequency. Figure 2.12b shows the excitation signal for one pixel, containing a band of frequencies between 1.1 and 1.45 MHz with amplitude of 0.5 V. The excitation response is repeated continuously for 256 pixels in each scan line. After acquiring and saving the deflection signal through DAQ unit (sampling rate 28 MHz), the data is transferred to hard drive and saved. The data matrix contains 256^2 rows corresponding to scan pixels and each row contains 2^{16} data points. The obtained data is reshaped and PCA is performed. The first 5000 eigenvalues of the decomposition are shown in Figure 2.12c, where a fast drop-off is evident for the first 20 eigenvalues. Visual inspection of the first 20 PCA loading maps (not shown here) proves that the first 20 modes contain all relevant information and the higher modes only contain noise. The First PCA loading map and the time-frequency analysis of its corresponding eigenvector is shown in Figures 2.12(d,e). The first PCA mode reveals the spatial variation of the average piezoresponse over the mapped area, while the eigenvector shows the time-frequency behavior of this mode. The presence of a resonance peak around 1.2 MHz is clear and there is another response around 2.5 MHz. In order to understand this behavior, the phase coherence analysis is performed, This is a measure of the correlation between the excitation signal and the first eigenvector in the time-frequency plane. Interestingly, only the response around the resonance is correlated with the excitation signal and the higher frequency response has a low coherence and therefore, irrelevant to the vertical piezoresponse. Further analysis of probe torsional motion and its natural frequency

shows that the response is perhaps due to torsional movement of the cantilever. The phase values are shown by the black vectors in Figure 2.12f, where the phase is around 180°, 90°, and 0 ° before, during, and after the resonance. The advantage of big-data AFM is already evident by this analysis. The excitation signal can have any arbitrary form and the measurements reveal the complex dynamics of the probe. Further, the time-frequency analysis reveals valuable information on the correlations between the excitation and response and characterizes the phase responses. Contrary to conventional AFM measurements, where the phase responses are highly frequency dependent, the phase measurements do not show any lags due to filter and system errors.

As mentioned, the PCA analysis reveals almost 20 orthogonal modes with relevant information. The data is reconstructed based on these 20 modes. The first 20 eigenvectors are filtered in time-frequency domains by only considering information that has phase coherency of 0.5 and greater and frequency in the range of excitation signal. The inverse continuous wavelet transformation of the first 20 eigenvectors are obtained and the data matrix is reconstructed. The signal-to-noise ratio of the truncated data is enhanced and the data can further be analyzed with a physical model to reveal intrinsic properties of the sample.

The reconstructed data of each pixel is fitted to a SHO model and the intrinsic amplitude, resonance frequency, and quality factor are found and illustrated in Figure 2.13. The variations in topography, amplitude, quality factor and resonance maps seems uncorrelated since these parameters are independent of each other. The topography reveals the surface roughness and the amplitude map shows the heterogeneous piezoresponse magnitude. In addition, the map of resonance frequency clearly shows distinct frequencies on grains and grain boundaries of the BFO sample. Thus, the electromechanical properties of the sample are characterized during one scan without resonance tracking and feedback loops. The mapping of R^2, the fitting coefficient of determination (Figure 2.13d) suggests a high fidelity of SHO regression analysis, with R^2, values ranging from 0.91 to 0.99 (within one standard deviation), which demonstrates the capability of big-data AFM in capturing the physics of probe near its resonance frequency with high statistical significance.

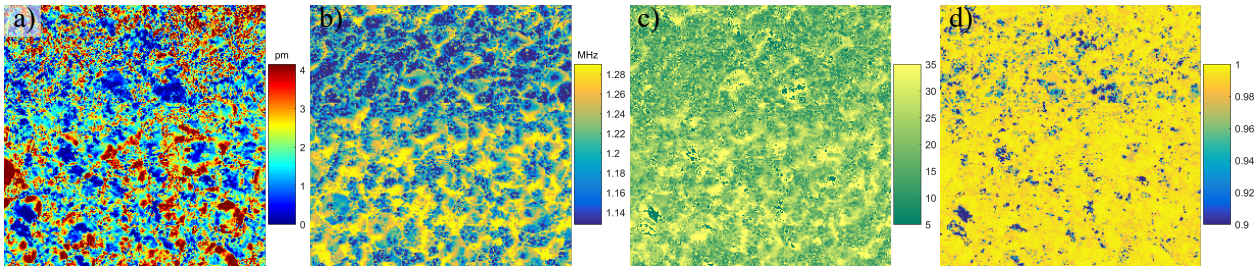

Figure 2.13: Intrinsic properties of BFO sample. SHO fitting of big-data AFM reveals (a) intrinsic amplitude, (b) resonance frequency, (c) Quality factor, and (d) fitting R^2 maps.

Big-data AFM can further shed light on ferroelectric properties of the sample. In order to characterize the ferroelectric properties of the sample, the process is repeated on an identical area of the sample with a different excitation signal. A separate experiment (switching spectroscopy-PFM, Asylum Research) is performed in advance to measure the coercive voltage of the sample (3 V). The AWG unit is used to synthesize a band excitation signal and a sinusoidal signal, concurrently. The band excitation signal (with a frequency band of 1.1–1.45 MHz and amplitude of 0.5 V) is used to excite the resonance-enhanced piezoelectric response, while the sinusoidal waveform with a fixed frequency of 73 kHz and amplitude of 5 V is used to switch the ferroelectric orientation of the sample during the scan.

Figure 2.14a shows the time-frequency analysis of the drive signal for a pixel, where a linear time-varying chirp (1.1–1.45 MHz) and fix frequency sinusoidal (73 kHz) waveforms are evident. While performing AFM scan with a rate of 0.67 Hz/Line, the external DAQ is used to acquire the AFM cantilever motion and save the data. The data matrix contains 256^2 rows for all AFM grid points and each row contains 2^{16} data points. The obtained data matrix is reshaped, principal component analysis is performed, and the first 4000 eigenvalues are shown in Figure 2.14b. The first PCA mode has much higher variance followed by a fast drop-off of eigvenvalues to more than two orders of magnitude for only the first 7 modes. Note that there are 2^{16} eigenvalues, but only the first 4000 eigenvalues are found using a randomized singular value decomposition algorithm. The first PCA eigenvector reveals interesting behaviors. Figure 2.14c shows the first eigenvector as a function of the excitation

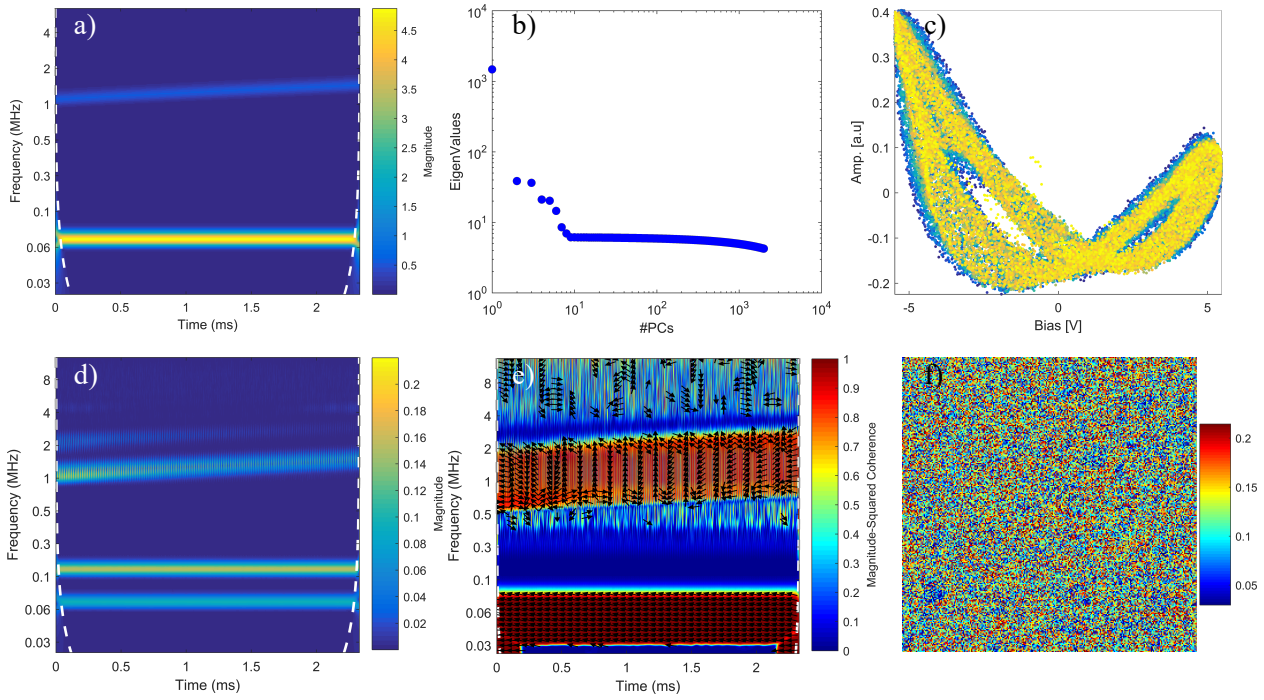

Figure 2.14: Ferroelectric properties of BFO sample obtained with big-data AFM. (a) Time-frequency representation of excitation signal, (b) eigenvalues of PCA analysis, (c) the 1$^{\text{th}}$ PCA eigenvector as a function of excitation signal, (d) time-frequency representation of the 1$^{\text{th}}$ eigenvector, (e) phase coherence between the eigenvector and the excitation signals, and (f) the 1$^{\text{th}}$ PCA loading maps.

signal, clearly revealing butterfly hysteresis loop, a signature of ferroelectric materials. It is observed that under excitation biases larger than the coercive voltage (∼3 V), the sign of the deflection signal switches due to the change in piezoelectric orientation of the sample under the charged tip. The time-frequency analysis of this eigenvector, offered in Figure 2.14d, explains the behavior. Compared to the previous example, the resonance peak is replaced by an intermittent time-varying response around 1.2 MHz. The phase coherent analysis (Figure 2.14e illustrates a continuous change of phase for a pixel time of 2.3 msec. The phase values are around 180° when the orientation is upward, 90° when switching from upward to downward domain occurs, 0° when the domain is downward and finally -90° when switching from downward domain to upward domain. There are two responses around 73 kHz

and 146 kHz without variation in time and constant phase values of 180°. The response at 146 kHz has zero phase coherence due to its quadratic nature. This lower frequency responses are the first harmonic and second harmonic responses to the sinusoidal excitation waveform caused by induced piezoelectricity and electrostatic effects. The PCA loading map in Figure 2.14f shows a uniform responses (except on sample defects) showing a uniform ferroelectric switching throughout the scanned area.

The big data AFM is better than the current methodologies in many ways. First, is the availability of multi-dimensional data for each pixel of the image that allows measuring and identifying transient and stationary phenomena in AFM measurements. While the lock-in methods only provide one or few amplitude and phase responses as a function of frequency without providing temporal information of the transient phenomena, big data AFM provides multiple harmonics and resonance modes arising from nonlinear probe interactions. Further, multi-modal imaging is easily possible as the whole frequency spectrum of the lateral and vertical probe motions and other channels are saved. In addition, capturing multiple signals allows for utilizing the adaptive and data-driven methods that can correlate, deconvolute and identify highly coupled phenomena during AFM measurements. Second, unlike the classical SPM imaging which has fixed number of pixels, this method allows for multi-resolution imaging with having higher pixels in a trade for having a higher noise and *vice versa*. This can systematically overcome one of the most difficulties with current AFMs which is finding small features in a big area through using cross-correlation algorithms. Third, this allows for creation of AFM data repositories and libraries throughout the material science community which enables a deep data approach toward development of unbiased selection of material methods and models. This method can promise to extend empirical knowledge of materials, especially for complex energy storage material systems with nonlinear coupled physics and competing degrees of freedom.

2.7 Conclusions

In this chapter, new approaches for measuring the AFM deflection signals are presented. The multi-harmonic DART is a lock-in based method, capable of measuring the nonlinear phenomena while tracking the resonance frequency of tip-sample contact. The multi-harmonic DART requires specific instrumentation that are not available to all AFM users. A sequential excitation method overcomes the difficulties associated with feedback loop errors. Further, a big-data AFM approach is introduced and the preliminary implementation and results are offered. The big data AFM is an unusual and unique instrument that connects physical and data sciences, providing an ideal platform to develop and test methodologies ranging from data acquisition, processing, analysis, to artificial intelligence. These methods are the basis of deflection detection for techniques that are explained in the following chapters.

Chapter 3

SCANNING THERMO-IONIC MICROSCOPY FOR PROBING LOCAL ELECTROCHEMISTRY AT THE NANOSCALE

3.1 Introduction

The worldwide energy economy is shifting focus from extraction and consumption of fossil fuels towards a diverse, multidirectional, and asynchronous network of energy sources and demands. There is a critical need for electrochemical materials that efficiently interconvert and/or store electrical and chemical energy. These include more robust electrode materials for large and small scale battery systems [76–78], fuel cells or flow batteries [79–81], electrocatalysts for efficient electrosynthesis of liquid transportation and storage fuels [82], and photoelectrochemical materials that directly convert solar energy to fuels [83]. At present, a universal challenge facing the development of electrochemical materials is the lack of understanding of physical and chemical processes. A deep fundamental understanding of the microscopic mechanisms, as well as technological advancement, is largely hampered by a lack of experimental techniques that can directly probe electrochemical processes at the nanoscale at local length scales in the 10–100 nm regime. A growing body of research shows that the composition, structure, and properties of electrochemical materials near active interfaces often deviate substantially and inhomogeneously from those of the bulk, and the electrochemistry at this length scale is still poorly understood [80, 84, 85]. Acquiring this understanding requires a new generation of imaging techniques that can resolve local chemistry and fast dynamics in electrochemical materials at the time along length scales relevant to strongly coupled reaction and transport phenomena. This offers a new opportunity for microscopy development.

Conventional electrochemical characterization techniques are very difficult to scale down

as they are mostly based on the measurement of current: this requires the detection of small currents on the order of pA at the nanoscale [86]. Custom-made ion-conducting electrodes have been developed for scanning electrochemical microscopy [87]. However, the spatial resolution is usually no better than micrometers [88,89], and the fabrication process is complex. Electrostatic force microscopy and Kelvin probe force microscopy have been applied to study local electrochemical processes [86,90]. Yet the spatial resolution is limited because of long-range electrostatic interactions. In addition, the data are often ambiguous and, in turn, are difficult to interpret. In the last several years, researchers have realized that Vegard strain [91,92] can provide an alternative imaging mechanism with high sensitivity and spatial resolution for nanoscale electrochemical characterization. The initial attempt focused on atomic force microscopy (AFM) topographic mapping of lithium ion electrodes during charging and discharging. However, the volume evolution that is induced by the change in lithium ion concentration [93] reflects the accumulation of Vegard strain over both space and time. Later on, electrochemical strain microscopy (ESM) was proposed, and focused on local and instantaneous fluctuations in ionic species induced by an AC voltage applied through a conductive scanning probe tip [35,94–96]. While these techniques have provided considerable insight into local electrochemistry, isolating Vegard strain from other electromechanical mechanisms such as piezoelectric effect, electrostrictive effects, electrostatic interactions, and capacitive forces is often non-trivial [2,97]. Furthermore, it is highly challenging to integrate local ESM with global electrochemical measurement *in-operando* because the charged scanning probe is often affected by global voltage perturbations.

In this chapter, a novel technique for probing local electrochemistry at the nanoscale, termed scanning thermo-ionic microscopy (STIM), is presented [38,39,54]. This new form of microscopy overcomes the aforementioned difficulties. The new technique utilizes thermally, instead of electrically, induced Vegard strain, thus eliminating contributions from other electromechanical strains and interference from global electrical perturbations, as presented in Section 3.2. This technique can be applied to investigate a wide range of electrochemical systems including electrode materials for lithium ion batteries, solid oxide electrolysis cells

(SOEC), and solid oxide fuel cells (SOFC), which is presented in Section 3.3.

3.2 Principle of Method and Implementation

3.2.1 Concept of the Method

The concept of STIM is built on three observations. First, when the ionic concentration oscillates in a solid, the associated volume also fluctuates due to Vegard strain [91,92]. The Vegard strain is defined broadly as a lattice volume change associated with a concentration change in the ionic species. This results in a mechanical vibration that can be measured locally via a scanning probe, shown schematically 3.1. Such dynamic-strain-based detection has been applied in a variety of scanning probe microscopy (SPM) techniques, including piezoresponse force microscopy (PFM) [98–100], electrochemical strain microscopy (ESM) [35, 94–96], and piezomagnetic force microscopy (PmFM) [101, 102]. Second, the fluctuation of ionic concentration may be driven by an oscillation in its electrochemical potential, which can be induced by the gradient in hydrostatic stress and temperature, simultaneously. Finally, the characteristics of ionic oscillation and electrochemical strain probed via the scanning probe are linearly correlated and could reveal valuable information on the local ionic species, concentration, and diffusivity. Thus, STIM technique could provide a window into local electrochemistry at the nanoscale. In contrast to ESM where the ionic oscillation is driven by an applied electrical potential [33], the new method probes the concentration fluctuations of ionic species or electronic defect caused directly or indirectly by temperature oscillation induced by a heated scanning probe. Overall, STIM has several potential advantages over ESM.

In order to fully appreciate the concept of STIM, it is necessary to briefly review the theory of stress-induced diffusion developed by Larch and Cahn in the 1970s [34, 103],

$$\frac{\partial c}{\partial t} = \nabla \cdot (D \nabla c) + \nabla \cdot (\frac{DFz}{RT} c \nabla \phi) - \nabla \cdot (\frac{D\Omega}{RT} c \nabla \sigma_h), \tag{3.1}$$

where D, z, and Ω are the diffusivity, charge, and partial molar volume of an ion, F and R are the Faraday and ideal gas constants, and T and t are the absolute temperature and

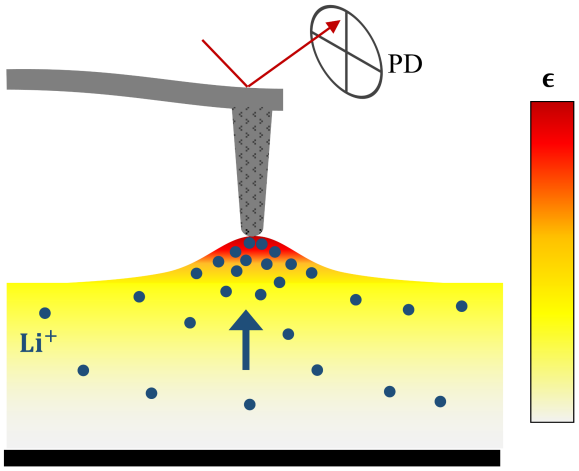

Figure 3.1: Schematic of Vegard strain detection in scanning probe microscopy. Higher ionic concentration induced by changes in electrochemical potential results in expanded molar volume that can be measured from the deflection of the cantilever and the reflected laser beam, received in a photo detector (PD).

time, respectively. The three driving forces for ionic oscillation are gradients in ionic concentration ∇c, electric potential $\nabla \phi$, and hydrostatic mechanical stress $\nabla \sigma_h$, corresponding to three terms on the right side of Equation 3.1. The second term explains the principle of ESM, where the alternating electric potential drives the oscillation of ionic concentration. Another method of inducing local ionic fluctuation is to apply hydrostatic stress by mechanically vibrating the scanning probe (the third term). However, this implementation complicates the measurement of the resulting displacement as the nature of oscillation will be dominantly dependent on the viscoelastic properties of the sample under the probe.It also severely limits the magnitude of stresses possible. In order to impose an oscillating stress while simultaneously measuring the resulting local vibration through the scanning probe, a local temperature oscillation with angular frequency ω is resorted,

$$\Delta T_{AC}[\omega] = \Delta T \exp(i\omega t), \tag{3.2}$$

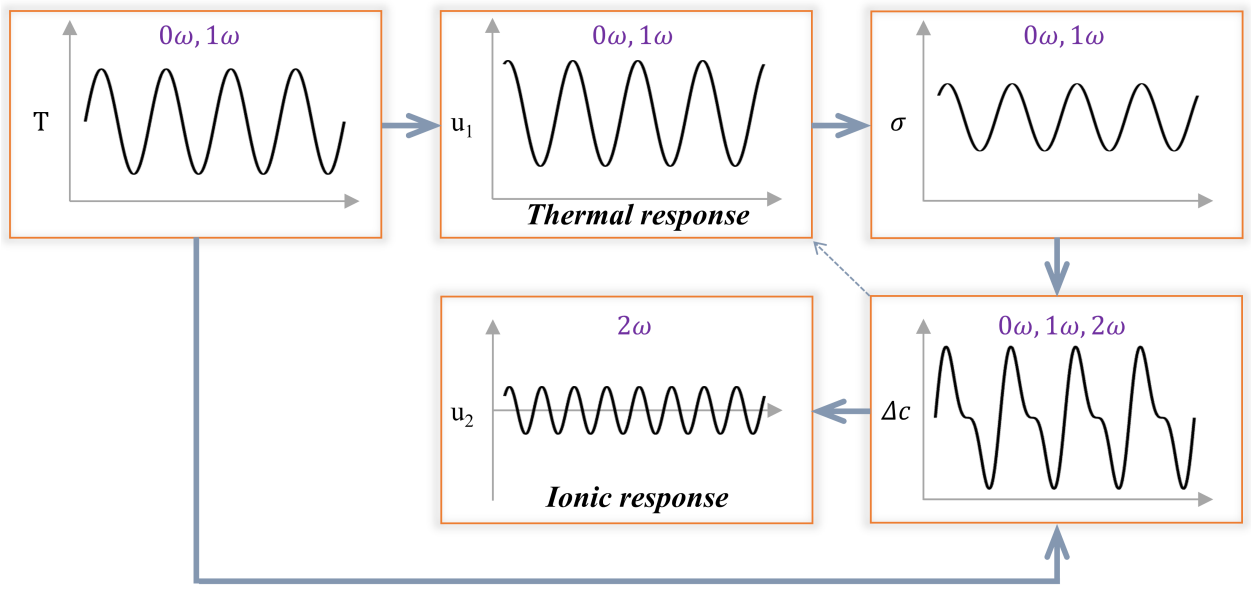

Figure 3.2: Graphical representations of oscillating temperature, stress, ionic concentration, and the first and second harmonic components of scanning thermo-ionic microscopy displacements. The oscillation of temperature causes thermal expansion that induces a fluctuating thermal stress. The simultaneous temperature and stress oscillations result in an ionic concentration oscillation and subsequently displacement oscillation at a few distinctive frequencies.

which results in local oscillation of thermal strain $\Delta\boldsymbol{\epsilon}^*$ and hydrostatic stress $\Delta\boldsymbol{\sigma}_h$,

$$\Delta\boldsymbol{\epsilon}^*[\omega] = \alpha\Delta T\exp(i\omega t)\boldsymbol{I}, \quad \Delta\boldsymbol{\sigma}_h[\omega] = \frac{1}{3}\operatorname{Tr}\boldsymbol{C}(\Delta\boldsymbol{\epsilon}[\omega] - \Delta\boldsymbol{\epsilon}^*[\omega]) = \Delta\sigma_{h_0}\exp(i\omega t), \tag{3.3}$$

where α and $\boldsymbol{C}$ are the thermal expansion coefficient and elastic stiffness tensor of the material, $\boldsymbol{\epsilon}$ is the total strain consisting of thermal strain $\boldsymbol{\epsilon}^*$and elastic strain, Tr denotes the trace of the matrix, $\Delta\sigma_{h_0}$ is the amplitude of hydrostatic stress oscillation, and $\boldsymbol{I}$ is the second rank unit tensor. Note that thermal expansion results in a vibration that is the first harmonic to the temperature oscillation, as schematically shown in Figure 3.2, and thus the first harmonic response $u_1[\omega]$ yields local thermomechanical properties.

However, there are further consequences and implications of this oscillating thermal stress, which drives oscillation in ionic concentration. By Taylor expanding T around an average temperature, T_0, and substituting into Equation 3.1, we obtain the first and the second

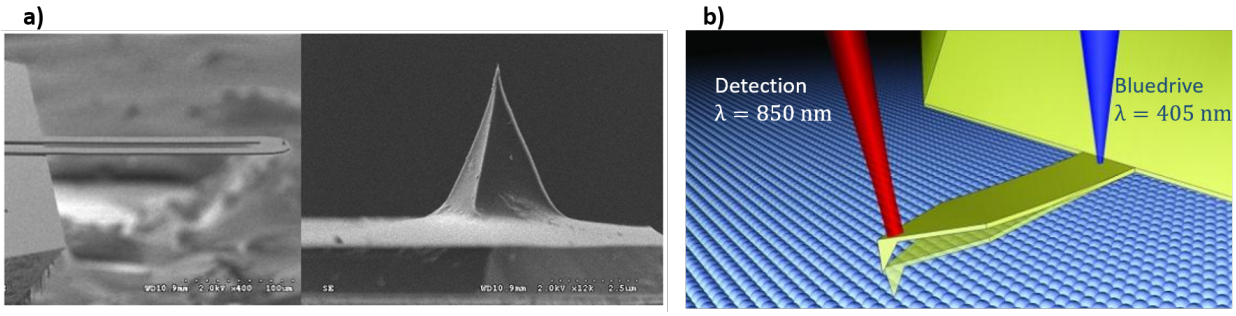

Figure 3.3: STIM excitation sources; (a) Photos of two-leg scanning thermal probe and (b) blueDrive^{TM} photo-thermal excitation module. Images used with permission of ANASYS Instruments and Asylum Research.

harmonic components of ionic oscillation:

$$\Delta c[\omega] = -\nabla \cdot (\frac{D\Omega c_0}{RT_0}\nabla\sigma_{h_0}) \exp(i\omega t), \quad \Delta c[2\omega] = \nabla \cdot (\frac{D\Omega c_0}{RT_0^2}\Delta T\nabla\sigma_{h_0}) \exp(i2\omega t), \qquad (3.4)$$

which in turn induce the first and second harmonic Vegard strains and the corresponding displacements shown in Figure 3.2. Thus, the first harmonic STIM response $u_1[\omega]$ consists of contributions from both thermal expansion and Vegard strain. In general, this is dominated by thermal expansion and thereafter referred to as *thermal response*, whereas the second harmonic STIM response $u_2[2\omega]$ is purely caused by Vegard strain associated with ionic oscillation and is thereafter referred to as *ionic response*. By measuring displacements associated with thermal and ionic responses induced by the fluctuating temperature and thermal stress at respective harmonics, information on both thermomechanical and ionic properties of materials can be obtained. It should be noted that other nonlinear sources such as thermally-induced defect formation and thermally driven transport (Soret/Dufour effects) are ignored here. However, like stress-driven transport, strong contributions from these sources are expected to appear in the higher harmonic responses, leading to a higher sensitivity of STIM to local shifts in defect concentration.

3.2.2 Excitation Sources

The nanoscale temperature oscillation, necessary to stimulate the hydrostatic stress and local concentration fluctuations, is achieved through two different methods. Namely, resistive heating and photo-thermal excitation are both implemented on commercial AFM systems. Initially, STIM was implemented through using headed probes (ThermaLever™ AN2-300, Anasys Instruments) (Figure 3.3a), on an Asylum Research MFP-3D AFM. The two-leg thermal probe has a micro-fabricated solid state resistive heater at the end of the cantilever, enabling local heating. When an AC current $I[\frac{\omega}{2}] = I_0 \cos(\frac{\omega}{2}t)$ is passed through a heated probe with resistance β, the resulted power dissipation p is given by:

$$p[\omega] = \beta I^2 = \frac{\beta I_0^2}{2}(1 + \cos(\omega t)), \tag{3.5}$$

which has a DC component and an AC component with the angular frequency ω. Consequently, the power dissipation generates a DC temperature raise ΔT_{DC}, and a temperature oscillation with amplitude ΔT_{AC}. The temperature of the probe $T[\omega]$ can be determined by:

$$T[\omega] = T_{amb} + \Delta T_{DC} + \Delta T_{AC} = T_0 + \Delta T \cos(\omega t + \theta), \tag{3.6}$$

where T_{amb} is the initial temperature of probe and θ is the phase delay of temperature oscillation with respect to the drive signal. Equation 3.6 illustrates the principle of the temperature perturbation that is essential to STIM. The heated probe can elevate the temperature of the sample to more than 600 °C [104] with 0.076 °C precision at 1 MHz bandwidth [105], therefore is highly suitable for STIM application. In this implementation the temperature oscillation is the second harmonic to the AC current because of the quadratic relationship between power and current. As a result, the probe deflection contains the thermal response $u_1[\omega]$ at the second harmonic and the ionic response $u_2[2\omega]$ at the fourth harmonic with reference to the input current $I[\frac{\omega}{2}]$, which reflect the thermomechanical and electrochemical properties of the material, respectively.

Alternatively, local heating and temperature fluctuation can also be realized through a photo-thermal approach, utilizing a 405 nm laser with modulated intensity aligned at

the base of a gold coated cantilever (Multi75GD-G, Budget Sensors) or any regular AFM probe, implemented on an Asylum Research Cypher ES AFM equipped with blueDrive™ photo-thermal excitation module, (Figure 3.3b) [106]. The temperature profile spans several orders of magnitude based on laser power, material, cantilever geometry, location of the laser spot, coating, and environment [107]. These should be carefully calibrated and optimized before STIM operations. Under photo-thermal excitation, the laser power and thus the local temperature is modulated directly. According to Equation 3.4, the first and second harmonic deflection responses —with respect to the laser being driven at frequency ω— are the thermal $u_1[\omega]$ and ionic $u_2[2\omega]$ responses, respectively.

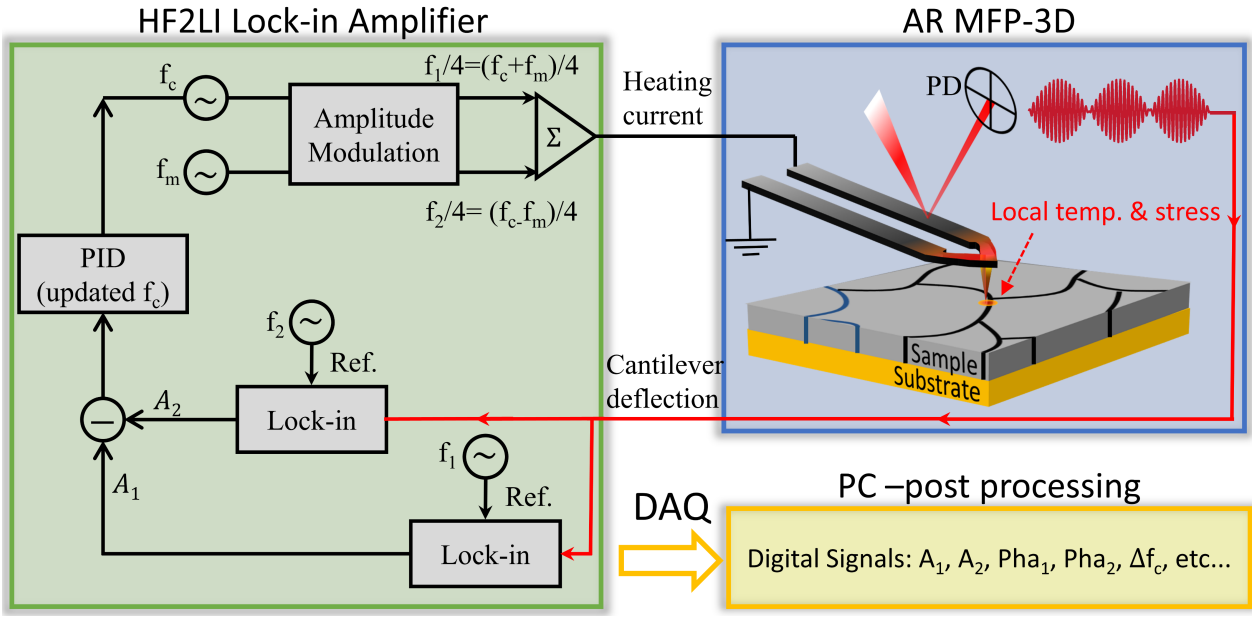

Figure 3.4: Schematic implementation of the fourth harmonic dual amplitude resonance tracking (DART) scanning thermo-ionic microscopy (STIM). The lock-in amplifier synthesizes a dual AC signal (at frequencies $\frac{f_1}{4}$ and $\frac{f_2}{4}$) and the output of the lock-in is used for bimodal excitation of the thermal probe. The AFM deflection signal is routed to the lock-in input and the fourth harmonic deflection responses at both frequencies (f_1 and f_2 around the contact resonance) are detected (amplitude and phase). The internal PID is used to regulate the difference between the detected amplitudes and adjust the carrier frequency f_c. The lock-in amplifier streams the detected information to a PC synchronous to AFM in real-time.

The photo-thermal heating is advantageous over the resistive heating excitation due to the following issues associated with heated probes. The heated probes contain a solid state resistor composed of heavily doped silicon near the probe tip as well as two electrical paths on each leg probe with light doped silicon. This connects the current source to the resistor. Due to the large surface area of the doped silicon, the electrostatic forces between the body of probe cantilever and sample surface are inevitable when the current passes through the resistor. Fortunately, the forces are first and second harmonic responses to the drive current, and do not interfere with the ionic measurements in the 4^{th} harmonic response STIM measurements. Furthermore, the electrical conductivity of heated probes vary significantly from probe to probe, which makes the absolute temperature determination very difficult, requiring careful calibrations. On the other hand, photo-thermal heating can be very well controlled as the power of the laser source can be controlled in real time.

3.2.3 Deflection Detection

Detection of the respective harmonic response of the cantilever deflection is non-trivial since it is typically a small signal with a low signal-to-noise ratio. As mentioned in Chapter 2 , several techniques have been specifically developed in this work for the problems of interest and implemented on AFM systems. Advanced lock-in amplifiers and full information acquisition has been leveraged in STIM to reveal the ionic response.

As was explained in previous section, both thermal and ionic responses have well-known frequency modulations due to the forced harmonic nature of excitation sources. Lock-in amplifiers (LIA) can be used to find the amplitude and phase of the noisy deflection signal while the LIA reference signal is served as the excitation source. Most of the commercial AFM controllers have a few built-in LIAs. This allows for measurements of the first harmonic (which requires only one LIA) or higher harmonics (which requires at least two LIAs) responses. For the ionic response in STIM mode, the associated deflection amplitudes are on the order of 1–20 pm, which is comparable to the noise floor of the AFM deflection signal obatined via optical beam deflection. In order to accomplish higher signal-to-noise ratio,

STIM measurements are resonance-enhanced, *i.e.* the excitation frequency is chosen in a way that the deflection signal frequency is around the cantilever-sample contact resonance frequency. This tip-sample contact resonance frequency varies inhomogeneously over the scanned area of the sample and thus having a fixed excitation and detection frequency will cause topography crosstalks during STIM scanning. To circumvent this, the dual amplitude resonance tracking (DART) technique is adopted(Figure 3.4) [69] implemented with the thermal probe. Four lock-ins are thus necessary to obtain the thermal (off-resonance) and ionic response (resonance-enhanced) mappings simultaneously, is beyond the capabilities of commercial AFM controllers and requires additional instrumentation. The new test setup is designed and implemented in the Shenzhen Key Laboratory of Nanobiomechanics, Shenzhen Institute of Advanced Technology, Chinese Academy of Science, where an Asylum Research MFP-3D Bio AFM is merged and synchronized with a Zurich Instrument HF2LI lock-in amplifier and a proportional, integral, derivative (PID) controller in combination. The implementation details are fully explained in Section 2.4.

The design of PID gains, the appropriate modulation frequency f_m, and the heating power amplitude depends on many parameters. The parameters, include probe geometry, probe natural frequency, scan speed, and the average ionic responses of the sample. PID parameters were coarsely tuned according to guidelines reported by Abramovitch *et. al* [108], followed by fine-tuning to optimize controller behavior in each set of experimental conditions. Lacking such a system at UW, resonance tracking is not possible for STIM, and experiments are restricted to point-wise spectroscopic studies, as shown later.

The DART measurements are prone to several issues including the errors in tracing the resonance frequency, slow feedback response, topography cross-talks, and the lack of nonlinear and transient tip-sample interaction dynamics in measurementsSection 1.3. Alternately, STIM was implemented through using full information acquisition of cantilever motion in real time with a high sampling rate. This eliminates the need for the closed loop measurements and resonance tracking, allows for faster scanning and reveals the full dynamics of probe. The huge data sets collected during the experiments allow for information-based analysis,

even without known the dynamics of the interaction in advance. Full details of this method and the analysis flow is presented in Section 2.6.

3.3 Application

3.3.1 Application to Ceria

Pure ceria (CeO_2), and ceria-based ion conductors such as $Ce_{1-x}M_xO_{2-\delta}$ (where M = Y, La, Gd, and Sm) exhibit electronic insulation under oxidizing conditions [109, 110]. When reduced from Ce^{4+} to Ce^{3+}, oxygen vacancies and charge compensating mobile electrons (small polarons) are formed [111]. Tschpe *et al.* [112] first reported that nanocrystalline ceria shows remarkable electronic conductivity in air which may arise from space-charge effects near the grain boundaries [113–115]. Positive charge accumulates in the grain boundary core from segregated impurities, surface defects, and other charged species, which is compensated by a depletion of oxygen vacancies and an accumulation of small polarons (electron +lattice distortion) in a diffuse region known as the space charge region. The charge trapped in the grain boundary core is compensated by space charge regions on both sides of the interface. This theory is supported by a series of simulations and models [115, 116], however observing and probing the diffuse space charge region is rather challenging. Chen *et al.* [36] and Kumar *et al.* [117, 118] utilized ESM in separate studies and observed that such a diffuse space charge region exists and is localized at the grain boundaries of ceria. This makes ceria an interesting yet challenging material system that is characterized with STIM.

3.3.2 Application to Halide Perovskites

Halide perovskite solar cells based on $CH_3NH_3PbI_3$ are one of the most promising material systems in the next generation of photovoltaic technologies [119, 120]. In the last eight years their conversion efficiency has tremendously increased to higher than 22%, currently making this the fastest advancing solar cell technology [121]. At the microscopic level, halide perovskites exhibit exotic phenomena including photo-carriers, ionic defects, and spontaneous

polarization, which are still not understood. In fact, there lacks a method that can examine the local photovoltaic efficiency and correlate the device performance with microstructure properties [122].

The macroscopic measurements of transient current (I-V curves) reveal large I-V hysteresis which is potentially due to the migration of charged Pb, MA, and I vacancies and ions [123–126]. Researchers tried to map the redistribution of surface potential associated with this ionic movement through KPFM, but suffered from insufficient spatial resolution [127]. Also, ESM has been employed to probe the local concentration of ionic species, however the predicted ferroelectric nature of halide perovskites means that the ionic strain response measured in ESM is interfered by piezoelectric strain [128, 129]. STIM seems to be particularly suitable for probing the concentration of ionic species and diffusivity in halide perovskites, since the measured Vegard strain is induced by thermal stress fluctuations. Unlike ESM, STIM has the ability to measure and probe the local concentration and diffusivity fluctuations even when the device is under test. The combination of nanoscale measurements such as STIM and global measurements including macroscopic I-V curve measurements, electric polling, and light illuminations can reveal microscopic mechanisms that are responsible for the macroscopic performance of halide perovskite solar cells.

3.4 Results and Analysis

The dynamic-strain responses in atomic force microscopes can be obtained through different acquisition techniques developed in the context of this work for broad ranges of AFM modes (Chapter 2). This section includes analysis of STIM responses acquired through lock-in DART measurements and full information acquisition techniques (Section 3.2.3 for detailed discussion) in point-wise and scanning modes. Measurements were obtained through different excitation sources explained in Section 3.2.2.

3.4.1 Point-wise Measurements with Lock-in

The feasibility of the STIM concept is domonestrated by the point-wise thermal and ionic responses of two types of samples at respective harmonics. One is nanocrystalline Sm-doped ceria that is a good ionic conductor [112], and the other is polymeric polytetrafluoroethylene (PTFE) that serves as a control sample (no ionic conductivity). The detection was performed with LIA, where the driving frequency was swept across tip-sample contact resonance frequency, and the corresponding harmonic responses of probe deflection signal was measured. The STIM implementation was based on resistive heating. As seen in Figure 3.5a, both ceria and PTFE exhibit substantial thermal response measured at the second harmonic under the resistive heating, as expected in any material with non-zero thermal expansion coefficient regardless of its ionic characteristics. The higher contact resonance frequency of ceria at 123.4 kHz indicates its higher elastic modulus compared to PTFE with a resonance frequency of 118.7 kHz. Furthermore, after fitting the experimental data with the damped driven simple harmonic oscillator model [64, 130], the quality factors for ceria and PTFE are obtained as 57.7 and 46.4, which indicate higher viscous energy dissipation in PTFE. The corresponding intrinsic thermal response amplitudes (after correcting the peak value using the quality factors) are determined to be 38.2 pm and 44.3 pm, suggesting that the thermal expansion of PTFE is higher than that of ceria, as expected [131, 132]. Thus the local thermomechanical properties of solid materials can indeed be obtained from the STIM thermal response.

Further insights can be provided from the ionic response measured at the fourth harmonic under similar conditions(Figure 3.5b). First of all, substantial higher ionic response is observed in ceria, while that of PTFE is almost negligible. This is more evident after the data is analyzed using a damped driven simple harmonic model that yields a quality factor of 49.52 for PTFE and corresponding intrinsic ionic response of 0.31 pm, consistent with its non-ionic nature. The quality factor and the intrinsic response of ceria are 55.95 and 3.31 pm. Since ionic response is proportional to ionic diffusivity according to Equation 3.4. The good ionic

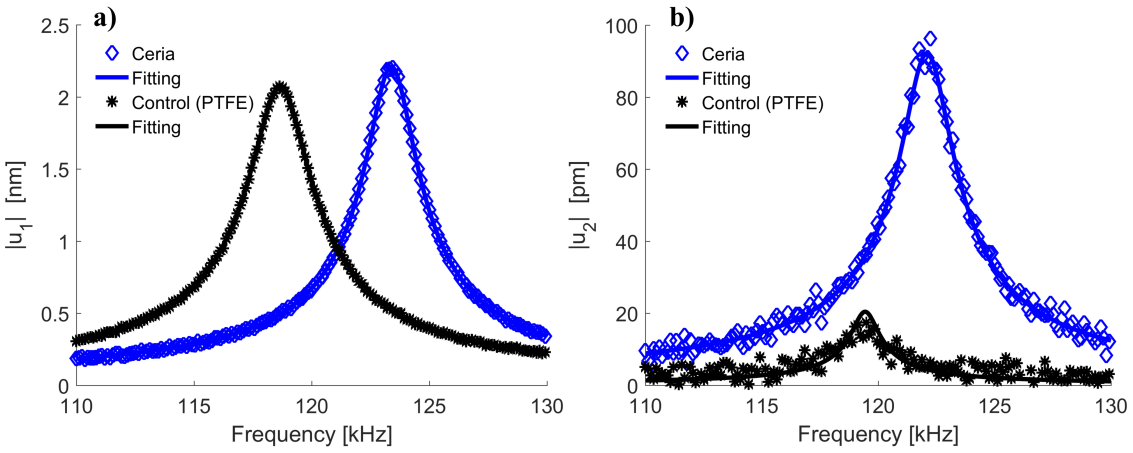

Figure 3.5: Point-wise (a)thermal and (b)ionic responses in STIM on ceria and PTFE samples using resistive heating on MFP-3D AFM, demonstrating the feasibility of STIM. While sweeping the drive signal frequency, the amplitudes of (a) 2^{nd} and (b) 4^{th} harmonic responses of the deflection signal is detected through lock-in measurements. The 2^{nd} and 4^{th} harmonic deflection signals are enhanced substantially where the temperature/ionic concentration oscillations (if any) are near the probe contact resonance.

response of ceria seen in Figure 3.5 indicates its good ionic nature. Moreover, the quality factors and the resonance frequencies (119.3 and 122.1 kHz for PTFE and ceria) obtained from thermal and ionic responses are in a good agreement, confirming the reliability of the measurements. While the ionic response of ceria is an order of magnitude smaller compared to its thermal response, the signal is sufficiently strong and clean for sensitive detection. These sets of data thus demonstrate the feasibility of STIM without ambiguity.

valuable dynamic information can be learned from the STIM ionic response, by imposing a low-frequency modulation bias, in the range of 0.1 Hz to 20 Hz, on top of high-frequency excitation bias, in the order of 30 kHz(Figure 3.6a). The modulation bias is to manipulate the local ionic concentration away from equilibrium by changing the baseline temperature, while excitation bias is to stimulate ionic oscillation for the measurement. Since their frequencies differ by more than three orders of magnitude, the low-frequency modulation bias can be viewed as DC, as far as the instantaneous high-frequency excitation bias is concerned. The

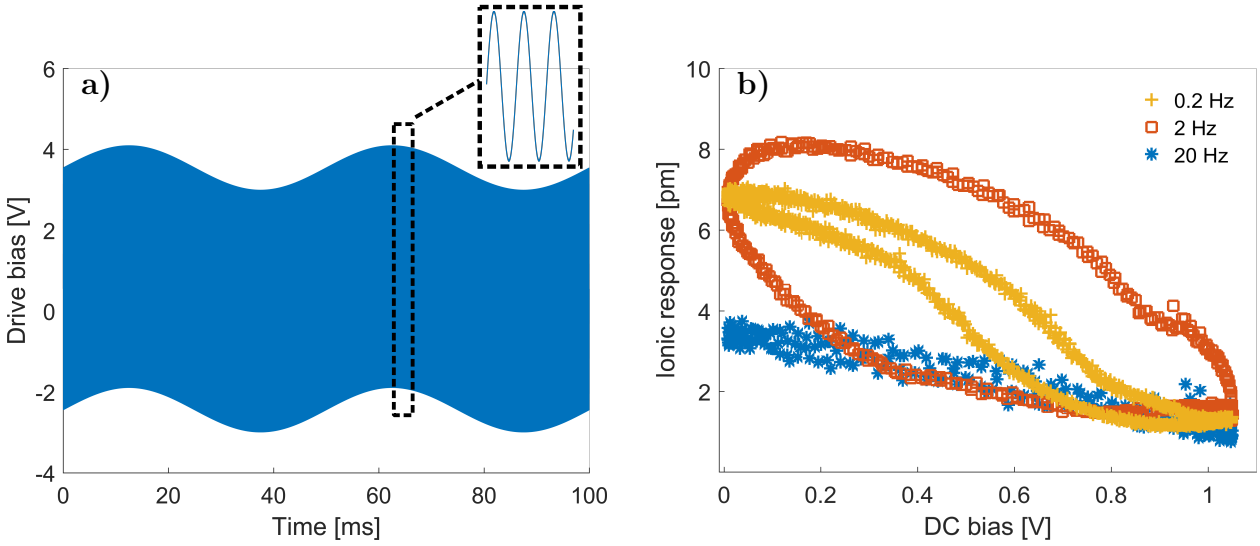

Figure 3.6: Point-wise ionic spectroscopy of ceria; (a) heating voltage applied to the thermal probe, consisting of superposition of high- and low-frequency voltage waveforms; (b) the intrinsic ionic response of ceria as a function low-frequency modulation bias under different modulating frequencies; these measurements were repeated 20 times and the average results are presented.

ionic responses of ceria measured in term of 4^{th} harmonic probe deflection induced by driving heating voltage, after correction by using a damped driven simple harmonic oscillator model, are plotted in Figure 3.6b. It is observed that with increased DC voltage and thus higher local temperature, the ionic response drops due to reduced ionic concentration underneath the probe, driven away by the higher temperature and thermal stress. The shape of this loops, qualitatively similar to ESM spectroscopy loops, is determined by the kinetics and dynamics of electrochemical reaction and therefore highly rate dependent [35, 56]. Furthermore, the loop initially opens up with an increased modulation in frequency and then closes, which can be understood as follows. For the low (0.2 Hz) and fast (20 Hz) modulation frequencies, where the ionic species are being driven much slower and faster than the typical diffusion time scale, not much hysteresis is observed. However, the intermediate frequency modulations (2 Hz), which perhaps has a time scale comparable to that of ionic diffusion, leads a phase lag and thus the loop opens up [36]. In turn, from the loop opening under appropriate modulating

frequency, dynamic information can be learned from the STIM spectroscopy studies.

3.4.2 DART-STIM Mappings

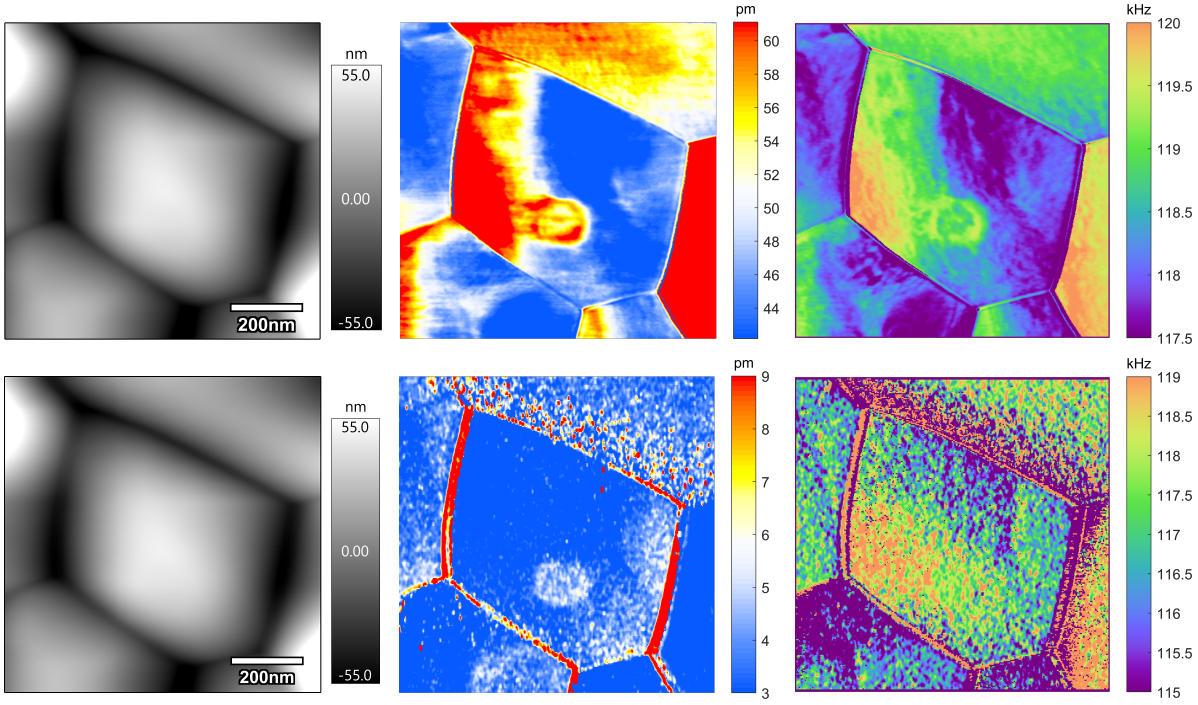

Figure 3.7: Thermal (top and middle rows) and ionic (bottom row) DART STIM mappings of ceria through photo-thermal (top row) and resistive heating (middle and bottom row). (a,d,e) Topography, (b,e,h) STIM amplitude, and (c,f,i) resonance frequency mappings. The results in each row obtained from a separate scan where the middle and bottom row scans are on similar area.

The STIM mappings of thermal and ionic responses can reveal local variations of thermomechanical and electrochemical properties of materials. In this section, the thermal and ionic STIM mappings acquired with higher harmonic dual ac resonance tracking (DART) technique are presented. The STIM experiments with resistive heating excitation requires higher harmonic measurements that are beyond the capabilities of current AFM systems and a custom-designed test setup was implemented on an MFP-3D Bio AFM combined with an HF2LI lock-in amplifier and PID (Zurich Instruments). The photo-thermal excitation was implemented on Cypher ES AFM with built-in lock-ins, which only allow for the first harmonic measurements (Section 3.2.2 for details of excitation sources). During the scan, the lock-ins measure real-time dual amplitude and phase responses of deflection signal at respective harmonics, and records the frequency of the excitation frequency for each pixel. Given these information the intrinsic properties of the tip-contact interaction including the intrinsic amplitude, phase lag, quality factor, and the resonance frequency of oscillation can be obtained in post-processing stage (Sections 2.4).

Figure 3.7 depicts the thermal and ionic STIM maps obtained with both excitation methods in a 900 nm $\times$ 900 nm region along with their contact mode topography. The top and middle rows of Figure 3.7 correspond to thermal mapping responses (each in separate scan on a different area of sample) with photo-thermal and resistive heating excitation , respectively, while the bottom row shows ionic maps obtained through resistive heating (separate scan and on similar area of the middle row). From topography mappings in Figures 3.7a,d,g, a pentagonal grain having boundaries with five neighboring grains is evident. The photo-thermal excitation was implemented using a gold coated AFM probe with in-air resonance frequency of $\sim$70 kHz (Multi75GD-G, Budget Sensors) while the resistive heating was implemented using a heated probe with an in-air resonance frequency of $\sim$30 kHz (AN2-300, Anasys Instruments). The contact resonance frequency maps of ceria in Figures 3.7c,f, therefore exhibit a different type of variation within grains, however, the thermal responses in Figures 3.7b,e show grain-to-grain variation, as well as variation within a grain with a good qualitative agreement. The variations withing the grain can be possibly caused by the ef-

fect of topography variations on nano-scale heat conduction between the thermal probe and the sample. On the other hand, the ionic response in Figure 3.7h exhibits a substantially higher amplitude at the grain boundaries, but within each grain the responses are uniformly low. Such contrast is believed to be caused by accumulation of mobile electrons in the diffuse space charge regions near the surface and at grain boundaries, as recently imaged by ESM [36, 117, 118]. In comparison with ESM results, the mappings show a sharper contrast and the existence of a diffuse space charge region on the two sides of grain boundaries are clearly evident. The core of the grain boundaries show relatively low response, which is expected due to the low mobility of oxygen vacancies at room temperature. This makes the STIM a nanoscale electrochemical characterization technique to observe and probe the space charge regions. The resonance frequency mappings in Figure 3.7c,f, acquired from the second and fourth harmonic scanning are consistent with each other, though the second harmonic one has a better signal-to-noise ratio due to the much higher amplitude of thermal response. Compared to the first implementations of STIM with single frequency excitation [39], much enhanced STIM mappings are obtained, thanks to the improved capability for tracking the resonance frequency during scanning using DART.

Finally, DART STIM ionic mappings were obtained on $CH_3NH_3PbI_3$, an emerging perovskite material for solar cells [120, 129]. It has been reported that ionic migration in $CH_3NH_3PbI_3$ occurs under light illumination or electric polling [133], which has significant implication to its photovoltaic performance.

Figure 3.8 shows the STIM ionic response for a $CH_3NH_3PbI_3$ film on a hole-collecting FTO/PEDOTS:PSS substrate, in which rough topography is observed and large variations in ionic response are evident in Figure 3.8b. The enhanced responses are mainly at the grain boundaries , reflecting their higher ionic activities, and are extremely sensitive to external illumination condition and sample degradation. The resonance frequency shown in Figure 3.8c is rather uniform with one standard deviation of $\sim$1 kHz, indicating homogeneous mechanical stiffness of the sample. The amplitude response seems correlated with the resonance frequency, possibly because shifts of resonance frequency due to ionic concentration. The

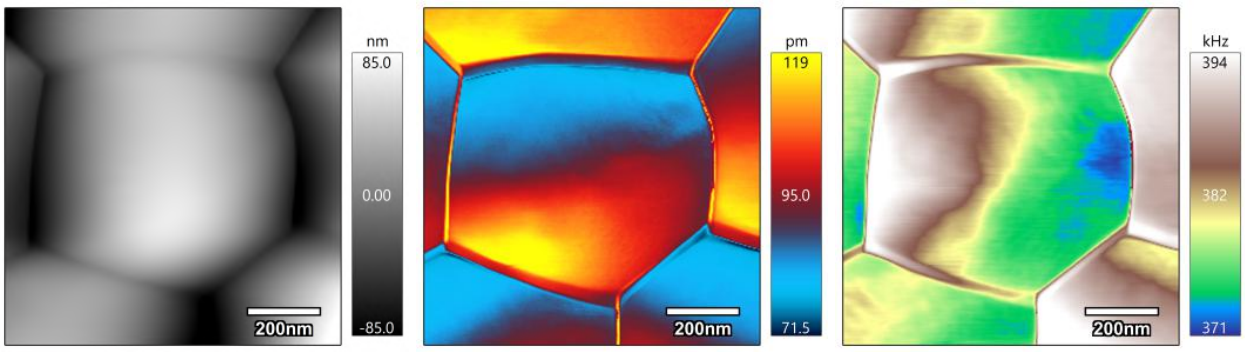

Figure 3.8: Ionic mapping of $CH_3NH_3PbI_3$ on FTO/PEDOTS:PSS by STIM; (a) schematics of STIM through photo-thermal heating, STIM mappings of (b) ionic responses (second harmonic) , and (c) resonance frequency, both overlaid on three-dimensional topography. The STIM measurements were carried out on an Asylum Research Cypher ES AFM equipped with BlueDrive^{TM} photo-thermal excitation unit that illuminates a 9 mW power modulated 405 nm laser aligned on the base of a gold coated probe (Multi75GD-G, Budget Sensors).

preliminary results reported here proves the capability of STIM to study such a phenomena at the nanoscale while the device is under global test. However, due to unstable nature of the material systems, the tests should be carried out under full environmentally control. These tests are currently being developed. Under stable conditions, STIM measurements combined with global electrical perturbation and light illumination can reveal valuable information on local ionic activity.

3.4.3 Full Information Acquisition in STIM Mappings

The lock-in measurements have certain limitations and challenges. The lock-ins receive the probe deflection stream of the data with 20 MHz bandwidth in time domain and drastically compresses the data stream to amplitude and phase information of limited frequencies at a rate of 1–10 kHz. LIAs measure the amplitude and phase during each pixel dwell time regardless of the previous or next measurements. Thus, in presence of high noise levels, the reliability of the measurements can be questionable. The DART technique requires

extra feedback time. This results in longer scan times, and often in unwanted tracking and post-processing errors [47]. Resonance tracking often fails on rough sample surfaces and generates imaging artifacts. Furthermore, the PID gain design and lock-in filter designs of DART measurements have ti be done in advance based on a well-known physical model, which is not precise and results in irreversible loss of valuable information.

In this section, the STIM data obtained through full information acquisition of AFM probe deflection stream are analyzed. The full details

n analysis flow is explained in Section 2.6 in details. In short, the approach is based on obtaining full information of cantilever motion in time-domain with high sampling rate and subsequent analysis based on information-theory analysis and physical model regression. Multivariate statistical analysis such as principal component analysis (PCA) performs orthogonal transformation and orders the modes based on variance. PCA compresses and denoises the highly redundant data obtained and yield valuable information on statistical relevance and spatial variability of the cantilever response. When the the fundamental behavior of cantilever motion is established, the data can be fitted to physical models, enabling the extraction of inherent material properties.

The STIM experiments were performed with resistive heating excitation on a ceria sample. Rather than sweeping the excitation frequency and measuring the averaged spectral amplitudes —such as lock-in measurements which fails to capture the transient phenomena and is time consuming— our method is based on fast and continues change of frequency while recording highly sampled signals in time domain. The tip-sample contact resonance is around 161 kHz (from point-wise lock-in measurements), and thus for the 4^{th} harmonic STIM the drive signal should have an excitation band with a quarter of this frequency. The excitation waveform was synthesized before the experiment, with a chirp frequency sweeping from 39 kHz to 43 kHz for each pixel dwell time of 9 msec through using an arbitrary waveform generator (AWG) (UHFAWG, Zurich instrument). The time-domain information is simultaneously captured with a sampling rate of 7MHz using a data acquisition system (DAQ) (UHF-DIG, Zurich Instruments) synchronized with AFM. Custom-made triggering

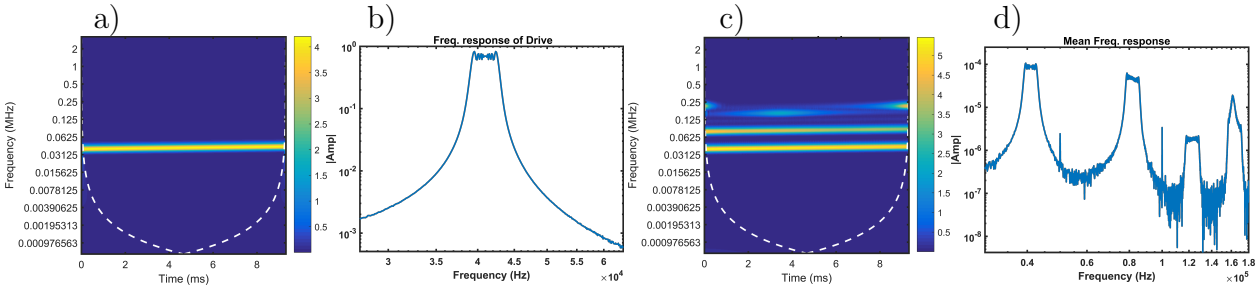

Figure 3.9: The excitation(a,b) and spatially averaged response (c,d) of 4$^{\text{th}}$ harmonic STIM obtained with continues wavelet (a,c) and Fourier (b,d) transforms. The chirp excitation waveform sweeps between 39–43 kHz while the response seems to have first, second, third and fourth harmonic responses.

circuit is designed to allow the AFM, AWG, and DAQ to work seamlessly in parallel without any dead-times. Simultaneous to the AFM scan, the AWG is exciting the heated probe while the DAQ captures the cantilever motion.

When the data is acquired, the full response is processed similar to that of conventional AFM through time-frequency analysis. Figure 3.9 shows the scalogram of the drive signal and the spatially averaged deflection responses over all pixels obtained via the continues wavelet transformation CWT and Fourier transforms. Note that small regions outside the dashed white line in CWT scalograms delineate regions where CWT edge effects are significant and thus the areas should be ignored. The drive signal has a 4 V amplitude and a frequency band between 39–43 kHz, as clearly depicted in Figures 3.9a,b). The mean deflection response (Figures 3.9c,d) exhibits responses at the first, second, third, and fourth harmonic with respect to the drive signal. The first harmonic response (around 40 kHz) may be due to a Vegard strain induced by electric potential of the probe and also due to the electrostatic interactions between the cantilever and sample. A disadvantage of heated probes is that the electrical drive necessary for resistive heating may interfere with the sample and cause the first and second harmonic responses. The second harmonic response (around 80 kHz) is prominently due to the thermomechanical STIM effect caused by thermal expansion of the sample. The third harmonic response is perhaps due to mixed nonlinear effect between the

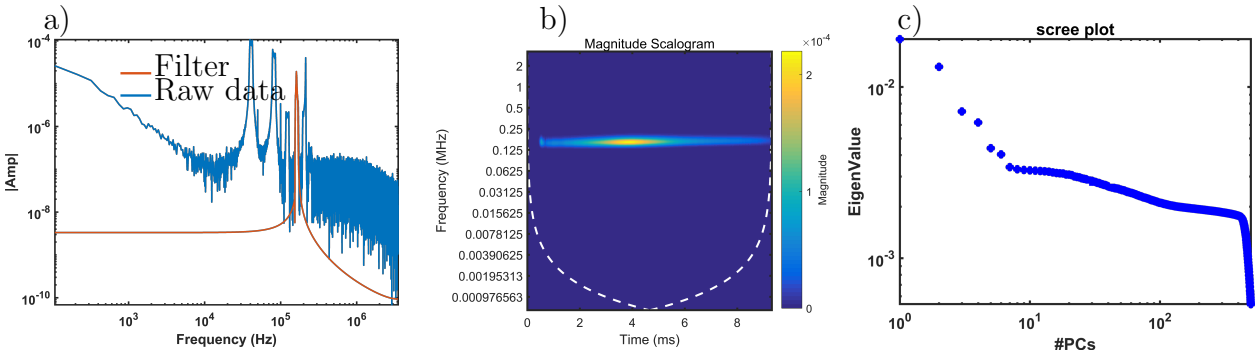

Figure 3.10: Optional Filtering of the raw STIM data and eigenvalues of PCA. (a) The raw data before filtering, and (b) the time-frequency representation of the data after filtering containing only 4^{th} harmonic STIM contribution. (c) The eigenvalues of each PCA mode is presented in the scree plot.

electrostatic, thermomechanical behavior and the Vegard strain. The peak around 160 kHz shows the resonance-enhanced 4^{th} harmonic STIM response which is known to be due to ionic motion induced by the temperature and stress oscillations at the second harmonic. The advantages of this method is evident, as it provides information on the complex dynamics of the tip-sample interaction and capture the full transient and steady-state behaviors which would be lost in lock-in measurements. As such, in one single scan the electrostatic, thermomechanical, and ionic behavior of the sample can be characterized.

The main focus of this chapter is to characterize the ionic motion of the sample. The data is filtered in time-frequency and keep the relevant information. Figures 3.10a,b show the application of a such a filter where only 4^{th} harmonic response is maintained. Note that this can be done during the experiment on-the-fly or afterward without any loss of data. The PCA is used to obtain the orthogonal modes with ordered statistical variance and keep the statistically significant modes for long-term storage. The raw data waveform of each AFM line is sliced into sequential smaller time segments, where each segment is selected to match the spatial pixel time. The eigenvalues presented in PCA scree plot (Figure 3.10c) illustrate that only the first seven PCA modes are relevant while the rest of PCA modes are redundant data.

Presented in Figure 3.11 is the PCA results. The top and bottom rows show the loading maps and their corresponding eigenvectors for the first four PCA components, respectively. The first PCA mode shows the average spectrum of the data and the higher modes take into account the spatial variables such as local shifts in resonance frequency, quality factor, local concentration and the phase lag. Although PCA can reduce the dimensionality of the data, due to its unsupervised nature of analysis, drawing any physical conclusion is challenging.

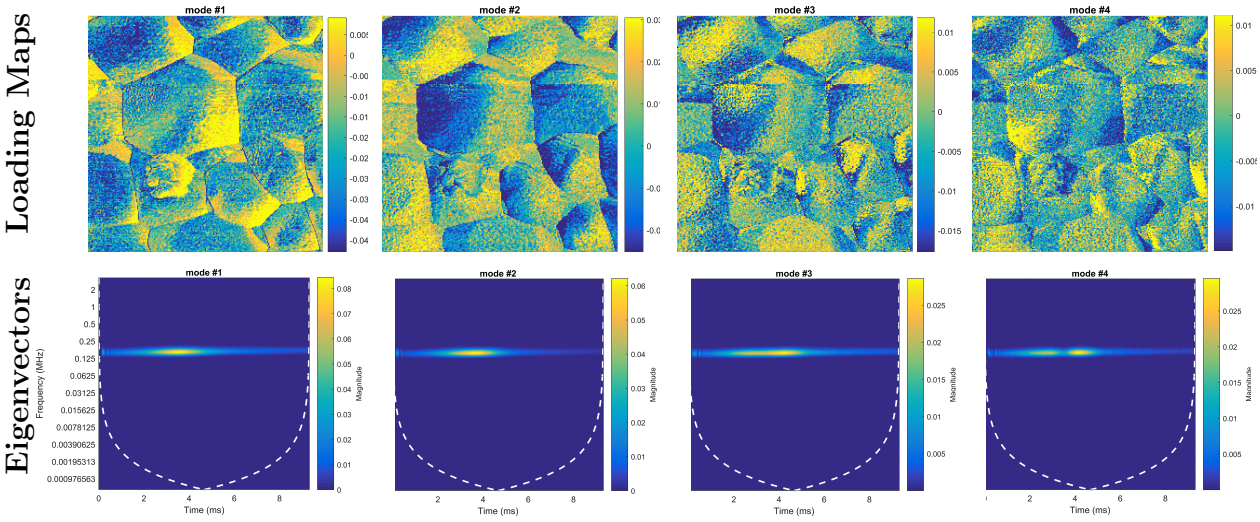

Figure 3.11: PCA analysis of 4^{th} harmonic STIM. The top and bottom rows show the first four loading maps and eigenvectors, respectively. The eigenvectors are obtained via a continuous wavelet transform after the PCA analysis.

The PCA analysis allow for reconstruction of the data based on selected modes. The data matrix is reconstructed based on the first seven PCA modes. The reconstructed deflection data for each pixel then is used to fit to a simple harmonic oscillator (SHO) model, which mimics the resonance behavior of the probe and reveals valuable information about material properties under the probe. The regression process allows for determination of intrinsic amplitude, quality factor and the resonance frequency of each pixel. This further reduce the dimensionality of the data to a low order model. Initially the raw data matrix contained 256^2 rows for all pixels and 2^{16} columns corresponding to time snapshots for each pixel. The PCA reduces the data matrix size to $256^2 \times 7$. However, the information are not physically

interpretable. The SHO model further reduces this to a data matrix of $256^2 \times 3$. Figure 3.12 shows the results of a such a regression analysis. The amplitude mapping in 3.12b shows a higher response on grain boundaries revealing higher ionic activity of space charge region. Interestingly, the of map resonance frequency shows variations within grains, without any cross-talks with the topography or amplitude maps.

The overall behavior of STIM responses of ceria obtained with full information acquisition is very similar to those obtained with lock-ins. Due to limited resources, these results were obtained with sampling rate of 7 MHz. Increasing the sampling rate to over 40MHz would allow us to achieve much higher signal-to-noise ratio. Beside PCA and SHO models, more sophisticated methods such as multi-resolution dynamic mode decomposition [134] can be employed to robustly separate complex systems such as tip-sample interaction with multiple eigen-modes of vibration into a hierarchy of multi-resolution time-scale components.

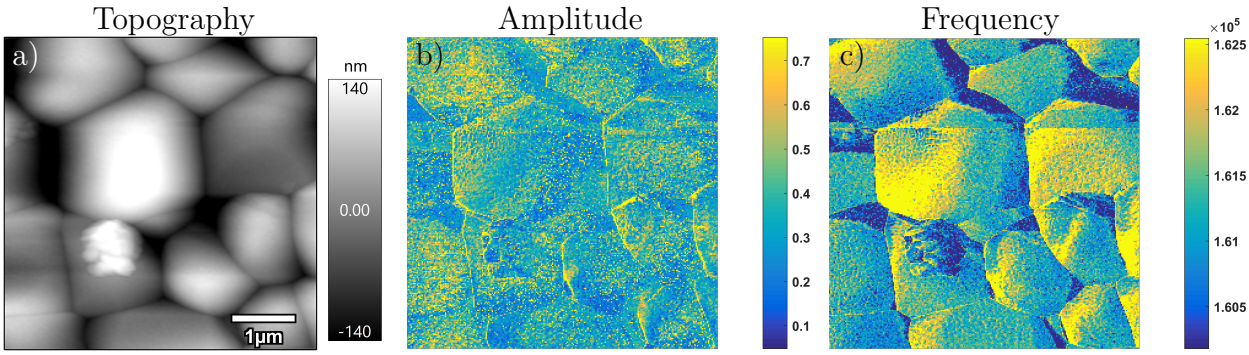

Figure 3.12: STIM ionic response obtained from full information acquisition of cantilever deflection. (a) Topography, (b) amplitude, and (c) resonance frequency maps obtained through PCA dimensional reduction and simple harmonic oscillator model fitting.

3.5 Conclusion

Probing local ionic concentration and obtaining information about diffusivity with nanometer resolution is challenging using conventional electrochemical techniques. Scanning thermo-ionic microscopy (STIM) overcomes this difficulty by measuring Vegard strain arising from

local ionic oscillation. Spatial resolution as small as 10 nm and sensitivity as high as picometer can be realized using a dynamic scanning probe, and the ionic response, measured in terms of probe deflection, correlates with local ionic concentration and diffusivity. Thus its is a powerful tool to probe local electrochemistry at the nanoscale, and can be used to study a wide range of electrochemical materials and systems wherein imaging local ionic distributions can further our understanding of materials and better tailor them for particular applications. Furthermore, thermal expansion and mechanical stiffness of the sample can also be obtained, yielding additional insight into the local electrochemical processes, for example the formation of solid electrolyte interface (SEI) in lithium ion batteries.However, the data analysis and interpretation of STIM are not straightforward, and often requires assistance of modeling and simulation to translate the measured probe deflection into ionic concentration and diffusivity. In particular, spectroscopy type of dynamic studies are necessary to deconvolute local diffusivity and ionic concentration in future studies.

In this chapter, the capabilities of scanning thermo-ionic microscopy (STIM) for characterizing ionic and thermal properties of materials at nanoscale is demonstrated, based on detecting dynamic strain due to ionic motion induced by modulated temperature and stress gradients. The technique was demonstrated on active electrochemical materials including ceria and perovskite $CH_3NH_3PbI_3$ as well as a control sample of PTFE, implemented using both resistive heating and photo-thermal heating. The dynamics of ionic motion can be captured from point-wise spectroscopy studies, while the spatial inhomogeneity is shown via by STIM mapping. The measurements were obtained through higher harmonic DART and full information acquisition of deflection signal and data processing techniques. Since STIM utilizes thermal stress-induced oscillation as its driving force, the ionic responses can be isolated from the electromechanical, electrostatic, and capacitive effects, and they are immune to global current perturbation, making in-operando testing possible. In principle, STIM is a powerful tool for probing local electrochemical functionalities at the nanoscale.

Chapter 4

SCANNING THERMAL MICROSCOPY FOR QUANTITATIVE MEASUREMENTS OF THERMAL PROPERTIES

4.1 Introduction

Solid-state thermoelectric conversion is promising for recovering tremendous waste heat produced by human society and for enabling more effective thermal management. However, the high thermoelectric conversion efficiency, governed by the dimensionless figure of merit ZT, requires simultaneously high electrical conductivity and Seebeck coefficient, yet at the same time requires low thermal conductivity, which is rather difficult to obtain in a single-phase material [135–139] . One of the primary mechanisms for improving thermoelectric performance in a material is to reduce lattice thermal conductivity through scattering of phonons by structural heterogeneity such as defects, interfaces, and impurities. In the last two decades, the nanostructuring paradigm has been successfully applied to a wide range of thermoelectric materials, resulting in significant reduction in thermal conductivity and superior thermoelectric performance [140–146]. For example, nanocrystalline $(Bi,Sb)_2Te_3$ with maximum ZT values of 1.4–1.6 were reported [141,147–149], and the improvement was largely attributed to the low lattice thermal conductivity resulting from intensified phonon scattering by nanostructures and defects [150]. In addition, by combining all-scale hierarchical architectural microstructures, including atomic defects, endotaxial nanoprecipitates, and mesoscale grains [151] a wide range of heat carrying phonons can be strongly scattered [143], resulting in high ZTs in PbTe [151]. Similar reduction in thermal conductivity has also been reported in many nanocomposites, including systems consisting of half-Heusler/full-Heusler and $In_xCe_yCo_4Sb_{12}$/InSb [152].

These advances in thermoelectric materials highlight the importance of nanostructuring

in enhancing thermoelectric properties, yet such improvements have been largely accomplished with no direct investigation of the local thermoelectric properties in nanostructured materials. Indeed, there still lacks an effective method that directly links the macroscopic thermoelectric performance to the local microstructures and properties. The microstructural heterogeneity can be mapped with atomic resolution in terms of chemical and phase compositions. However, the microstructural properties reveal limited information about local transport behavior. Traditionally, the thermoelectric properties are only measured at the macroscopic scale, averaged over various microstructural feature. It is a challenge to determine *which* material constituent contributes to *what* in the local thermal transport processes. Therefore, high spatial resolution is critically needed in the thermal analysis of nanostructured materials in general, and specifically nanostructured thermoelectrics.

In the last decade, time domain thermoreflectance (TDTR) emerged as a powerful tool for thermal transport property measurements [153, 154], though its spatial resolution is limited to hundreds of nanometers [155–158], making detailed mapping of thermal transport properties in nanostructured materials challenging. Various scanning thermal microscopy (SThM) techniques were developed based on temperature-sensitive phenomena, promising potentially higher spatial resolutions [159–169] , though they have rarely provided even a qualitative thermal mapping that correlates with the microstructures in a heterogeneous material. Furthermore,strong cross-talk between thermal imaging and surface topography is often observed. Such quantitative direct correlation is highly desirable for rational design and optimization of high performance thermoelectric materials.

In this chapter, quantitative mappings of local thermal conductivity with nanometer resolution and one-to-one correspondence to the microstructure is obtained, using filled skutterudite as a model system. The principle of SThM method for obtaining qualitative thermal properties along with implementation details are explained. SThM experiments are performed on calibration samples and the process is simulated with a finite element package to obtain quantitative relationship between the experimental parameters and local thermal conductivity of the samples. It is shown that the electrical resistance of the probe, under

the careful test conditions is correlated with the thermal conductivity of the sample under the probe tip for a wide range of thermal conductivities. The calibrated probe then is used to map local thermal properties of a thermoelectric sample, revealing quantitative thermal conductivity properties with nanometer resolution for the first time. The technique provides a powerful tool to correlate local thermal conductivities, microstructures, and macroscopic properties for nanostructured materials in general, and nanostructured thermoelectrics in particular.

4.2 Principle of the Method

4.2.1 Scanning Thermal Microscopy

The microstructural analyses such as scanning electron microscopy or energy-dispersive X-ray spectroscopy (EDS) are powerful in mapping local chemical composition and phase structure of a material. However, they do not reveal information about the local thermoelectric properties. Traditionally, such properties are measured at the macroscopic scale, and their local variations, if any, can only be deduced indirectly from the macroscopic measurement or from computational analyses. If one can correlate local thermal properties directly with the microstructural features, then the effect of structural heterogeneity on the macroscopic thermoelectric conversion can be better understood and optimized.

The local thermal characterizations is performed via a scanning thermal probe (Figure 4.1a) [170–172]. It has a micro-fabricated solid-state resistive heater at the end of the cantilever [173–175], which forms one branch of the Wheatstone bridge circuit that allows precise measurement of its electrical resistance. The Wheatstone bridge is designed and built specifically to be able to measure the voltage differences parallel to AFM measurements. When the probe scan material phases with lower (Figure 4.1b) and higher (Figure 4.1c) thermal conductivities, it will have lower and higher temperature drops, respectively, resulting in different probe resistances that can be measured accurately from the imbalanced Wheatstone bridge voltage. This enables us to image local the local tip temperature. In-

deed, there is a linear relationship between the probe resistance and its temperature around the SThM operation temperature (Figure 4.1d). The relationship is obtained by passively probing a hot-plate stage with well-defined temperatures:

$$R(T) = R_0(1 + \alpha(T - T_{amb})) \tag{4.1}$$

where R_0 is the resistance of the thermal probe at room-temperature reference T_{amb}=293.15 K, and α is the temperature coefficient of resistance (TCR) measured to be 0.8/K between 350 and 450 K (Figure 4.1d), the temperature range relevant or our subsequent experiments. As such, the thermal probe not only functions as a heater, but also as a local temperature sensor via the resistance measurement. This makes it possible to measure the local thermal properties of the sample quantitatively [159, 176].

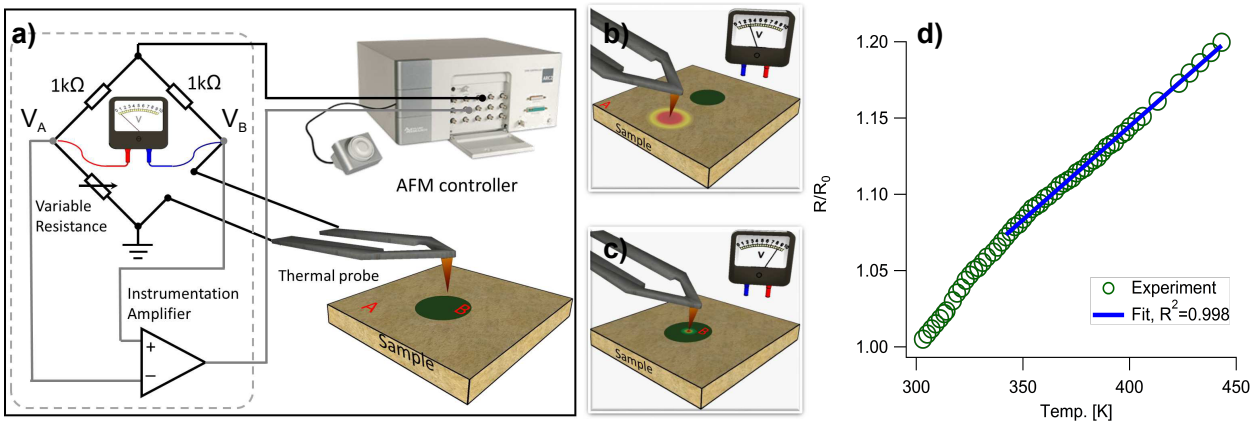

Figure 4.1: The schematics of SThM setup; (a) resistive heating thermal probe in a balanced Wheatstone bridge circuit (V_A-V_B=0) before touching the sample; the thermal probe scans phases with (b) lower and (c) higher thermal conductivities, resulting in different probe temperatures that can be measured via imbalanced Wheatstone bridge for imaging; (d) linear correlation between temperature and resistance of the thermal probe calibrated by a hot plate with known temperatures.

In order to precisely measure the change in electrical resistance induced by heat transfer to areas with different thermal conductivities, a custom-designed Wheatstone bridge was used. The Wheatstone bridge is balanced by adjusting the variable resistor before contacting

the sample. The bridge voltage is amplified with a 10× gain using a differential amplifier for enhanced sensitivity. Upon contacting the sample, heat transfers from the probe to the sample, resulting in a temperature drop, and thus a corresponding resistance drop, as measured by voltage drop between nodes A and B of the Wheatstone bridge. A lower thermal conductivity results in less heat transferred and in turn a lower resistance drop, as indicated by a smaller bridge voltage difference (Figure 4.1b). Conversely, a higher bridge voltage difference indicates a larger thermal conductivity (Figure 4.1c), making it possible to image local thermal conductivity variation based on the bridge voltage.

4.2.2 Numerical Modeling Framework for Quantitative SThM

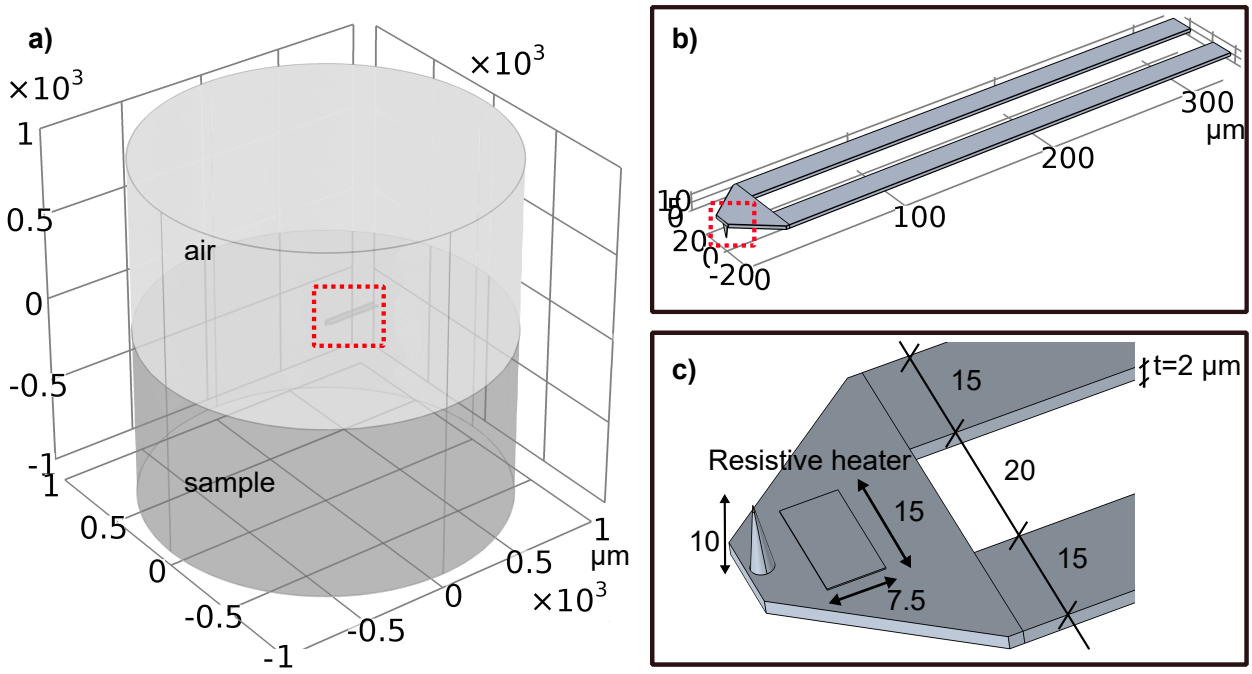

Figure 4.2: (Finite element model of SThM; (a) sample, probe and the surround air; (b) zoom-in on the probe; and (c) further zoom-in on the probe apex and heater region; all dimensions shown are in micrometer and the probe tip radius is 20 nm. The dashed red boxes show the zoom-in area.

In order to analyze the SThM data quantitatively, finite element model (FEM) implemented in the COMSOL Multiphysics package was developed to study heat transfer among

Table 4.1: Material properties used in FE simulations

Material	κ (W/(m.K))	C_p (J/(kg.K))	ρ kg/m^3
Cantilever	130	700	2329
Sample	3.2–15	300	7000
Air	0.025645	1010.19	1.2

the thermal probe, the sample, and surrounding air(Figure 4.2). Two dominant physical processes were considered, one is Joule heating in the resistive heater of thermal probe, and the other is heat conduction in the thermal probe, sample, and surrounding air. The quasi-steady problem was solved using a stationary solver based on the conduction equation

$$\rho C_p \boldsymbol{u} \cdot \nabla T - \nabla \cdot (\kappa \nabla T) = Q, \tag{4.2}$$

where ρ, C_p, and κ are the density, heat capacitance and thermal conductivity of each domain listed in Table 4.1, respectively, and Q is the heat source, set to be zero in all domains except in the resistive heater part of the thermal probe (Figure 4.2c) under an input voltage V_0,

$$Q = \frac{V_0^2}{R(T)}. \tag{4.3}$$

It is important to recognize that the temperature of the thermal probe and its resistance are intimately coupled, resulting in a nonlinear governing equation to solve. In the simulations, the initial value of temperature for all domains as well as the external boundaries of air-box and the sample (far from the thermal probe) are set to have ambient temperature $T = T_{amb}$.

Contact Thermal Resistance

One important aspect of heat transfer in SThM is the thermal contact resistance between tip and sample. The contact resistance depends on the probe and sample geometry, material properties, the nature of the contact and the contact area, and the contact force [167, 177]. Generally, the contact resistance is determined by performing point-wise SThM measurements on materials with known conductivity in advance,assuming the contact resistance is

constant for small variations of sample thermal conductivity or changes in surface roughness [178, 179]. Throughout all the measurements, the same SThM probe is used and the contact force is kept constant. Furthermore, with the intermediate range of sample thermal conductivity (2–13 W/(m.K).) the thermal contact resistance can be treated as a constant [168].

The thermal contact resistance G_c is implemented in the model by defining heat fluxes at the upside and downside boundaries according to the relations [180]:

$$-\boldsymbol{n_d}\cdot(-\kappa_d\nabla T_d)=\frac{T_u-T_d}{G_cA_c}\quad\text{and}\quad-\boldsymbol{n_u}\cdot(-\kappa_u\nabla T_u)=\frac{T_d-T_u}{G_cA_c},\tag{4.4}$$

where $\boldsymbol{n}$ refers to interfacial normal and the parameters at upside and downside are denoted by subscript. Across interfaces between different domains, temperature and heat flux density are assumed continuous ($G_c = 0$), except on the tip-sample contact A_c wherein a thermal contact resistance of G_c is defined.

The effect of the thermal contact resistance is examined by comparing the temperature and heat flux distributions along the tip-sample interface. Without considering the losses, the temperature should be continuous at the interface, while by defining the contact resistance, the temperature and heat flux drops significantly at the tip-sample junction (Figure 4.3). To identify the impact of the temperature drop on the probe heater resistance, the resistive heater temperature and its electrical resistance are compared as a function of the sample thermal conductivity, with and without considering the contact resistance. It is observed that although the tip temperature drops more than 20 K, the temperature and the electrical resistance of the resistive heater are not significantly affected (Figures 4.3&4.4). The change in the electric resistance after considering the thermal resistance for a sample thermal conductivity of 12 W/(m.K) is less than 0.1%.

The presence of the contact resistance results in significant temperature drop at the tip-sample junction but rather small temperature increases in resistive heater that is more relevant for the measurement (Figure 4.3). More importantly, the temperature of resistive heater is sensitive to the change in thermal conductivity of the sample, but much less sensitive

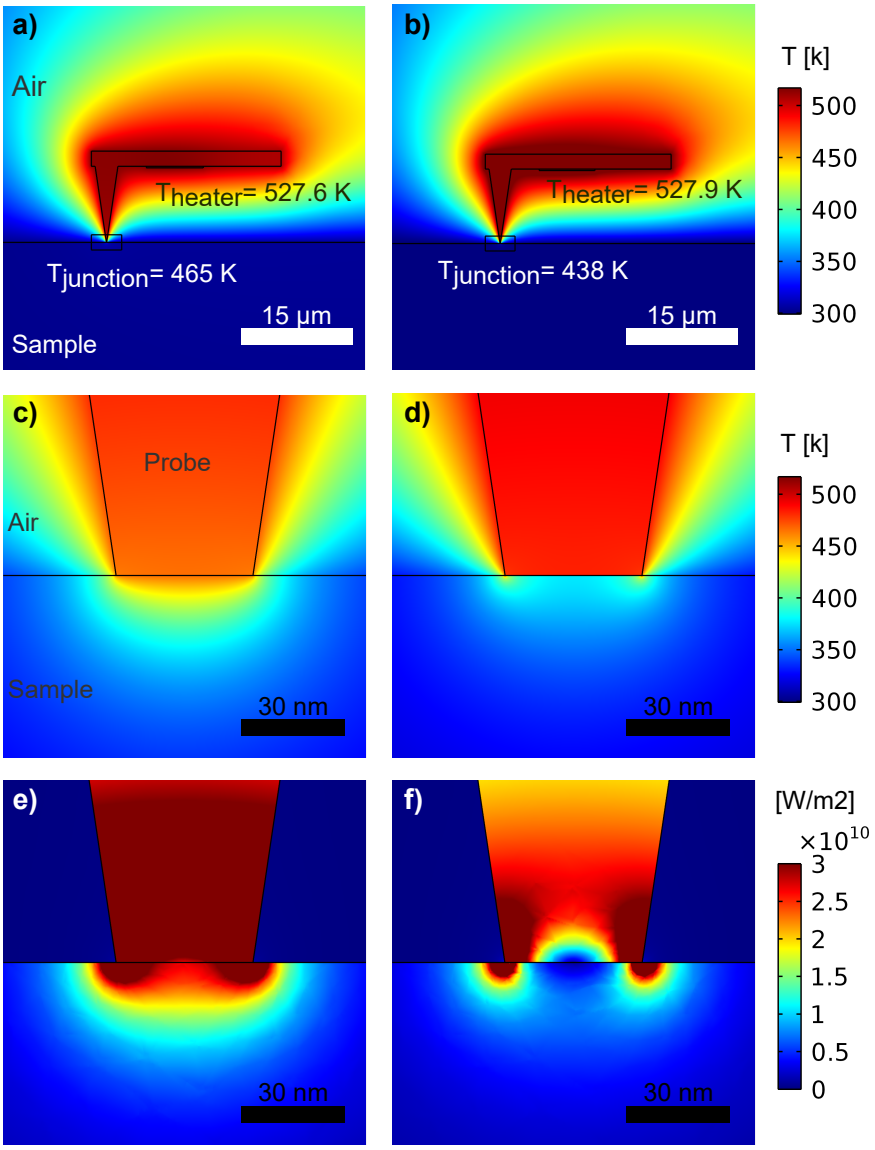

Figure 4.3: (Numerical simulation of SThM; the cross section temperature distributions along the probe (a,b) and near the probe-sample junction (c,d), and conductive heat flux distribution (e,f) near the probe-sample junction with. Thermal contact resistance was ignored on the left side (a,c,e) but considered in the right wide (b,d,f). In the simulation, the thermal conductivity of the sample is taken to be 5 W/(m.K), and the contact resistance is taken to be 1.0×10^8 K/W.

to the contact resistance variations (Figure 4.4), as the total heat loss due to the contact resistance is less than 1 μW while the total heat conductance through tip-sample junction is

in order of 100 μW. It is observed that with defining a contact resistance of 1.0×10^8 K/W, the maximum reduction in heater temperature and resistance is only 0.11% and 0.03%, while the change in thermal conductivity from 2 W/(m.K) to 12 W/(m.K) results in a reduction of heater temperature and resistance around 1.15% and 0.36%, which are much more substantial. Furthermore, it is observed that the change in heater temperature and resistance is insignificant when the contact resistance varies by four orders of magnitude. Therefore, a thermal contact resistance of $G_c = 1.0 \times 10^8$ K/W is defined in all simulations for the tip-contact with radius of 20 nm , which was measured using similar type of SThM probe in a previous study [181].

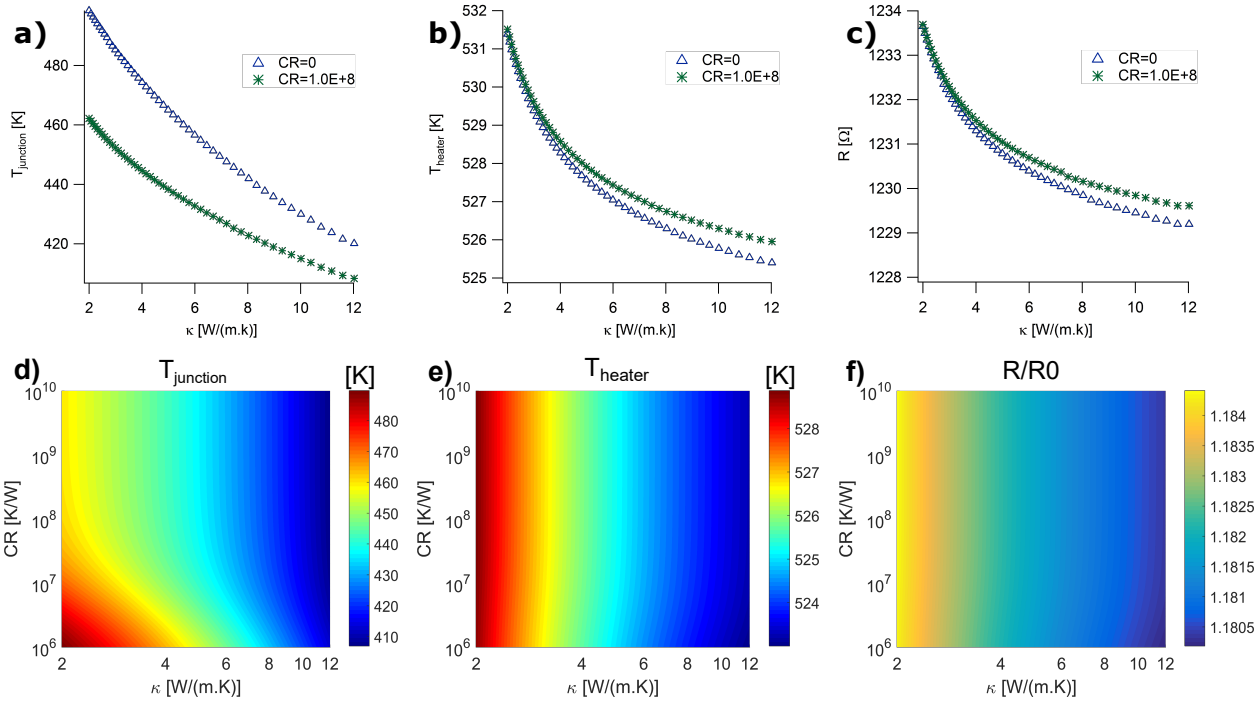

Figure 4.4: Sensitivity of SThM measurements as a function of sample thermal conductivity and contact resistance CR as revealed by numerical simulations; (a,d) temperature at probe-sample junction; (b,e) average temperature of the heater; and (c,f) the electrical resistance corresponding to the heater temperature. The top row shows the variation with respect to thermal conductivity, while the bottom row shows the two-dimensional mapping with respect to thermal conductivity and contact resistance.

Effect of Convection and Radiation

Another issue in nanoscale heat transfer of SThM is the effect of convection and radiation, which can be ignored as shown by the following analysis. In the simulation, the natural convection in the air is considered and solved by using a Laminar Flow module in COMSOL by solving the full Navier-Stokes equations considering the pressure shift:

$$\rho(\boldsymbol{u}\cdot\nabla\boldsymbol{u}) = -\nabla p + \nabla\cdot(\mu(\nabla\boldsymbol{u} + (\nabla\boldsymbol{u}^T)) - \frac{2}{3}\mu(\nabla\cdot\boldsymbol{u})\boldsymbol{I}) + (\rho-\rho_0)g, \tag{4.5}$$

where $\boldsymbol{u}$ and p are the fluid velocity and pressure fields, rho is the temperature-dependent density of air, ρ_0 is the reference density of the air in room temperature, μ is the dynamic viscosity, $\boldsymbol{I}$ is the identity matrix, and g is the acceleration due to gravity. The density and dynamic viscosity are temperature and pressure dependent which couples the Laminar Flow and Heat Transfer modules. The boundaries between air and solids are defined as no-slip walls and the external boundaries are defined as open boundaries, *i.e.*, the normal stress on boundary is zero.

The surface-to-surface radiation is defined on the bottom part of the probe and the top surface of the sample by defining a radiation flux between surface i to j, as:

$$Q_{ij} = \sigma A_i \epsilon_i (T_i^4 - T_j^4), \tag{4.6}$$

where ϵ_i is the surface emissivity of surface i conservatively assumed to be 0.6 for all surface, A_i is the surface area, and the Stefan-Boltzmann constant $\sigma = 5.67\times10^{-8}$ [W.m^{-2}.K^{-4}]. The radiative and conductive heat fluxes on the upper surface of the sample are compared in Figure 4.5, where a conductive heat flux orders of magnitude higher than the radiative one was observed. The total radiative heat transfer on the sample surface was less than 5 μW while the conductive one was in order of 9 mW. Similar simulation without considering the effect of radiation resulted in probe temperature difference of less than 0.01 K, reassuring that the radiation can be completely ignored.

To investigate the effect of natural convection, the conductive and convective heat transfer mechanisms were compared for a sample of thermal conductivity of 5 W/(m.K). The fluid

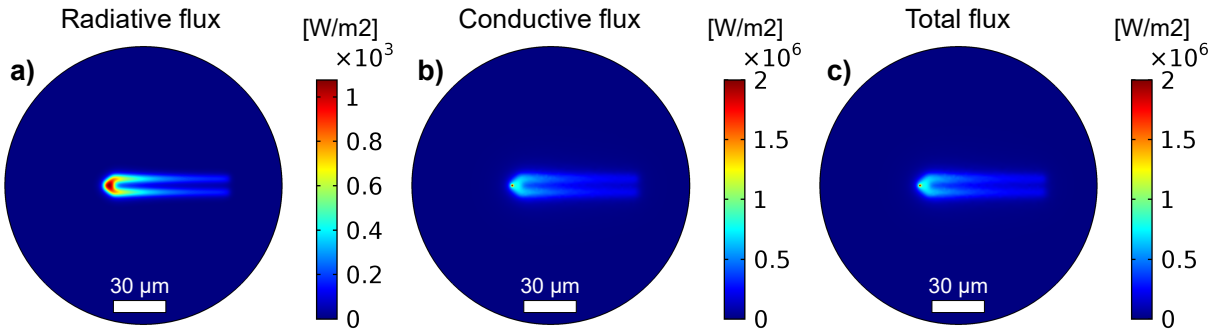

Figure 4.5: Simulations of SThM with radiative and conductive heat transfer. Comparison of the (a) radiative, (b) conductive, and (c) total heat flux magnitude mappings on the sample surface (zoom-in). The thermal conductivity of the sample was 5 W/(m.K).

velocity was observed to be less than 0.003 m/sec and the convective heat flux in the air is orders of magnitude smaller than the conductive one (Figure 4.6). The total heat transfer via natural convection was ∼40 μW while the total conductive heat transfer was in order of 9 mW. Furthermore, identical simulations without natural convection was performed, where the difference in the probe temperature was less than 0.75 K and the variation in the electrical resistance of the probe was less than 0.1%. Therefore, it is also safe to assume that the convection does not influence the SThM results.

4.3 Implementation

4.3.1 Sample

Yb-filled $CoSb_3$, with its maximum ZT up to 1.5, is one of the most promising thermoelectric materials for applications in the intermediate temperature range, since guest filling in the structural nanovoids acts to control the carrier concentration, while significantly suppress the propagation of heat-carrying phonons [182–184]. However, impurity phases such as $YbSb_2$, Yb_2O_3, and $CoSb_2$ are commonly observed due to the filling fraction limit of approximately 0.3 in $YbxCo_4Sb_{12}$, low formation energy of Yb oxide, and complexity in the Yb-Co-Sb phase diagram, and these impurity phases could exert significant influence on thermoelectric

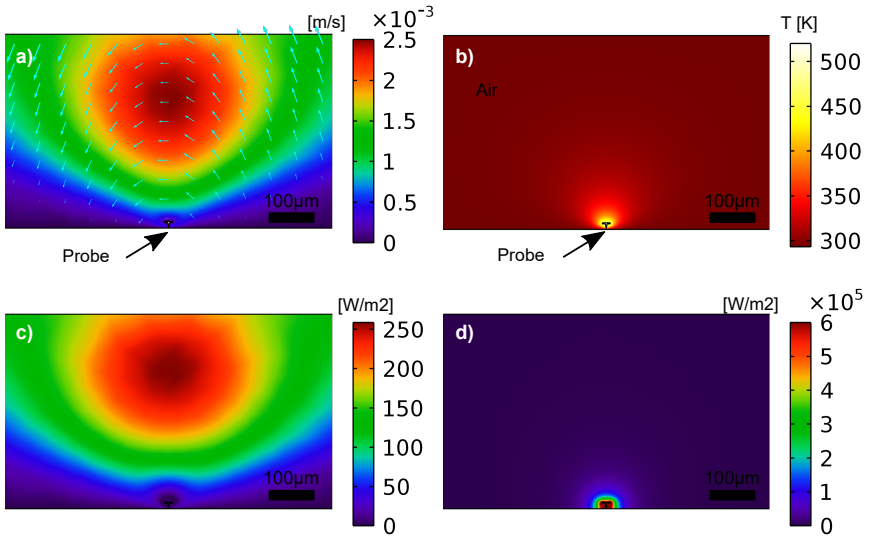

Figure 4.6: Simulation of SThM considering natural convection and heat conduction; (a) fluid velocity magnitude and field; (b) temperature distribution; (c) convective and (d) conductive heat flux distributions in the air-gap while the probe is contact with the sample ($\kappa = 5$ W/(m.K)).

properties [185]. The material systems provides an ideal model system to study its local thermal and electric conductivities.

The sample with a stoichiometry of $Yb_{0.7}Co_4Sb_{12}$ was prepared by a conventional induction melting-vacuum melting-quenching-annealing-sintering method. High purity Co powders (99.995%, Alfa Aesar), Sb shots (99.9999%, Alfa Aesar), and Yb chunks (99.995%, Alfa Aesar) were used as the starting materials. Co powders were first purified and melted into small shots with sizes of 1–5 mm by arc melting (SA-200, MRF Inc., USA), then loaded into a BN crucible with Sb shots for induction melting (at 2000 °C for 30 s under an Ar atmosphere, EQ-SP-25VIM, MTI Corporation, USA). The obtained ingot was subsequently crushed and loaded into a carbon-coated quartz tube with appropriate amounts of Yb and Sb in an argon-filled glove-box (Lab Star, Mbraun, Germany) and vacuum sealed (10^{-3} torr). Subsequently, raw materials were placed into a box furnace, heated to 1000 °C in 5 h, soaked for 24 h, and then rapidly quenched in ice water. The obtained ingot was ultrasonically cleaned and vacuum-sealed in a quartz tube, then annealed in a box furnace at 750 °C for

168 h. After annealing, the ingot was crushed, hand grounded into fine powders and sintered into a bulk material using the spark plasma sintering (SPS-211Lx, Dr. Sinter, Japan) at 680 °C and 50 MPa for 5 min.

4.3.2 Micro-Structure and Property Measurements

The phase composition was determined by the powder X-ray diffraction (XRD, Bruker D8 Focus X-ray diffraction, Germany) using the Cu K_α radiation ($\lambda = 1.5406$ Å). The BSE images were obtained in a TM3000 electron microscope (Hitachi, Japan). The chemical composition and elemental mapping were determined by a field emission scanning electron microscope equipped with EDS (FESEM/EDS, FEI Sirion, Japan). The electrical conductivity and Seebeck coefficient were measured simultaneously via commercial equipment (ZEM-3, Ulvac Riko, Inc., Japan) under a low-pressure helium atmosphere. Thermal conductivity was calculated from the product of the measured thermal diffusivity, specific heat, and density. Thermal diffusivity was measured by a laser flash method (Netzsch LFA-457, Germany), and specific heat was measured by a differential scanning calorimetry method (DSC) using sapphire as the reference (Netzsch 404F1, Germany). The measurement temperature ranges from 300 K to 850 K.

4.3.3 Scanning thermal microscopy

The scanning thermal microscopy was performed with an Asylum Research MFP-3D atomic force microscope (AFM) using a thermal probe with a spring constant of 0.2-0.5 N/m (ThermaLever^{TM} AN2-300, Anasys Instruments) in contact mode with contact force around 110 nN and scan rate of 0.5 Hz per line. The thermal probe is similar to any silicon AFM probe in geometry with an integrated heater at the end. A small region (7.5 $\mu m \times 15$ μm) close to the cantilever tip with light phosphorus doping acts as a solid-state heater. The heater region connects through two heavily doped branches acting as the electrical leads. The electrical resistivity of the probe varies between 600 Ω and 2 kΩ for different probes and different drive voltages.

4.3.4 Conductive AFM

The variations of electrical conductivity of the sample were characterized using ORCA, a conductive AFM (cAFM) module developed by Asylum Research. All measurements and images were obtained using AFM contact mode with a metallic Pt/lr coated probe having a force constant of 2.8 N/m (PPP-EFM, Nanosensors). Two different modes were used: imaging mode to map the variation of electrical conductivity, and spectroscopic mode to measure the I-V characteristics at points of interest. In the imaging mode, 2 V DC bias was applied to the sample substrate and the necessary current for virtually keeping the tip ground was used to image the electrical conductivity. In the spectroscopic mode under stationary probe, a sweeping DC bias (-0.6 V to 0.6 V) was applied to the sample while measuring the current that kept the conductive tip ground.

4.4 Result and Analysis

4.4.1 Three-phase Microstructure

The prepared $Yb_{0.7}Co_4Sb_{12}$ sample resulted in a three-phase microstructure (Figure 4.7). A back-scattered electron (BSE) image of the sample clearly reveals three phases as marked (Figure 4.7a), with impurity phases (2 and 3) embedded in the matrix phase (1). It is anticipated that the excessively added Yb reacts with Sb to form the $YbSb_2$ phase, and the resultant Sb-deficiency leads to the formation of $CoSb_2$. Such scenarios are indeed confirmed by the elemental mappings of Yb, Co, Sb, and O (Figure 4.7(b–e)) as well as elemental ratios in each phases determined from the energy-dispersive X-ray spectroscopy (EDS) (Figure 4.7f and Figure 4.8), suggesting that the matrix phase (1) is filled skutterudite $Yb_{0.3}Co_4Sb_{12}$, while the impurity phases (2 and 3) are $CoSb_2$ and surface oxidized $YbSb_2$, respectively. This analysis of phase composition is also confirmed by X-ray diffraction shown in Figure 4.9.

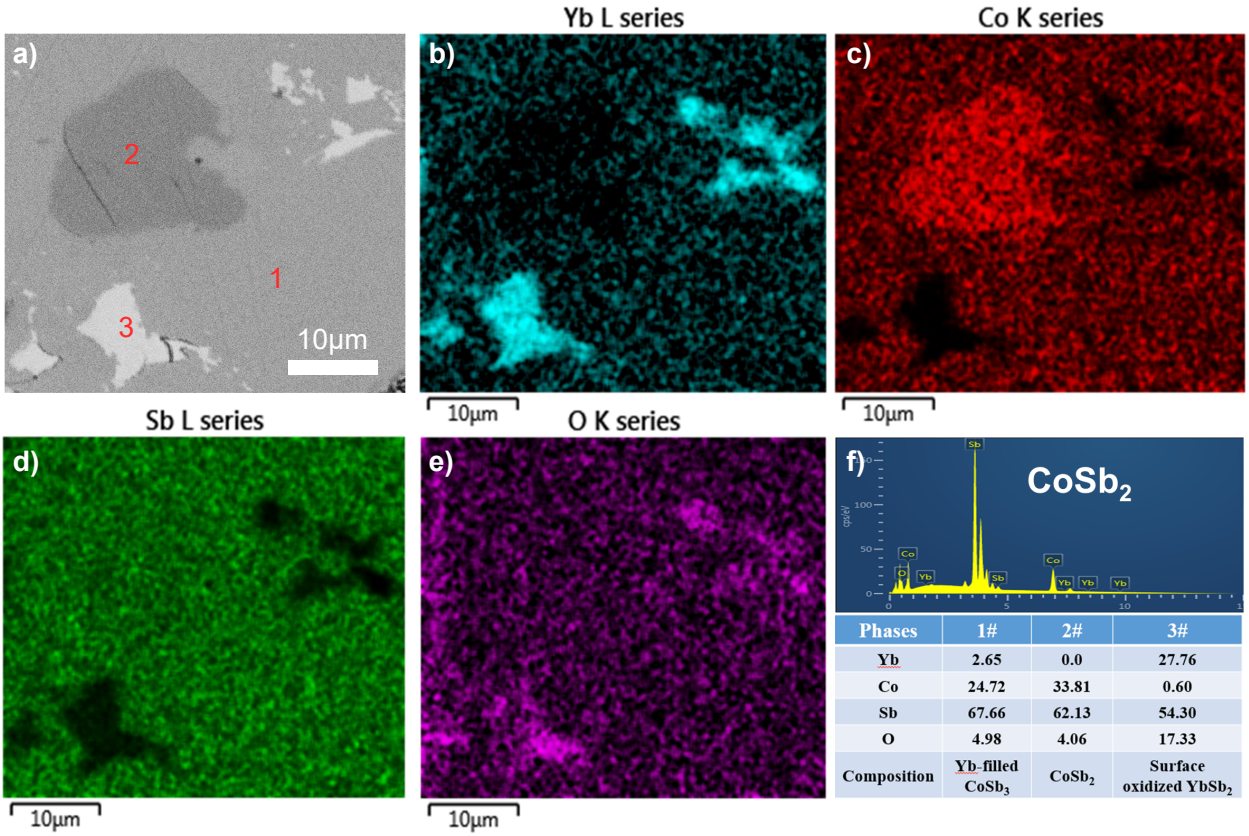

Phases	1#	2#	3#
Yb	2.65	0.0	27.76
Co	24.72	33.81	0.60
Sb	67.66	62.13	54.30
O	4.98	4.06	17.33
Composition	Yb-filled $CoSb_3$	$CoSb_2$	Surface oxidized $YbSb_2$

Figure 4.7: Composition analyses of three-phase microstructure in a $Yb_{0.7}Co_4Sb_{12}$; (a) a typical BSE image, wherein the three phases are labeled as 1, 2, and 3; (b–e) corresponding elemental mappings of Yb, Co, Sb, and O for the area shown in (a); (f) a typical EDS spectrum of phase 1, and elemental ratios of three different phases labeled in (a).

4.4.2 Qualitative SThM results

With a marker made near the area of the BSE image (Figure 4.10), the same area in the SThM studies is located. The topography mapping in Figure 4.11a obtained from the contact mode reveals relatively flat surface without any correlation with the microstructure shown in BSE image of Figure 4.7. However, simultaneous to the topography scan, the mapping of Wheatstone bridge voltage difference in Figure 4.11b clearly reveals three different contrasts that correlate well with the BSE microstructure, repeated here in Figure 4.11c for a direct comparison. Due to the drop in the probe temperature, and in turn the electrical resistance,

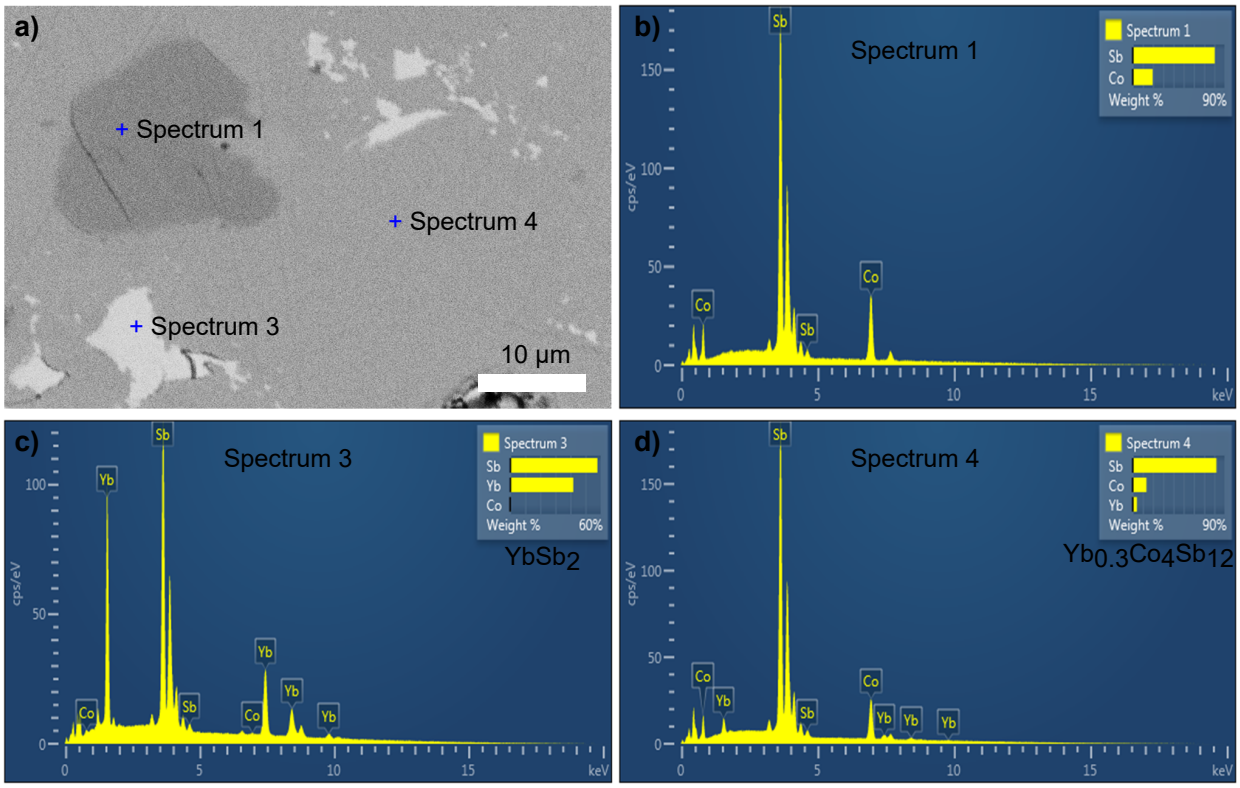

Figure 4.8: Energy dispersive X-ray spectrum EDS taken from different areas, using an FEI Sirion XL30 SEM with high resolution Oxford EDS; (a) back scattering image; (b) EDS of the $CoSb_2$ phase; (c) EDS of the $YbSb_2$ phase; and (d) EDS of the $Yb_{0.7}Co_4Sb_{12}$ skutterudite phase.

the Wheatstone bridge voltage drops to negative. The matrix phase (1) has the smallest voltage drop, while the impurity phase (2) has the largest. Such contrast is induced by the difference in thermal conductivity, not from the topography variation, as evident by the line scan comparison in Figure 4.11d. When a phase interface is crossed, sharp change in voltage difference is observed, while topography is relatively flat. On the other hand, within an individual phase, voltage difference is roughly constant, while topography variation is observed. The voltage difference mapped thus reflects the variation in thermal conductivity with no crosstalk to topography, wherein the matrix phase has the lowest thermal conductivity, while the impurity phase (2) has the highest. Thus, this is a direct characterization of local thermal conductivity that illustrates the role of impurity phases in thermal transport. Higher

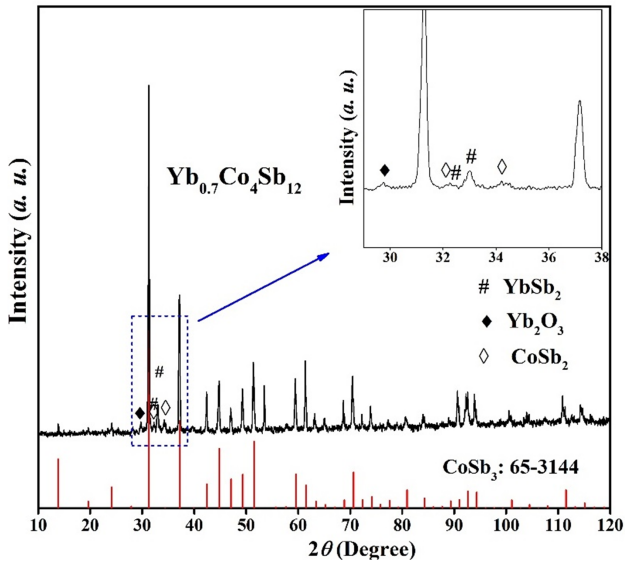

Figure 4.9: S2 Powder X-ray diffraction pattern of $Yb_{0.7}Co_4Sb_{12}$; the inset clearly shows the existence of $YbSb_2$, Yb_2O_3, and $CoSb_{0.2}$ impurity phases.

resolution scans of two boxes marked in Figure 4.11b are shown in Figure 4.11(e,f), demonstrating even higher sensitivity and spatial resolution. It is worth noting that although $YbSb_2$ (phase (3)) is supposed to have the highest thermal conductivity, it appears that the significant surface oxidation reduces its thermal conductivity, resulting in intermediate voltage drops as mapped.

4.4.3 SThM Simulation Results

The thermal probe in air, far away from the sample was considered. Under an input voltage of 3.5 V, the temperature distribution is shown in Figures 4.12(a-b), indicating a substantial temperature rise in the thermal probe up to 683K. The resistance of the probe is expected to rise with the increased input voltage in a nonlinear manner, caused by higher temperature induced by the heating voltage. This is confirmed in Figure 4.12c, wherein good agreement between experimental measurement and FEM simulation is observed, giving us confidence that the simulation does capture the physical processes in SThM experiment accurately. Next, the thermal probe in contact with a sample with a thermal conductivity of

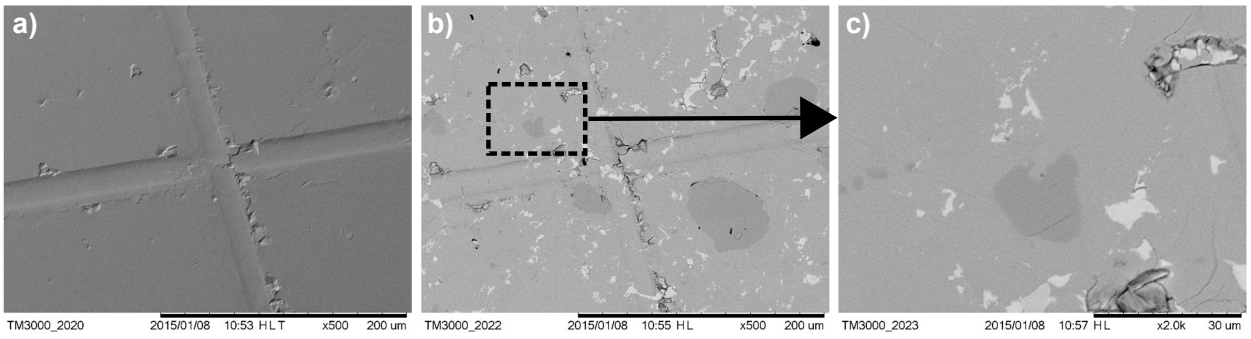

Figure 4.10: (a) SEM image of $Yb_{0.7}Co_4Sb_{12}$ sample with the artificial cross mark; (b) back scattered electron BSE image; and (c) zoom-in BSE image on the area of interest.

$\kappa = 5$ W/(m.K) was simulated. It is observed that the increased heat conduction through probe-sample junction results in a drop in the probe temperature, and in turn a drop in its resistance. Analysis on the overall heat flux and temperature distributions suggest that only a few percentage of the generated heat passes to the sample through the contact via heat conduction. Nevertheless, due to the small contact area of probe-sample junction, the heat flux density is substantial, and the resulting temperature drop in the thermal probe is significant, around 190 K. These are evident in the distributions of heat flux density and temperature in the probe-sample junction shown in Figures 4.12(d-e). Figures 4.12f-g show that the radius of the sample thermal volume affected by the probe is less than 100 nm, within which around 90% of temperature variation in the sample occur. This confirms the nanoscale resolution of our SThM technique.

4.4.4 Quantitative Mappings of Thermal Properties

In order to show feasibility of quantitative SThM, FEM simulations and SThM experiments were carried out on a 11 samples with nominal thermal conductivities ranging from 0.66 to 80.8 W/(m.K), spanning two orders of magnitude, as listed in Table 4.2. Under a constant 3.5 V DC bias to the thermal probe, the drop in the resistances when the probe contacts the samples was predicted by FEM simulations and measured by SThM experiments, as shown in Figure 4.13a. The point-wise experiments were repeated 5 times on each calibration

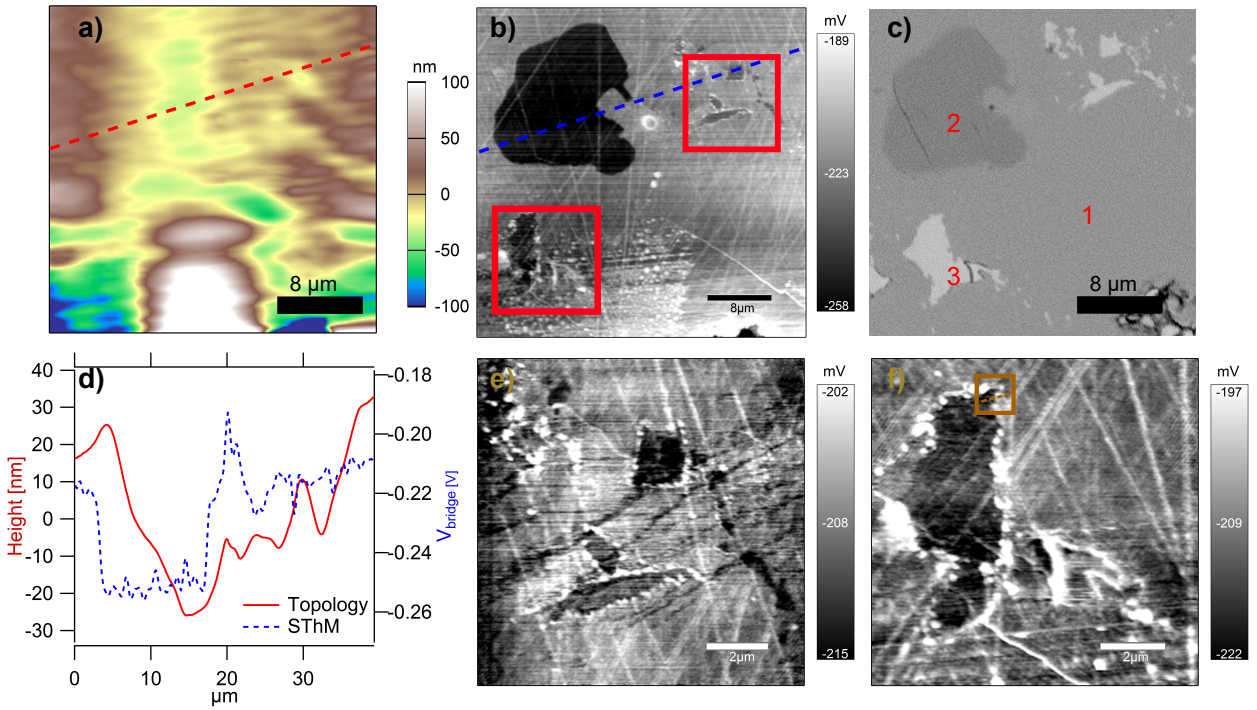

Figure 4.11: SThM mapping of a $Yb_{0.7}Co_4Sb_{12}$ sample; (a) topography; (b) distribution of Wheatstone bridge voltage with 10× amplification; (c) BSE image; (d) comparison of line scans in topography and voltage mappings; (e) and (f) higher resolution voltage mapping in smaller areas.

sample in different areas, and the mean and standard deviation were obtained with the SThM contact force kept constant throughout all the experiments. In the simulation, a constant contact resistance of 1.0×10^8 K/W is assumed, as explained earlier, and the results suggest that the thermal contact resistance is only significant for samples with higher thermal conductivity, consistent with what is observed in Figure 4.4. Good agreement between simulations and experiments observed in Figure 4.3a suggests that the thermal conductivity of the sample and the resistance drop can be quantitatively correlated. Indeed, for the three-phase microstructure mapped in Figure 4.10, the distribution of resistance change, shown here in Figure 4.13b, can be directly converted into a mapping of thermal conductivity shown in Figure 4.13c based on this correlation. The resulted thermal conductivities in the three phases are summarized in Table 4.4, and good agreements with nominal values reported in

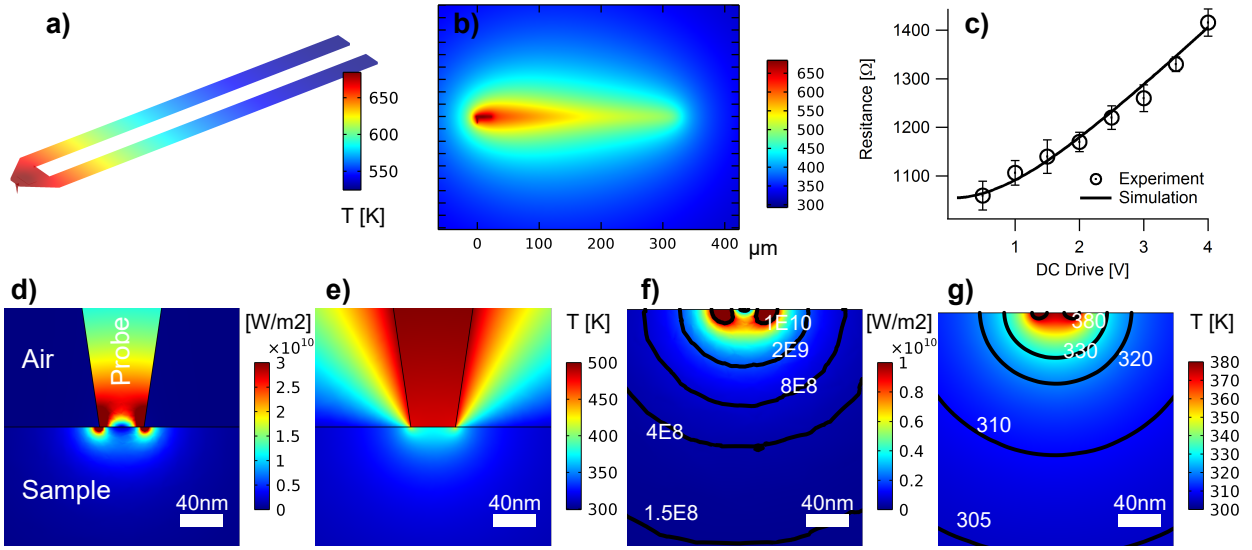

Figure 4.12: FEM simulation of the SThM experiment; (a-c) SThM simulation for a free probe in air: (a) 3D and (b) cross-sectional temperature distribution of thermal probe under 3.5 V heating voltage; (c) experimental probe resistance as a function of DC drive voltage in comparison with simulation; (d-g) SThM simulation the probe in contact with a homogeneous sample having $\kappa = 5$ W/(m.K), and the contact resistance is taken to be 1×10^8 K/W; cross-sectional distribution of (d) heat flux density and (e) temperature on the tip-sample junction; and overlaid contour on the distribution of (f) heat flux distribution and (g) temperature in the sample underneath the probe.

literature are observed [39, 49, 50], validating quantitative SThM mapping. Of particular interest is the variation of thermal response at an interface between two material phases. The interface marked by the dashed line in Figure 4.11f, passing from phase (3) to phase (1) is investigated. The variation of expected resistance change when the probe scans across the interface is simulated by FEM and compared with experiments, and again good agreement is observed, as shown in Figure 4.3d, with quantitative difference much less than 1%. FEM simulations were carried out under nominal thermal conductivity distributions with a sharp interface, as indicated by the blue line in Figure 4.3d, while the transition length of thermal response variation is in the order of 100 nm for both experiment and simulation.

Table 4.2: Thermal conductivity of calibration samples

Material	κ (W/(m.K))
$BiSbSe_3$	0.66
Te	1.31
$Yb_{0.25}Co_4Sb_{12}$	3.17
Bi	7.45
$CoSB_3$	10
FeNbSb	16.6
$YbSb_2$	16.69
Sb	22.3
Pb	34.3
Sn	71.3
Co	80.8

4.4.5 Mappings of Electrical Properties

The electrical conductivity of the sample in the same area is characterized using a conductive AFM (cAFM) (Figure 4.14), where good correlation between current mapping and phase distribution is observed. The current mapping in Figure 4.14b suggests that the electrical conductivity in the matrix phase (1) and secondary phase (2) is relatively high, while that of phase (3) is relatively low due to surface oxidation discussed earlier. Material phases (1,2) have comparable electrical conductivities of 2.3×10^5 S/m and 3×10^5 S/m, consistent with the slight contrast in Figure 4.14b. For phase (3), the oxidation of $YbSb_2$ introduces an insulating layer on the surface, resulting in very low electrical conductivity (Table 4.5). The I-V curves measured in each phase shown in Figure 4.14c also confirm this observation. Obviously, these impurity phases with higher thermal conductivity but lower electrical conductivity exert detrimental influence on the thermoelectric properties of skutterudites, and thus are

Table 4.3: Comparison of thermal conductivities measured from SThM experiment and reported in literature at 300 K

κ (W/(m.K))	$Yb_{0.3}Co_4Sb_{12}$ [184]	$CoSb_2$ [186]	$YbSb_2$	Yb_2O_3 [187]
Phase	(1)	(2)	(3)	(3)
SThM	4.63	11.71	*NA*	9.52
Reported	3.2	11.8	15.0	*NA*
Remarks	Polycrystal	Single-crystal	polycrystal	Surface oxidized

Table 4.4: SThM Numerical heat transfer properties at the contact of thermal probe with different phases of the sample.

κ	source	tip conduction/source (%)	tip heat flux (GW/m^2)	flux air to sample (kW/m^2)	tip temp. (K)	probe temp. (K)	$\Delta R(\Omega)$
4.5	9.968	0.9805	-4.861	-22.352	442.74	525.64	88.81
11	9.994	1.208	-6.105	-22.0.69	410.58	521.44	92.38
9.5	9.990	1.229	-6.004	-22.127	416.33	522.12	91.72

not desirable. Indeed, the thermoelectric properties measured at the macroscopic scale, as shown in Figure 4.15, confirmed this analysis, that its figure of merit ZT is not optimal due to these impurity phases. In order to exert significant scattering on phonons while negligible influence on electrons, it is critical to control precisely the stoichiometry and phase composition, as well as the size and morphology of impurity phases in filled skutterudites. In fact, this is important for nanostructured thermoelectrics in general.

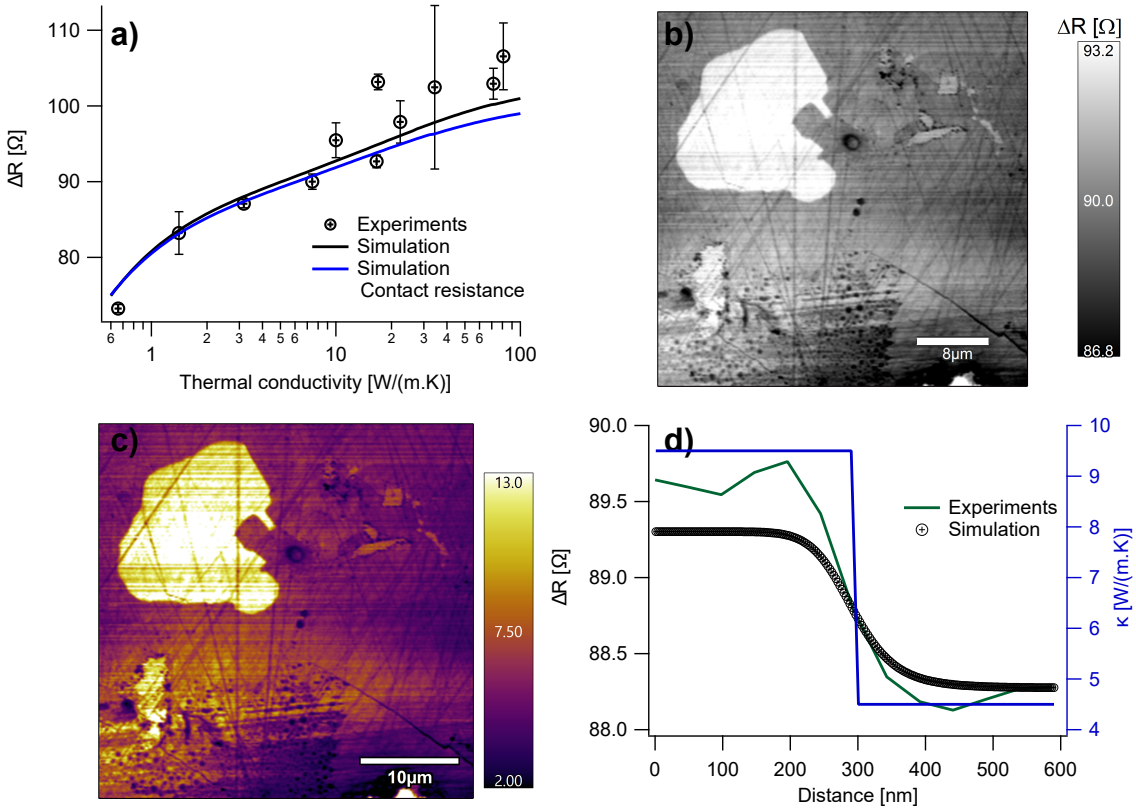

Figure 4.13: Quantitative mapping of thermal conductivities; (a) changes in the probe resistance induced by samples with different thermal conductivities; and mappings of (b) resistance change and (c) corresponding thermal conductivities in $Yb_{0.7}Co_4Sb_{12}$; (d) line scan of resistance change across an interface between phase (1) and phase (3).

4.5 Discussion and Conclusion

4.5.1 Discussions

It is remarkable that small contrasts in local thermal conductivity can be accurately mapped with nanoscale resolution via SThM. To understand the complex nanoscale heat transfer at the tip-sample junction better, finite element simulations were performed. The FEM simulation involves interaction of SThM tip with 3 representative material phases: matrix skutterudite $Yb_{0.3}Co_4Sb_{12}$ (1), impurity phase $CoSb_2$ (2), and surface oxidized phase Yb_2O_3 (3) are compared. The computed thermal transport parameters are summarized in Table 4.4. It

Table 4.5: Transport properties of four relevant phases of the $Yb_{0.7}Co_4Sb_{12}$ sample at 300 K

Phases	σ (S/m)	κ (W/(m.K))	α (μV/K)	*Remakrs*
$Yb_{0.3}Co_4Sb_{12}$ [184]	2.3×10^5	3.2	-138	Polycrystal
$CoSb_2$ [186]	3×10^5	11.8	26	Single-crystal
$YbSb_2$	7.9×10^6	15.0	15	Polycrystal
Yb_2O_3	2.4×10^2 [187]	*NA*	*NA*	no κ found

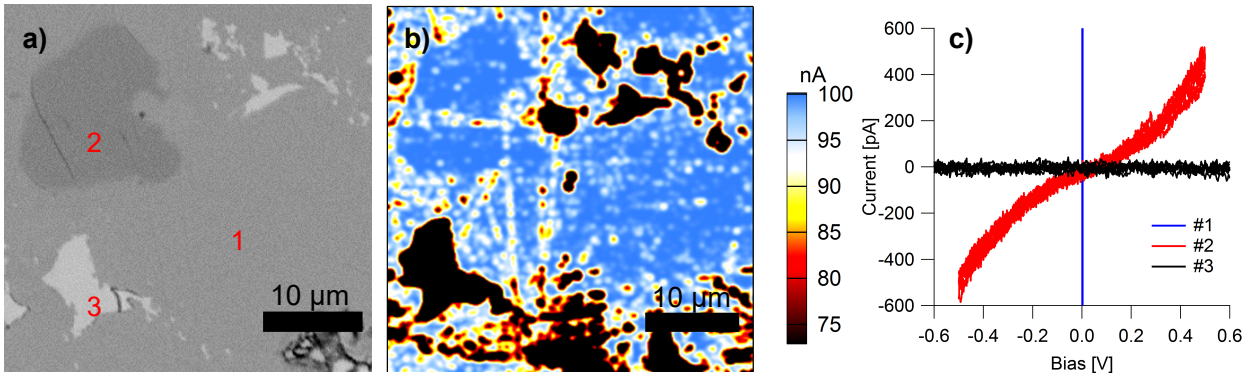

Figure 4.14: Mapping of local electric conductivity; (a) BSE image; (b) mapping of current; (c) IV curves measured in three phases using cAFM.

is interesting to note that although less than 2% of the total heat generated transfers through the tip-sample junction for each of the phase considered, the process, *i.e.* the change in heat transfer, is still dominated by the conductivity of the sample. Therefore, the heat flux at the tip-sample junction changes significantly for samples with different thermal conductivities, resulting in different temperature of the contact and thus different probe temperature and resistance that can be precisely measured using a Wheatstone bridge. This confirms the feasibility of the proposed technique and validates the experimental data. Further improvement can be achieved by carrying out SThM in vacuum, which would enhance sensitivity and resolution, though our study show that it is not absolutely necessary.

It is also important to examine the transient behavior of heat transfer during the SThM scanning obtained from FEM simulations (Figure 4.16) . It takes less than 1.2 milliseconds

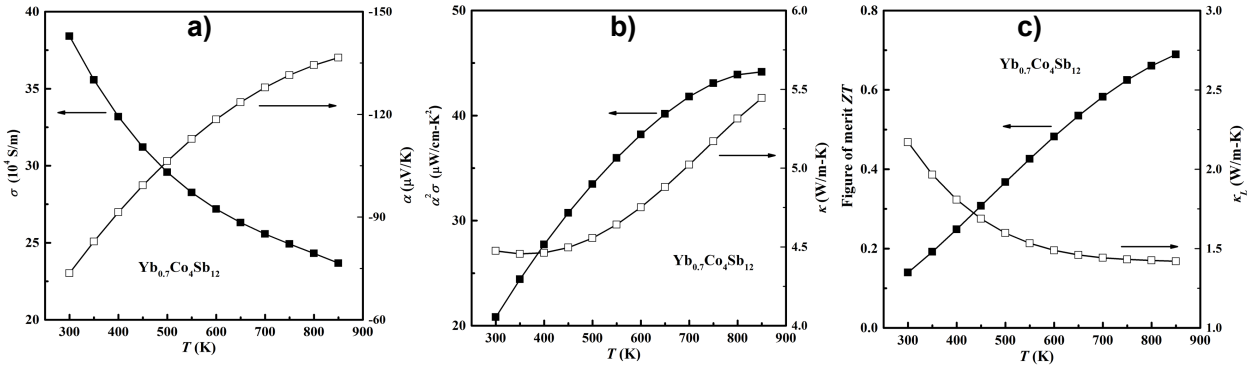

Figure 4.15: Thermoelectric properties of $Yb_{0.7}Co_4Sb_{12}$ sample; (a) electrical conductivity σ and Seebeck coefficient α; (b) power factor $\alpha^2\sigma$and thermal conductivity κ ; and (c) ZT and lattice thermal conductivity κ_L.

for the probe temperature to reach its steady-state value, and this is much less than the pixel time of SThM (3.1 mSec for 0.5 Hz line scan), ensuring a quasi-steady-state condition during the SThM scanning. This also imposes an upper limit on scanning rate at 1.3 Hz per line. Note that the assumption is conservatively based on reaching from the ambient to the operation temperature, while in during SThM scans, the probe temperature is around the baseline operational temperature with small variations, and therefore the transient time is much smaller.

Finally, it is noted that the spatial resolution of this technique can be further improved using a dynamic approach. Under a quasi-steady state condition, the affected thermal volume in the sample is substantial, with radius on the order of 100 nm. This has been confirmed by the temperature distribution in the sample underneath of the probe (Figure 4.2g), as well as the line scan of resistance change across an interface (Figure 4.3d). If a dynamic probing is adopted instead, wherein the heating voltage of the probe is frequency-modulated, and the corresponding harmonic response is probed, much higher spatial resolution on the order of 10 nm is expected. This will provide us a powerful tool to study the effect of structural heterogeneity such as defects, interfaces, and impurities in thermoelectric materials, which can be used to guide the design and optimization of thermoelectric materials with enhanced

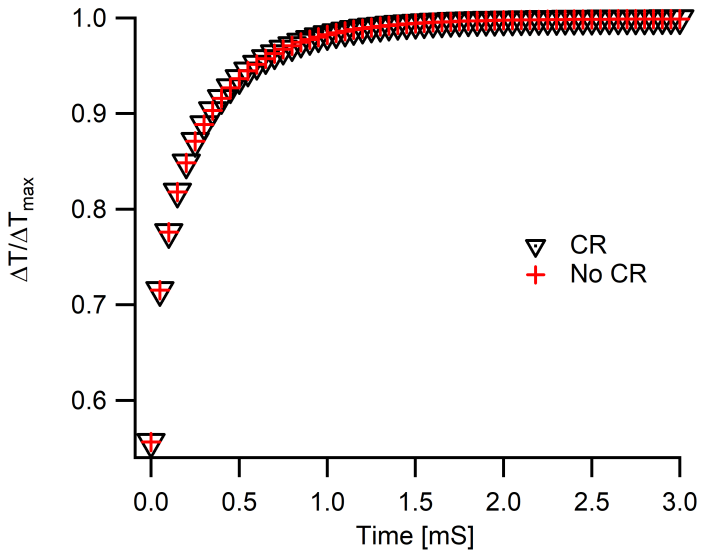

Figure 4.16: Time-dependent analysis of thermal probe in touch with a sample having κ = 5 W/m.K with and without considering the thermal contact resistance; The transient time for the thermal probe to reach steady-state condition is around 1.2mSec.

performance, especially when the thermoelectric coefficient can also be mapped in addition to thermal conductivity and electric current.

4.5.2 Conclusion

In this work, local thermal conductivities of a three-phase filled skutterudite were mapped quantitatively with good accuracy, nanometer resolution, and one-to-one correspondence with microstructure. Quantitative mapping was accomplished via a SThM using resistive heating thermal probe complemented by FEM simulations, enabling distinction of thermal conductivities spanning two orders of magnitude, yet resolving thermal variation across a phase interface with small thermal conductivity contrast. The technique developed here provides a powerful tool to correlate local thermal conductivities, microstructures, and macroscopic properties for nanostructured thermoelectric materials. SThM can be used to guide the design and optimization of thermoelectric materials with enhanced performance.

Chapter 5

IMAGING FERROELECTRIC DOMAINS VIA CHARGE GRADIENT MICROSCOPY

5.1 Introduction

Electromechanical coupling is a ubiquitous property of broad range of synthetic and biological material systems. For example, piezoelectric, ferroelectric, and electrostrictive materials, as well as muscles, hair cells, and voltage-gated ion channels exhibit electromechanical coupling [28, 100, 188–191]. In the last two decades, dynamic strain-based scanning probe microscopy such as piezoresponse force microscopy (PFM) has emerged as a powerful tool to investigate electromechanical coupling at the nanoscale. Because of experimental complications, these techniques are usually performed with a slow or moderate scan speeds, less than 250 μm/s. The measurements are averaged over each pixel with the pixel dwell time on the order of 100 μs, which is much longer that the nanosecond time scale of the ferroelectric dynamics. Therefore, the fast formation kinetics of domains and domain walls and the evolution of the screening charges cannot be captured by such quasi-static measurements. Furthermore, none of these techniques measure the polarization directly and the data interpretation is often challenging. For example, PFM images ferroelectric domains through measuring the piezoelectric strain. However, it is well known that multiple electromechanical mechanisms contribute to the piezoresponse signal measured by PFM [2, 40, 192–194].

In this Chapter, the recently developed charge gradient microscopy (CGM) is employed to study the ferroelectric domain structure of $LiNbO_3$ crystal. The effects of scan speed and temperature on CGM signals are investigated. Principal component analysis (PCA) reduces the dimensionality and enhance the signal-to-noise ratio of CGM signals. The analysis demonstrates that CGM signals are linearly proportional to the scan speed and inversely

proportional to the temperature. The study suggests that the current measured under CGM arises from the scraped and refilled surface charges within a domain, and from polarization change experienced by the scanning probe across a domain wall. Finally, CGM signals are used to provide a direct estimation of spontaneous polarization and surface charge density of $LiNbO_3$.

5.2 Principle and Methods

5.2.1 Charge Gradient Microscopy

Recently, charge gradient microscopy (CGM) was developed to study the ferroelectric domains and characterize their surface charges [195–197]. CGM operates by mechanically scraping the screening charges on the surface using a conductive scanning probe, and collecting the resultant current using a conductive atomic force microscopy (cAFM). Note that these scraped charges can be compensated and refilled by the conductive probe (Figure 5.1a). Since the probe is virtually grounded under cAFM, the refilled charges can be measured as a current signal, making imaging possible. Because of the fast-moving probe, the refilling process is rapid compared to other mechanisms, enabling the study of dynamic process of domains and domain walls. Unlike other SPM techniques, the measured current can be directly correlated to polarization.

5.2.2 AFM Measurements

PFM scans were carried out to map the ferroelectric domain structure of PPLN (Figure 5.1b). An AC voltage of 7 V with a single frequency of 135 kHz was used to excite the piezoresponse. The excitation frequency is far away from the contact resonant frequency of approximately 2 MHz, making the direct identification of the polarization orientation possible. The scan speed was 22 μm/s and the contact force was constant at approximately 500 nN.

The CGM signals were acquired using ORCA (Asylum Research, USA), a cAFM module with a gain of 5×10^8 V/A (Figure 5.1a). The CGM scan speed incrementally increases from

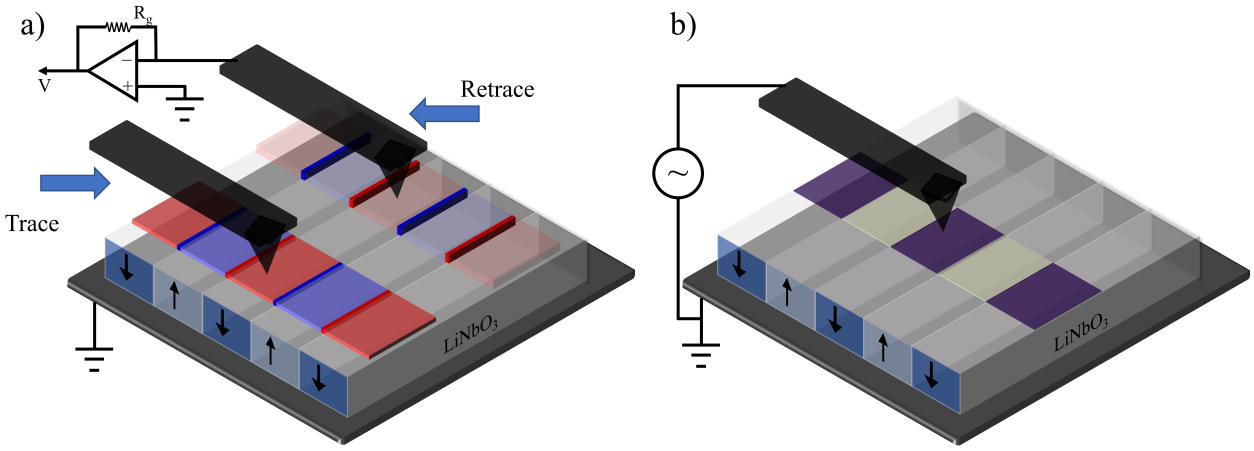

Figure 5.1: Schematics of (a) charge gradient microscopy with trace and retrace current mappings overlaid, and (b) PFM with phase map overlaid partially.

~75 μm/s to ~3 mm/s in a series of scans while the contact force was constant at around 3 μN. Note that the contact force in CGM is much higher than that of PFM to ensure that surface charges were scraped effectively. In addition, a heating stage (PolyHeater^{TM}, Asylum Research, USA) was used to study the effect of temperatures on CGM signals. In the experiment, the temperature of the sample was slowly raised to 83 °C and kept constant. Continuous CGM imaging was carried out while the temperature was ramped down with a rate of 4 °C/min controlled via a closed-loop feedback.

The experiments were carried out on MFP-3d and Cypher AFMs (Asylum Research) using a conductive diamond probe (CDT-NCHR-10, Nanosensors, Inc.) with a spring constant around 80 N/m.

5.2.3 Principal Component Analysis

A series of CGM current mappings were acquired under different conditions, including different scan speeds and temperatures, and the data were post-processed by PCAto enhance the signal-to-noise ratio. The details of analysis is provided in Section 2.5.3.

5.2.4 Sample Properties

Lithium niobate ($LiNbO_3$) is a uniaxial ferroelectric crystal with large spontaneous polarization ($P_s = 80 \pm 5\ \mu C/cm^2$) aligned along the crystallographic Z-axis [198, 199]. Because of its versatile ferroelectric properties, $LiNbO_3$ has been used in a wide ranges of applications, including electro-optics [200], nonlinear optics [201], ferroelectric data storage [202], and microelectromechanical devices [203]. Most of these applications involve ferroelectric domains with 180° domain walls created by applying an external electric field to produce antiparallel (180°) domains with $+P_s$ and $-P_s$ polarizations. The large spontaneous polarization of $LiNbO_3$ often results in screening charges from the surrounding environment, so that bound charges on the crystal surface can be compensated, and the electrostatic energy can be minimized [204]. A periodically poled $LiNbO_3$ (PPLN, Asylum Research, USA) sample is used in this study. The poled domains are approximately 10 μm in width and the sample is mounted on a metal puke and has dimensions of 3 $mm \times 3\ mm \times 0.5\ mm$.

5.3 Results and Discussions

PFM with a scan speed of f 22 $\mu m/s$ is performed to map the ferroelectric domain structure and identify the polarization direction of PPLN. The measurements were not resonance enhanced as the absolute phase of piezoresponse at the contact resonance is not well defined, and the resonance-enhanced imaging at higher frequencies can change the piezoresponse due to the dynamics of cantilever or instrumental lags [205–207]. Away from the resonance, the polarization direction can be deduced directly from the piezoresponse phase signal measured [2]. The amplitude of PFM response reveals the domain pattern of PPLN sample in Figure 5.2a. While the oppositely oriented domains have similar responses, the domain walls exhibit low responses. This is evident from PFM phase mapping in Figure 5.2b as well, wherein 180° phase contrast is observed across domains. The variation of PFM phase and amplitude can be more clearly seen in Figure 5.2c. Given the positive d_{33} coefficient for PPLN, the phase should be around 180° and 0° for upward- and downward-polarized

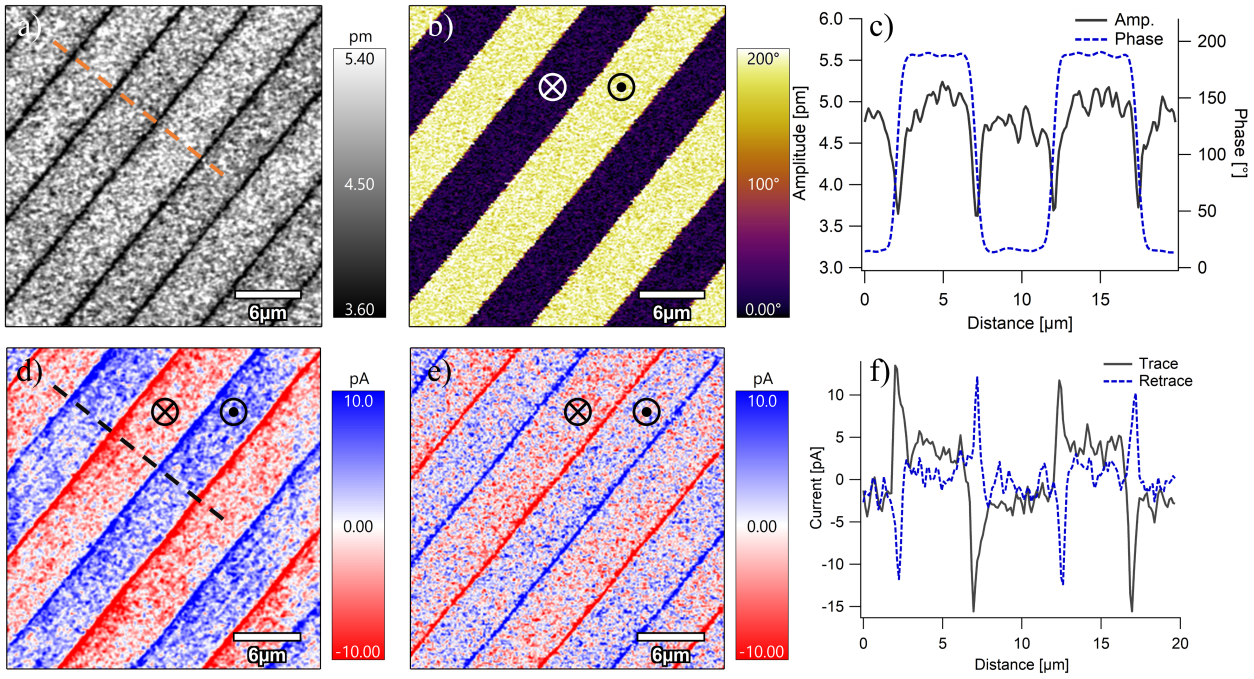

Figure 5.2: Domain pattern of PPLN mapped by (a-c) PFM and (d-f) CGM; PFM amplitude (a), phase (b), and line scans of amplitude and phase (c); and CGM current mapping during trace (d), retrace (e), and corresponding line scans (f). The PFM was acquired with probe speed of 22 μm/s while the CGM acquired with probe speed of 1.5 mm/s. The upward and downward domains are shown by $\odot$ and $\otimes$ signs, respectively.

domains (Figure 5.2b) [208].

While powerful for domain imaging, PFM does not yield quantitative information on the local polarization value. The CGM signals acquired in a separate scan but on the same area as PFM (Figures 5.2d,e) for both trace and retrace AFM passes. There are current spikes when passing over domain walls. The polarity of the current over the same domain wall is is alternating for trace and retrace passes The spikes can be seen more clearly from the line scans in Figure 5.2f. The current magnitude is reduced within domains, and the sign of the current acquired during trace and retrace are identical for the same domain. However, between the adjacent domains the sign is reversed. The difference between CGM signals at domain walls and within domains can be understood from two different imaging mechanisms.

The polarization within a domain is compensated by the screen charge on the surface, and the charges are mechanically scraped by the CGM probe and then refilled, resulting CGM current signals. For a downward polarization, the positive surface charges are scratched away and have to be refilled from the probe, resulting in a negative current (*i.e.* positive charges are flowing from the probe to the sample). In this process the current sign does not depend on the scan direction. For an upward polarization, positive current (flowing from the sample to probe) is resulted. This is indeed what is observeed in Figure 5.2d,e, confirming that the imaging mechanism within domains is scratching and refilling of surface charge by the virtually grounded CGM probe. When a domain wall is crossed, from a downward polarized domain to an upward polarized one, the net polarization difference is $+2P_s$. This positive polarization difference results in a positive current spike, which is reversed when going from the upward polarization to the downward one. This also explains why the current spikes reverse polarity between trace and retrace passes. These observations confirm that the imaging mechanism at domain walls is caused by the change of polarization experienced by the probe. Consequently, two different imaging mechanisms exist for CGM, which were observed by Hong *et al.* as well [195]. It should be noted that this CGM mechanism is foundamentaly different than the photo-induced current along the domain walls [209].

5.3.1 Effect of Scan Speed on CGM Signals

To further understand the imaging mechanism of CGM, the effect of scan speed v on CGM signals, ranging from $\sim$75 μm/s to $\sim$3 mm/s, is investigated. The raw CGM mappings acquired during the trace pass under a slow, intermediate, and fast scan speeds are presented in Figure 5.3a-c, showing enhanced CGM signals under higher scan speeds. However, having currents on the order of pA, the signals are noisy and it is difficult to draw a quantitative conclusion. Traditionally, the evolution of a set of AFM images were compared by their mean and standard deviation [195], which can be unreliable given the noisy CGM measurements. Principal component analysis is used to analyze the data. The PCA eigenvalues drop rapidly after the first one (Figure 5.3d) suggesting that the first mode has the highest

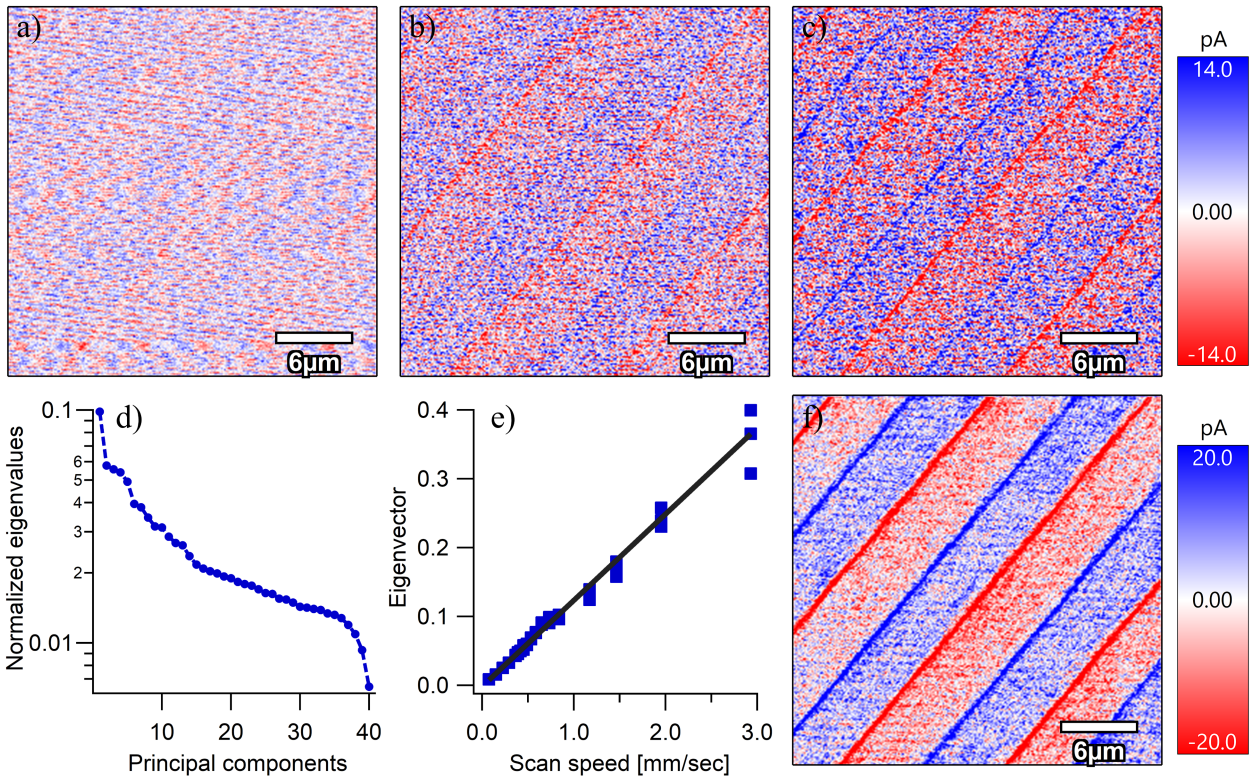

Figure 5.3: CGM under different scan speeds; (a-c) raw CGM current mappings acquired with scanning speed of 0.36 mm/s (a), 1.46 mm/s (b), and 2.93 mm/s (c); (d-f) PCA of scan speed-dependent images: scree plot of eigenvalues (d), the first PCA eigenvector (e), and its corresponding component image (f).

possible variance and contains the most information in this set of data. The first eigenvector $b_1(v_i)$ captures the average spectrum of data as a function of discrete set of scan speeds v_i (Figure 5.3e). The first PCA loading image shows the spatial distribution of CGM data (Figure 5.3f). The higher component images of PCA only contain noise, confirming that the first mode is indeed sufficient to represent the data. The noise reduction is evident in the first PCA loading image, while the corresponding eigenvector exhibits a linear correlation between scan speed and the average current signal. Such a linear relationship is consistent with the imaging mechanisms proposed. The current under a constant change in charge is inversely proportional to time, and directly proportional to the scan speed.

5.3.2 Effect of Temperature on CGM Signals

The origin of current signals are further investigated by performing temperature-dependent CGM. The CGM data set is acquired while the temperature is continuously decreasing from 83 °C to 30 °C. The raw CGM current images acquired at three distinct temperatures (Figure 5.4a-c) are showing a stronger signals for lower temperatures. To see this more clearly, this set of temperature-dependent CGM data was also analyzed by PCA and the eigenvalues are plotted in Figure 5.4d. It is observed that the second and higher modes of PCA have variances orders of magnitude less than that of the first mode. The eigenvector of the first mode exhibits a power-law decrease with increased temperatures (Figure 5.4e). The first PCA loading image (Figure 5.4f) clearly reveals the domain structure of PPLN with enhanced signal-to-noise ratio. This temperature-dependence can be understood from the imaging mechanism of the CGM. The increased temperature reduces spontaneous polarization and removes the screening charges, and therefore, reduces CGM signal. Indeed, Tong *et al.* discussed that the surface of PPLN is screened via short-range adsorption of ambient humidity molecules [197], and the rise in temperature results in evaporation of water and decrease in the humidity, which significantly suppress the CGM signal. Furthermore, when the relative ambient humidity is less than 30%, no CGM signal is observed in experiments.

5.3.3 Quantitative Analysis of Spontaneous Polarization and Surface Charge Density

The dependence of CGM current signal on scan speed and temperature are clearly revealed by PCA, consistent with the proposed imaging mechanisms based on scraping and refilling of charges within domains, and changes of polarizations at domain walls. With such an understanding on CGM current, the spontaneous polarization P_s as well as the surface screening charge density $|\sigma_d|$ are estimated based on the current measured in CGM.

The estimated displacement charge associated with the crossing over a domain wall $|Q_w|$ can be correlated with the absolute polarization difference $2P_s$ as: $|Q_w| = 2P_s A_{tip}$, where A_{tip} is the circular contact area of tip-sample junction with tip radius of 45 nm. Similarly,

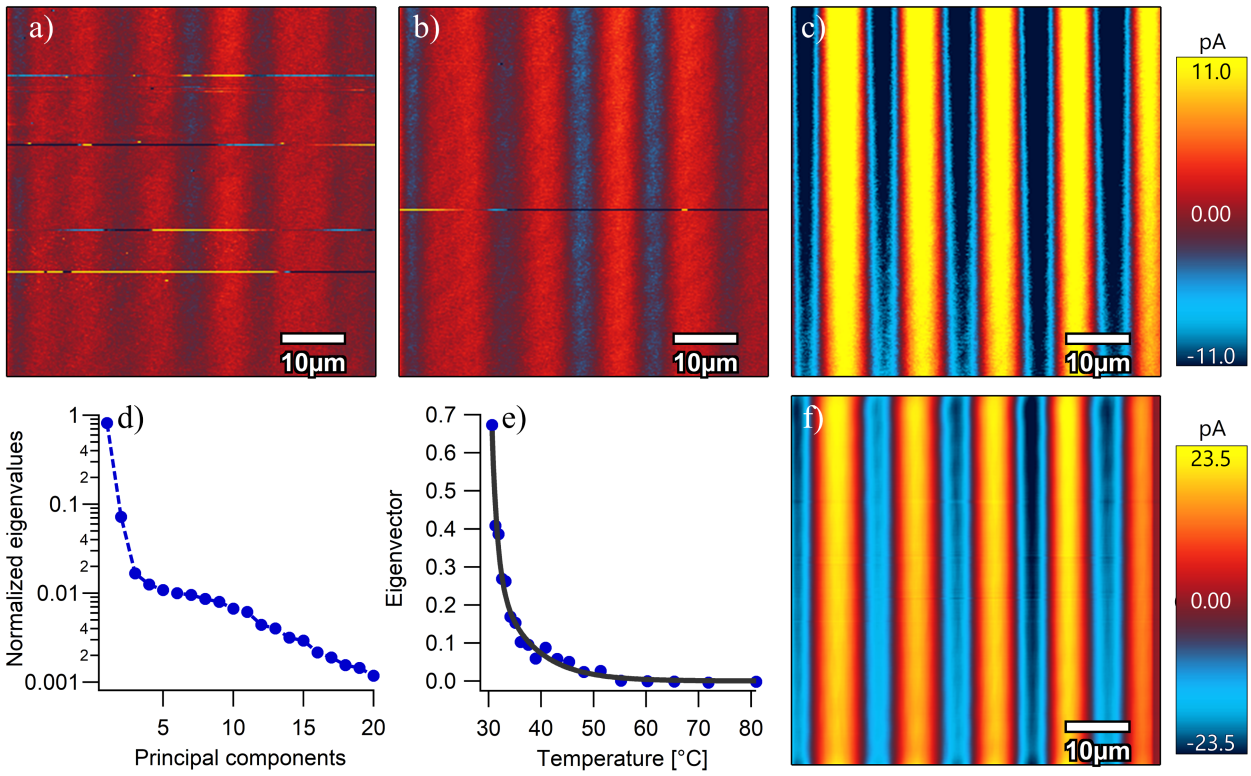

Figure 5.4: CGM under different temperatures; (a-c) raw CGM current mappings acquired under temperatures of 71.9 °C (a), 40.8 °C (b), and 30.6 °C (c); (d-f) PCA of temperature-dependent images: scree plot of eigenvalues (d), the first PCA eigenvector (e), and its corresponding component image (f). The scan speed in all 20 images was 1.2 mm/s.

the screening surface charge density $|\sigma_d|$ can be estimated by averaging the collected absolute domain charges $|Q_d|$ over the number of pixels n and the tip area as $|\sigma_d| = |Q_d|/(n \times A_{tip})$. The extent of surface screening is assessed by finding the ratio of $|\sigma_d|/P_s$.

A simple example of this analysis is visualized in Figure 5.5. A trace and a retrace line scans of a CGM image are shown in Figure 5.5a. With the CGM probe speed given, the absolute value of these signals as a function scan time were calculated and shown in Figure 5.5b. The area under these curve is the collected charges, which were scraped over domains and domain walls. To separate these two mechanisms of charge scraping, the signals were masked based on a predefined threshold. The corresponding domain signals are obtained

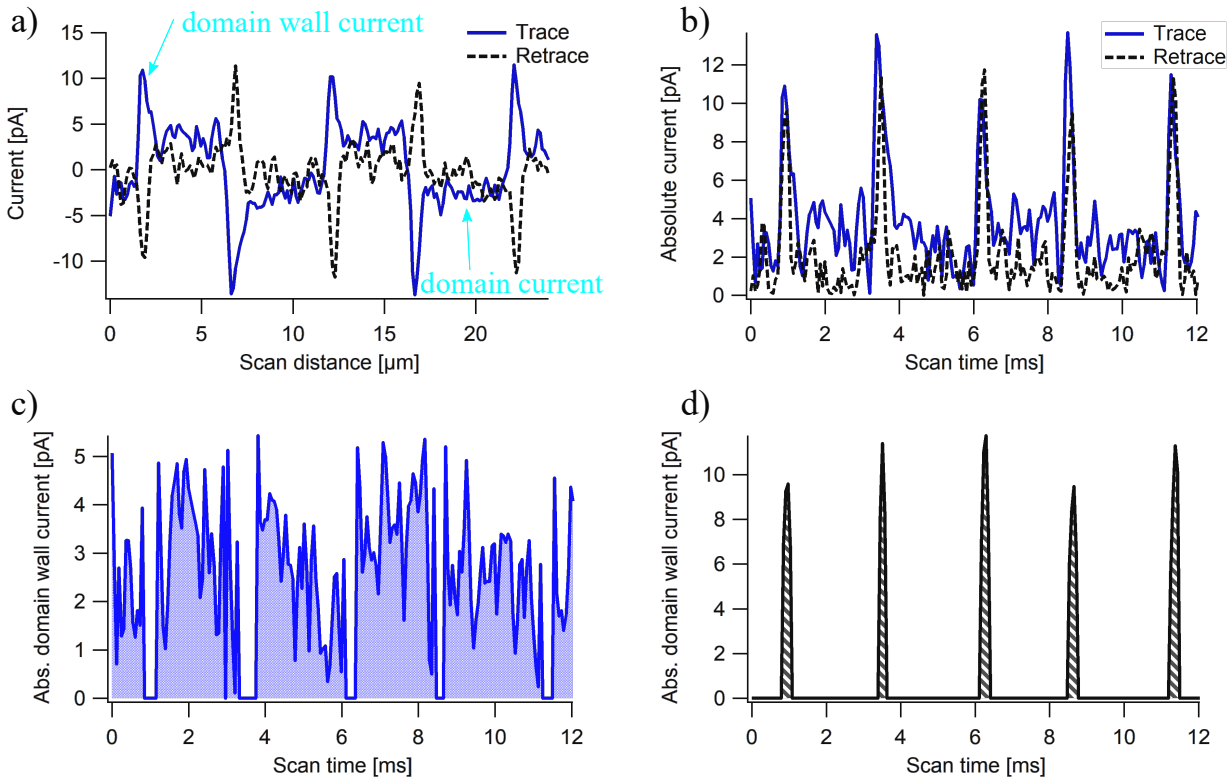

Figure 5.5: Calculation of collected domain and domain wall charges via CGM current signals. Line profiles of (a) trace and retrace CGM image as a function of scan distance; (b) absolute trace and retrace line profiles of CGM image as a function of scan time; (c) masked trace signal only over domains; and (d) masked retrace signal only over the domain walls.

by masking the trace signal and removing the values bigger than the threshold of 7 pA, while the domain wall signals were acquired by ignoring the retrace values less than 5.5 pA. The shaded area under the curve in Figure 5.5c is equal to the absolute scraped charge over 5 domains while the shaded area in Figure 5.5d is equal to the scraped charge over 5 domain walls.

The retrace signal is dominated by the domain wall charges (Figure 5.6a). In order to consider the domain wall effect, the current image was masked by replacing all the absolute values less than 5.5 pA with zero (Figure 5.6b). The area under each line scan of this image is found with respect to the time of scan, summed over all line scans, and the total collected

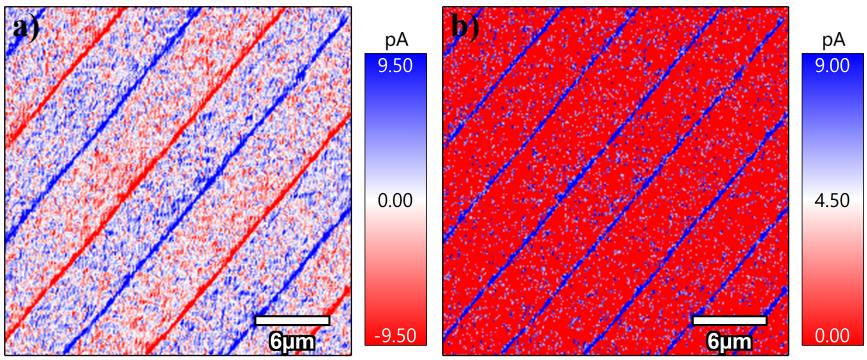

Figure 5.6: CGM retrace image (a), and the masked retrace image with threshold of 5.5 pA (b).

charge over all domain walls found to be $|Q_w| \cong 6.12$ pC. It is found that the number of current spikes corresponding to the domain wall crossing is around $n = 1040$. The estimated polarization is defined as $P_s \approx \frac{|Q_w|}{2A_{tip} \times n} = 46.22\ \mu\text{C/cm}^2$.

The trace signal contains the scraped charge over the domains. To remove the domain wall current spikes, the trace CGM image (shown in Figure 5.7a) is masked by considering only absolute current values less than the threshold of 7 pA. Figure 5.7b shows the absolute current values only over the domains. The sum of areas under each line scan of this image with respect to the time is the total charge collected over the domains and is equal to $|Q_d| = 9.076$ pC. The number of pixels with non-zero values (corresponding to domain charges) in Figure 5.7b is equal to 50173 and the average collected domain charge per pixel is equal $|Q_{dp}| = 0.1809$ fC/pixel . In turn, The surface charge density $|\sigma_d|$ is estimated as $|\sigma_d| = \frac{|Q_{dp}|}{A_{tip}} = 2.84\ \mu$ C/cm^2. The extent of surface screening is estimated by comparing the estimated domain charge density $|\sigma|$ with the ideal surface charge of ferroelectric surface, which should be equal to polarization charges $P_s = 80\ \mu$C/cm^2, and found 3.55% screening ratio. Both spontaneous polarization and surface charge density estimated from experimental data appear to be relatively low, perhaps because of the partial screening of polarization charges and incomplete scraping and refilling of surface charges under moving CGM probe.

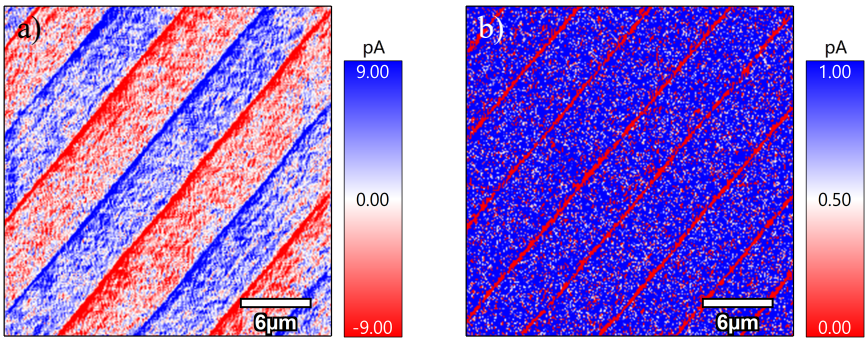

Figure 5.7: CGM trace image (a), and masked image with threshold of 7 pA (b). The masked image only captures the current signal over the domains.

5.4 Conclusions

In summary, CGM and PCA approaches are used to image ferroelectric domains of PPLN. The CGM signal increases linearly with the scan speed while decreases via power law with the temperature. The observations are consistent with proposed imaging mechanisms of scraping and refilling of surface screening charge within domains, and polarization change across domain wall, enabling the estimation of the spontaneous polarization and the density of surface charges with order of magnitude agreement with literature data. The study demonstrates the capabilities of PCA in reduce noise level and enhancing signal-to-noise ratio, making quantitative analysis of noise raw data possible.

Chapter 6

CONCLUSIONS AND FUTURE WORK

6.1 Conclusions

The dissertation focused on development of advanced atomic force microscopy techniques. A review of the state-of-the-art methods available for nanoscale characterization of electromechanical responses was provided in Chapter 1. The different signal formation mechanisms, means and methods to distinguish the coupling effects, and different excitation and detection schemes were explained. The challenges that motivated this dissertation and the the dissertation scope were discussed at the end.

In Chapter 2, three different excitation and detection schemes were developed that can be used in variety of resonance-enhanced AFM techniques. The simple harmonic oscillator (SHO) model was used as a physical model to explain the tip-sample contact interaction near contact resonance frequency. The multi-harmonic dual resonance tracking was introduced, and the development and implementations details were explained. The SHO parameters (intrinsic properties) were extracted based on the dual amplitude and phase responses at each pixel and examples of intrinsic and frequency-dependent responses were provided. The method was successfully applied to measure the 4^{th} harmonic response, track the resonance frequency and extract intrinsic responses with minimal cross-talks. The second developed method was an open loop sequential excitation (SE) which performs a series of fast single-frequency excitations and analyzes the data set through principal component analysis (PCA) and consequently SHO analysis. The details of PCA and SHO parameter extraction were offered. The SE-piezoresponse force microscopy (SE-PFM) experiments were performed on a PZT ceramic and the obtained data were compared to conventional PFM. The SE-PFM exhibited more accurate characterization of piezoelectricity with minimal cross-talks. The

third method, big-data AFM, was based on full information acquisition of cantilever motion in time domain. The need for big-data AFM and details of implementation were explained. The method was used to perform fast spectroscopy switching in PFM mode with and without super-coercive voltage on thin-film BFO. The Wavelet-based time-frequency and phase coherence analyses were used to observe the switching phenomena. Finally, dimensional reduction based on PCA were performed and the low-rank data were analyzed with SHO model.

Scanning thermo-ionic microscopy (STIM) was invented and developed for probing local ionic concentration and was introduced in Chapter 3. STIM works based on imaging the Vegard strain induced via thermal and hydrostatic stress excitations. The principle of STIM, signal formation mechanisms and different excitation sources were explained, and the obtained results from Sm-doped ceria and halide perovskites solar cells were offered. Furthermore, the detection schemes developed in previous chapter were utilized to obtain thermo-mechanical and thermo-ionic properties of samples. The multi-harmonic dual resonance tracking was implemented for STIM measurements and the intrinsic properties were found based on SHO regression analysis. The big-data STIM exhibited interesting behaviors in acquired deflection time-frequency response. There were the first, second, third and fourth harmonic responses corresponding to Vegard strain, thermo-mechanical, mixed effects and ionic effects. An advantage of big-data method is the availability of displacement signals in time-frequency domains and can be used to filter certain phenomena. By filtering out the first, second, and third harmonics (which were not relevant to ionic motion), the responses were not sensitive to the electromechanical, electrostatic, and capacitive effects, making in-operando testing possible.

The ability to control local temperatures motivated the work for Chapter 4. The heated AFM probe was used not only as a heater but also as a temperature sensor. It was found that under certain conditions, the temperature and in turn the electrical resistance of the heated probe are correlated with the thermal conductivity of the sample material. A combination of numerical and experimental tests was performed to obtain a semi-analytical relationship

between the sample thermal conductivity and electrical resistance of heated probe. The effects of contact resistance and heat losses due to convection and radiation were studied via numerical simulations. The method was applied on a three-phase thermoelectric and it was found that the thermal conductivity of the sample can be quantitatively characterized with 100 nm spatial resolution and good accuracy. The method was shown to be a powerful tool for design and optimization of thermoelectric materials.

Finally, in Chapter5 the recently developed charge gradient microscopy (CGM) was used to characterize the ferroelectric domains, domain walls and the surface charge removal and redistribution on a periodically poled lithium niobate sample. Contradictory to PFM indirect and qualitative measurements, this method directly measured the current in a hard contact with sample. The measured current in trace and retrace passes showed to have fundamental differences. It was shown the signal formation mechanism on domains and domain walls were different and the origin of the signals were investigated. The obtained currents as a function of scan speed and temperature are analyzed using PCA. Interestingly, it was found that the current signals proportionally enhance with the scan speed, while PFM measurements suffer from slow speeds.

6.2 Future work

The excitation and detection schemes developed in this dissertation can be applied to a broad range of AFM techniques. The SE method is currently under investigation for application in Kelvin probe force microscopy and in general can be applied to any AFM method where the feedback errors or cross-talks exist. The big-data framework developed here allows for arbitrary excitation and acquisition of multiple sources. Limited by experimental and instrumentation resources, the concept is demonstrated with only one input channel acquired at intermediate sampling rates. In future, this method should be extended with capabilities for on-the-fly adjustment of the excitation sources, and acquisition of multi-dimensional datasets. Furthermore, the PCA analysis performed here are unsupervised in nature, making the extraction of physical information difficult. More sophisticated methods such as multi-

resolution dynamic mode decomposition (mr-DMD) [134] and dynamic mode decomposition with control [210] should be employed to robustly separate complex dynamics of the systems such as tip-sample interaction with multiple eigen-modes of vibration into a hierarchy of multi-resolution time-scale components. Finally, the ultimate goal is to enable machine learning-based adaptive AFM experimentation based on ever growing training data, (*i.e.*, the AFM is capable of recognizing critical spots and key features during scans and matching them with underlying physical processes on-the-fly, and thus autonomously adjust experimental parameters for refined and more targeted probing without user's input).

All AFMs used in this study measure the cantilever deflection via an optical beam deflector. Recently a metrological AFM is introduced that used a laser vibrometer to directly measure the displacement and speed of the cantilever [211]. For dynamic-strain based techniques, it is desirable to measure the displacement via vibrometer due to its quantitative measurements, improved signal-to-noise-ratio and the fact that it can measure the displacement on top of the tip, isolating the other responses acting on the body of the cantilever.

Scanning thermo-ionic microscopy, developed in the context of this dissertation, has shown promising results for characterization of ionic concentration. Further analysis, simulations and experiments are needed to verify this technique. Time- and voltage-spectroscopic studies are needed to study and distinguish ionic diffusion and ionic migration and fully understand electrochemical activity under the STIM. Experimental tests under a global excitation of the sample can reveal similar information. Besides, the mathematical analysis provided in this dissertation is one possible nonlinear response. One may need to also include thermally-induced defect formation and thermally drive transport that may have contributed to the signal. It would be also highly desirable to accurately control and maintain the temperature of heated probe during STIM measurements. In materials with homogeneous thermal conductivity distribution, the change of temperature in heated probe is minimal and thus the effect can be ignored.

The SThM results provided in Chapter 4 are based on DC excitation of thermal probe and similar to other DC methods are prone to noises and suffer from low DC acquisition

time. Application of an alternating bias to the probe tip, would results in third harmonic voltage component which can be measured and correlated to thermal conductivity, known as 3ω method [212]. The method can overcome the difficulties associated with the current SThM and increase the spatial resolution of the method. In order to fully characterize the thermoelectric materials properties, one can use thermal probes to measure the Seebeck coefficient simultaneous to SThM measurements.

The charge gradient microscopy results in Chapter 5 are interesting. As the scan speed increases, the measured current is linearly scaled up and the responses enhance. However, the bottleneck is the bandwidth of the current detection system that puts an upper threshold for scan rates to around 40 Hz/line. Improving the bandwidth of the current detection system allows for ideal charge removal and direct detection of spontaneous polarization based on measured currents.

BIBLIOGRAPHY

[1] R. K. Vasudevan, N. Balke, P. Maksymovych, S. Jesse, and S. V. Kalinin, "Ferroelectric or non-ferroelectric: Why so many materials exhibit ferroelectricity on the nanoscale," *Applied Physics Reviews*, vol. 4, p. 021302, jun 2017.

[2] Q. N. Chen, Y. Ou, F. Ma, and J. Li, "Mechanisms of electromechanical coupling in strain based scanning probe microscopy," *Applied Physics Letters*, vol. 104, p. 242907, jun 2014.

[3] A. Labuda and R. Proksch, "Quantitative measurements of electromechanical response with a combined optical beam and interferometric atomic force microscope," *Applied Physics Letters*, vol. 106, no. 25, p. 253103, 2015.

[4] S. Somnath, A. Belianinov, S. V. Kalinin, and S. Jesse, "Rapid mapping of polarization switching through complete information acquisition," *Nature Communications*, vol. 7, p. 13290, 2016.

[5] G. Binnig and H. Rohrer, "Scanning tunneling microscopy," *Surface science*, vol. 126, no. 1-3, pp. 236–244, 1983.

[6] G. Binnig, C. F. Quate, and C. Gerber, "Atomic force microscope," *Phys. Rev. Lett.*, vol. 56, pp. 930–933, Mar 1986.

[7] W. G. Cady, "Piezoelectricity: an introduction to the theory and applications of electromechanical phenomena in crystals," 1946.

[8] A. Devonshire, "Theory of ferroelectrics," *Advances in physics*, vol. 3, no. 10, pp. 85–130, 1954.

[9] S. V. Kalinin and D. A. Bonnell, "Imaging mechanism of piezoresponse force microscopy of ferroelectric surfaces," *Physical Review B - Condensed Matter and Materials Physics*, vol. 65, no. 12, pp. 1–11, 2002.

[10] . A. Roelofs, U. Böttger, R. Waser, F. Schlaphof, S. Trogisch, and L. Eng, "Differentiating 180 and 90 switching of ferroelectric domains with three-dimensional piezoresponse force microscopy," *Applied Physics Letters*, vol. 77, no. 21, pp. 3444–3446, 2000.

[11] A. N. Morozovska, E. A. Eliseev, Y. Li, S. V. Svechnikov, P. Maksymovych, V. Y. Shur, V. Gopalan, L.-Q. Chen, and S. V. Kalinin, "Thermodynamics of nanodomain formation and breakdown in scanning probe microscopy: Landau-ginzburg-devonshire approach," *Physical Review B*, vol. 80, no. 21, p. 214110, 2009.

[12] N. Balke, S. Choudhury, S. Jesse, M. Huijben, Y. H. Chu, A. P. Baddorf, L.-Q. Chen, R. Ramesh, and S. V. Kalinin, "Deterministic control of ferroelastic switching in multiferroic materials," *Nature nanotechnology*, vol. 4, no. 12, p. 868, 2009.

[13] S. Jesse, A. P. Baddorf, and S. V. Kalinin, "Switching spectroscopy piezoresponse force microscopy of ferroelectric materials," *Applied Physics Letters*, vol. 88, no. 6, pp. 1–4, 2006.

[14] E. Karapetian, M. Kachanov, and S. V. Kalinin, "Stiffness relations for piezoelectric indentation of flat and non-flat punches of arbitrary planform: applications to probing nanoelectromechanical properties of materials," *Journal of the Mechanics and Physics of Solids*, vol. 57, no. 4, pp. 673–688, 2009.

[15] C. Ahn, J.-M. Triscone, and J. Mannhart, "Electric field effect in correlated oxide systems," *Nature*, vol. 424, no. 6952, p. 1015, 2003.

[16] S. V. Kalinin, B. Mirman, and E. Karapetian, "Relationship between direct and converse piezoelectric effect in a nanoscale electromechanical contact," *Physical Review B*, vol. 76, no. 21, p. 212102, 2007.

[17] A. N. Morozovska, E. A. Eliseev, S. L. Bravina, and S. V. Kalinin, "Resolution-function theory in piezoresponse force microscopy: Wall imaging, spectroscopy, and lateral resolution," *Physical Review B*, vol. 75, no. 17, p. 174109, 2007.

[18] L. Tian, A. Vasudevarao, A. N. Morozovska, E. A. Eliseev, S. V. Kalinin, and V. Gopalan, "Nanoscale polarization profile across a 180 ferroelectric domain wall extracted by quantitative piezoelectric force microscopy," *Journal of Applied Physics*, vol. 104, no. 7, p. 074110, 2008.

[19] S. Hong, J. Woo, H. Shin, J. U. Jeon, Y. E. Pak, E. L. Colla, N. Setter, E. Kim, and K. No, "Principle of ferroelectric domain imaging using atomic force microscope," *Journal of Applied Physics*, vol. 89, no. 2, pp. 1377–1386, 2001.

[20] A. N. Morozovska, S. V. Svechnikov, E. A. Eliseev, B. J. Rodriguez, S. Jesse, and S. V. Kalinin, "Local polarization switching in the presence of surface-charged defects: Microscopic mechanisms and piezoresponse force spectroscopy observations," *Physical Review B*, vol. 78, no. 5, p. 054101, 2008.

[21] C. Ganpule, V. Nagarajan, H. Li, A. Ogale, D. Steinhauer, S. Aggarwal, E. Williams, R. Ramesh, and P. De Wolf, "Role of 90 domains in lead zirconate titanate thin films," *Applied Physics Letters*, vol. 77, no. 2, pp. 292–294, 2000.

[22] M. Alexe, C. Harnagea, D. Hesse, and U. Gösele, "Patterning and switching of nanosize ferroelectric memory cells," *Applied physics letters*, vol. 75, no. 12, pp. 1793–1795, 1999.

[23] J. Seidel, P. Maksymovych, Y. Batra, A. Katan, S.-Y. Yang, Q. He, A. P. Baddorf, S. V. Kalinin, C.-H. Yang, J.-C. Yang, *et al.*, "Domain wall conductivity in la-doped bifeo 3," *Physical Review Letters*, vol. 105, no. 19, p. 197603, 2010.

[24] V. Likodimos, X. Orlik, L. Pardi, M. Labardi, and M. Allegrini, "Dynamical studies of the ferroelectric domain structure in triglycine sulfate by voltage-modulated scanning force microscopy," *Journal of Applied Physics*, vol. 87, no. 1, pp. 443–451, 2000.

[25] F. Saurenbach, , and B. Terris, "Imaging of ferroelectric domain walls by force microscopy," *Applied physics letters*, vol. 56, no. 17, pp. 1703–1705, 1990.

[26] C. Ganpule, A. Roytburd, V. Nagarajan, B. Hill, S. Ogale, E. Williams, R. Ramesh, and J. Scott, "Polarization relaxation kinetics and 180 domain wall dynamics in ferroelectric thin films," *Physical Review B*, vol. 65, no. 1, p. 014101, 2001.

[27] B. J. Rodriguez, A. Gruverman, A. Kingon, R. Nemanich, and J. Cross, "Three-dimensional high-resolution reconstruction of polarization in ferroelectric capacitors by piezoresponse force microscopy," *Journal of Applied Physics*, vol. 95, no. 4, pp. 1958–1962, 2004.

[28] Y. Liu, Y. Zhang, M. J. Chow, Q. N. Chen, and J. Li, "Biological ferroelectricity uncovered in aortic walls by piezoresponse force microscopy," *Physical Review Letters*, vol. 108, p. 078103, feb 2012.

[29] S. B. Lang, "Piezoelectricity, pyroelectricity and ferroelectricity in biomaterials: Speculation on their biological significance," *IEEE Transactions on Dielectrics and Electrical Insulation*, vol. 7, no. 4, pp. 466–473, 2000.

[30] E. Fukada and I. Yasuda, "On the piezoelectric effect of bone," *Journal of the physical society of Japan*, vol. 12, no. 10, pp. 1158–1162, 1957.

[31] A. A. Marino and R. O. Becker, "Piezoelectric effect and growth control in bone," *Nature*, vol. 228, no. 5270, p. 473, 1970.

[32] S. V. Kalinin, B. J. Rodriguez, J. Shin, S. Jesse, V. Grichko, T. Thundat, A. P. Baddorf, and A. Gruverman, "Bioelectromechanical imaging by scanning probe microscopy: Galvani's experiment at the nanoscale," *Ultramicroscopy*, vol. 106, no. 4-5, pp. 334–340, 2006.

[33] A. N. Morozovska, E. A. Eliseev, N. Balke, and S. V. Kalinin, "Local probing of ionic diffusion by electrochemical strain microscopy: Spatial resolution and signal formation mechanisms," *Journal of Applied Physics*, vol. 108, no. 5, p. 053712, 2010.

[34] A. Eshghinejad and J. Li, "The coupled lithium ion diffusion and stress in battery electrodes," *Mechanics of Materials*, vol. 91, pp. 343–350, 2015.

[35] A. Eshghinejad, E. Nasr Esfahani, C. Lei, and J. Li, "Resolving Local Electrochemistry at the Nanoscale via Electrochemical Strain Microscopy : Modeling and Experiments," *arXiv*, pp. 1–16, apr 2017.

[36] Q. N. Chen, S. B. Adler, and J. Li, "Imaging space charge regions in sm-doped ceria using electrochemical strain microscopy," *Applied Physics Letters*, vol. 105, no. 20, p. 201602, 2014.

[37] A. Kumar, F. Ciucci, A. N. Morozovska, S. V. Kalinin, and S. Jesse, "Measuring oxygen reduction/evolution reactions on the nanoscale," *Nature Chemistry*, vol. 3, pp. 707–713, aug 2011.

[38] S. B. Adler, B. S. Gerwe, E. N. Esfahani, P. Wang, Q. N. Chen, and J. Li, "Imaging Space Charge Regions in Sm-Doped Ceria Using Strain-Based Scanning Probe Techniques," in *ECS Transactions*, vol. 78, pp. 335–342, The Electrochemical Society, sep 2017.

[39] A. Eshghinejad, E. Nasr Esfahani, P. Wang, S. Xie, T. C. Geary, S. B. Adler, and J. Li, "Scanning thermo-ionic microscopy for probing local electrochemistry at the nanoscale," *Journal of Applied Physics*, vol. 119, p. 205110, may 2016.

[40] D. Seol, S. Park, O. V. Varenyk, S. Lee, H. N. Lee, A. N. Morozovska, and Y. Kim, "Determination of ferroelectric contributions to electromechanical response by frequency dependent piezoresponse force microscopy," *Scientific reports*, vol. 6, p. 30579, 2016.

[41] R. Proksch, "In-situ piezoresponse force microscopy cantilever mode shape profiling," *Journal of Applied Physics*, vol. 118, p. 072011, aug 2015.

[42] T. Jungk, Á. Hoffmann, and E. Soergel, "Challenges for the determination of piezoelectric constants with piezoresponse force microscopy," *Applied Physics Letters*, vol. 91, no. 25, p. 253511, 2007.

[43] S. V. Kalinin, A. Rar, and S. Jesse, "A decade of piezoresponse force microscopy: progress, challenges, and opportunities," *IEEE transactions on ultrasonics, ferroelectrics, and frequency control*, vol. 53, no. 12, 2006.

[44] K. Franke, H. Huelz, and M. Weihnacht, "How to extract spontaneous polarization information from experimental data in electric force microscopy," *Surface science*, vol. 415, no. 1-2, pp. 178–182, 1998.

[45] A. Gannepalli, D. G. Yablon, A. H. Tsou, and R. Proksch, "Mapping nanoscale elasticity and dissipation using dual frequency contact resonance AFM," *Nanotechnology*, vol. 22, p. 159501, sep 2011.

[46] S. Jesse, S. V. Kalinin, R. Proksch, A. P. Baddorf, and B. J. Rodriguez, "The band excitation method in scanning probe microscopy for rapid mapping of energy dissipation on the nanoscale," *Nanotechnology*, vol. 18, p. 435503, oct 2007.

[47] S. Bradler, A. Schirmeisen, and B. Roling, "Piezoresponse force and electrochemical strain microscopy in dual ac resonance tracking mode: Analysis of tracking errors," *Journal of Applied Physics*, vol. 123, no. 3, p. 035106, 2018.

[48] L. Collins, A. Belianinov, S. Somnath, B. J. Rodriguez, N. Balke, S. V. Kalinin, and S. Jesse, "Multifrequency spectrum analysis using fully digital g mode-kelvin probe force microscopy," *Nanotechnology*, vol. 27, no. 10, p. 105706, 2016.

[49] G. Binnig, C. F. Quate, and C. Gerber, "Atomic force microscope," *Physical review letters*, vol. 56, no. 9, p. 930, 1986.

[50] S.-i. Kitamura and M. Iwatsuki, "Observation of 7× 7 reconstructed structure on the silicon (111) surface using ultrahigh vacuum noncontact atomic force microscopy," *Japanese journal of applied physics*, vol. 34, no. 1B, p. L145, 1995.

[51] R. García, "Dynamic atomic force microscopy methods," *Surface Science Reports*, vol. 47, pp. 197–301, sep 2002.

[52] Q. Zhong, D. Inniss, K. Kjoller, and V. Elings, "Fractured polymer/silica fiber surface studied by tapping mode atomic force microscopy," *Surface Science Letters*, vol. 290, no. 1-2, pp. L688–L692, 1993.

[53] M. Nonnenmacher, M. oBoyle, and H. K. Wickramasinghe, "Kelvin probe force microscopy," *Applied physics letters*, vol. 58, no. 25, pp. 2921–2923, 1991.

[54] E. Nasr Esfahani, A. Eshghinejad, Y. Ou, J. Zhao, S. Adler, and J. Li, "Scanning Thermo-ionic Microscopy: Probing Nanoscale Electrochemistry via Thermal Stress-induced Oscillation," *Microscopy Today*, vol. 25, pp. 12–19, nov 2017.

[55] D. C. Coffey and D. S. Ginger, "Time-resolved electrostatic force microscopy of polymer solar cells," *Nature Materials*, vol. 5, pp. 735–740, sep 2006.

[56] A. Morozovska, E. Eliseev, N. Balke, and S. V. Kalinin, "Local probing of ionic diffusion by electrochemical strain microscopy: Spatial resolution and signal formation mechanisms," *Journal of Applied Physics*, vol. 108, no. 5, p. 053712, 2010.

[57] C. Mody, *Instrumental community: Probe microscopy and the path to nanotechnology.* MIT Press, 2011.

[58] E. T. Herruzo, A. P. Perrino, and R. Garcia, "Fast nanomechanical spectroscopy of soft matter," *Nature communications*, vol. 5, p. 3126, 2014.

[59] N. Martinez, J. R. Lozano, E. Herruzo, F. Garcia, C. Richter, T. Sulzbach, and R. Garcia, "Bimodal atomic force microscopy imaging of isolated antibodies in air and liquids," *Nanotechnology*, vol. 19, no. 38, p. 384011, 2008.

[60] D. Martinez-Martin, E. Herruzo, C. Dietz, J. Gomez-Herrero, and R. Garcia, "Noninvasive protein structural flexibility mapping by bimodal dynamic force microscopy," *Physical review letters*, vol. 106, no. 19, p. 198101, 2011.

[61] E. A. Tholén, D. Platz, D. Forchheimer, V. Schuler, M. O. Tholén, C. Hutter, and D. B. Haviland, "Note: The intermodulation lockin analyzer," *Review of Scientific Instruments*, vol. 82, no. 2, p. 026109, 2011.

[62] S. Jesse, S. Somnath, L. Collins, and S. Kalinin, "Full information acquisition in scanning probe microscopy," *Microscopy Today*, vol. 25, no. 4, pp. 34–45, 2017.

[63] S. Jesse and S. V. Kalinin, "Band excitation in scanning probe microscopy: sines of change," *Journal of Physics D: Applied Physics*, vol. 44, no. 46, p. 464006, 2011.

[64] A. P. French, "Vibrations and waves," 2001.

[65] A. Gruverman, O. Auciello, J. Hatano, and H. Tokumoto, "Scanning force microscopy as a tool for nanoscale study of ferroelectric domains," *Ferroelectrics*, vol. 184, no. 1, pp. 11–20, 1996.

[66] S. Wold, K. Esbensen, and P. Geladi, "Principal component analysis," *Chemometrics and Intelligent Laboratory Systems*, vol. 2, no. 1-3, pp. 37–52, 1987.

[67] M. Gavish and D. L. Donoho, "The optimal hard threshold for singular values is $4/\sqrt{3}$," *IEEE Transactions on Information Theory*, vol. 60, pp. 5040–5053, Aug 2014.

[68] A. Gruverman and A. Kholkin, "Nanoscale ferroelectrics: processing, characterization and future trends," *Reports on Progress in Physics*, vol. 69, no. 8, p. 2443, 2005.

[69] B. J. Rodriguez, C. Callahan, S. V. Kalinin, and R. Proksch, "Dual-frequency resonance-tracking atomic force microscopy," *Nanotechnology*, vol. 18, p. 475504, nov 2007.

[70] P. Girard, "Electrostatic force microscopy: principles and some applications to semiconductors," *Nanotechnology*, vol. 12, no. 4, p. 485, 2001.

[71] C. Gao, T. Wei, F. Duewer, Y. Lu, and X.-D. Xiang, "High spatial resolution quantitative microwave impedance microscopy by a scanning tip microwave near-field microscope," *Applied Physics Letters*, vol. 71, no. 13, pp. 1872–1874, 1997.

[72] S. Jesse and S. V. Kalinin, "Principal component and spatial correlation analysis of spectroscopic-imaging data in scanning probe microscopy," *Nanotechnology*, vol. 20, no. 8, p. 085714, 2009.

[73] A. Przybylski, B. Thiel, J. Keller-Findeisen, B. Stock, and M. Bates, "Gpufit: An open-source toolkit for GPU-accelerated curve fitting," *Scientific Reports*, vol. 7, p. 15722, dec 2017.

[74] S. V. Kalinin, E. Strelcov, A. Belianinov, S. Somnath, R. K. Vasudevan, E. J. Lingerfelt, R. K. Archibald, C. Chen, R. Proksch, N. Laanait, and S. Jesse, "Big, Deep, and Smart Data in Scanning Probe Microscopy," *ACS Nano*, vol. 10, no. 10, pp. 9068–9086, 2016.

[75] A. Belianinov, S. V. Kalinin, and S. Jesse, "Complete information acquisition in dynamic force microscopy," *Nature Communications*, vol. 6, p. 6550, dec 2015.

[76] J. M. Tarascon and M. Armand, "Issues and challenges facing rechargeable lithium batteries," *Nature*, vol. 414, no. 6861, pp. 359–367, 2001.

[77] B. Dunn, H. Kamath, and J.-M. Tarascon, "Electrical energy storage for the grid: a battery of choices," *Science*, vol. 334, no. 6058, pp. 928–935, 2011.

[78] M. S. Whittingham, "Lithium batteries and cathode materials," *Chemical reviews*, vol. 104, no. 10, pp. 4271–4302, 2004.

[79] R. Borup, J. Meyers, B. Pivovar, Y. S. Kim, R. Mukundan, N. Garland, D. Myers, M. Wilson, F. Garzon, D. Wood, *et al.*, "Scientific aspects of polymer electrolyte fuel cell durability and degradation," *Chemical reviews*, vol. 107, no. 10, pp. 3904–3951, 2007.

[80] S. B. Adler, "Factors governing oxygen reduction in solid oxide fuel cell cathodes," *Chemical Reviews*, vol. 104, no. 10, pp. 4791–4843, 2004.

[81] S. Kim, J. Yan, B. Schwenzer, J. Zhang, L. Li, J. Liu, Z. G. Yang, and M. A. Hickner, "Cycling performance and efficiency of sulfonated poly (sulfone) membranes in vanadium redox flow batteries," *Electrochemistry Communications*, vol. 12, no. 11, pp. 1650–1653, 2010.

[82] C. Graves, S. D. Ebbesen, M. Mogensen, and K. S. Lackner, "Sustainable hydrocarbon fuels by recycling co2 and h2o with renewable or nuclear energy," *Renewable and Sustainable Energy Reviews*, vol. 15, no. 1, pp. 1–23, 2011.

[83] B. A. Pinaud, J. D. Benck, L. C. Seitz, A. J. Forman, Z. Chen, T. G. Deutsch, B. D. James, K. N. Baum, G. N. Baum, S. Ardo, *et al.*, "Technical and economic feasibility of centralized facilities for solar hydrogen production via photocatalysis and photoelectrochemistry," *Energy & Environmental Science*, vol. 6, no. 7, pp. 1983–2002, 2013.

[84] A. S. Aricò, P. Bruce, B. Scrosati, J. M. Tarascon, and W. Van Schalkwijk, "Nanostructured materials for advanced energy conversion and storage devices," *Nature Materials*, vol. 4, pp. 366–377, may 2005.

[85] C. Groves, O. G. Reid, and D. S. Ginger, "Heterogeneity in polymer solar cells: Local morphology and performance in organic photovoltaics studied with scanning probe microscopy," *Accounts of Chemical Research*, vol. 43, pp. 612–620, may 2010.

[86] S. V. Kalinin and N. Balke, "Local electrochemical functionality in energy storage materials and devices by scanning probe microscopies: Status and perspectives," *Advanced Materials*, vol. 22, pp. E193–E209, sep 2010.

[87] Z. Huang, P. De Wolf, R. Poddar, C. Li, A. Mark, M. R. Nellist, Y. Chen, J. Jiang, G. Papastavrou, S. W. Boettcher, *et al.*, "Peakforce scanning electrochemical microscopy with nanoelectrode probes," *Microscopy Today*, vol. 24, no. 6, pp. 18–25, 2016.

[88] A. J. Bard and M. V. Mirkin, *Scanning electrochemical microscopy*. CRC Press, 2012.

[89] A. L. Barker, M. Gonsalves, J. V. MacPherson, C. J. Slevin, and P. R. Unwin, "Scanning electrochemical microscopy: Beyond the solid/liquid interface," *Analytica Chimica Acta*, vol. 385, no. 1-3, pp. 223–240, 1999.

[90] S. V. Kalinin and A. Gruverman, *Scanning probe microscopy: electrical and electromechanical phenomena at the nanoscale*, vol. 1. Springer Science & Business Media, 2007.

[91] A. R. Denton and N. W. Ashcroft, "Vegard's Law," *Physical Review A*, vol. 43, pp. 3161–3164, mar 1991.

[92] L. Vegard, "Die konstitution der mischkristalle und die raumfüllung der atome," *Zeitschrift für Physik*, vol. 5, no. 1, pp. 17–26, 1921.

[93] Y. Tian, A. Timmons, and J. R. Dahn, "In Situ AFM Measurements of the Expansion of Nanostructured SnCoC Films Reacting with Lithium," *Journal of The Electrochemical Society*, vol. 156, no. 3, p. A187, 2009.

[94] N. Balke, S. Jesse, Y. Kim, L. Adamczyk, A. Tselev, I. N. Ivanov, N. J. Dudney, and S. V. Kalinin, "Real space mapping of Li-ion transport in amorphous Si anodes with nanometer resolution," *Nano Letters*, vol. 10, pp. 3420–3425, sep 2010.

[95] Q. Nataly Chen, Y. Y. Liu, Y. Y. Liu, S. Xie, G. Cao, and J. Li, "Delineating local electromigration for nanoscale probing of lithium ion intercalation and extraction by electrochemical strain microscopy," *Applied Physics Letters*, vol. 101, no. 6, pp. 1–6, 2012.

[96] J. Zhu, J. Feng, L. Lu, and K. Zeng, "In situ study of topography, phase and volume changes of titanium dioxide anode in all-solid-state thin film lithium-ion battery by biased scanning probe microscopy," *Journal of Power Sources*, vol. 197, pp. 224–230, 2012.

[97] R. Proksch, "Electrochemical strain microscopy of silica glasses," *Journal of Applied Physics*, vol. 116, p. 066804, aug 2014.

[98] O. Kolosov, A. Gruverman, J. Hatano, K. Takahashi, and H. Tokumoto, "Nanoscale visualization and control of ferroelectric domains by atomic force microscopy," *Physical review letters*, vol. 74, no. 21, p. 4309, 1995.

[99] T. Keiji, K. Keiko, T. Kazuyoshi, and M. Hiroshi, "Strain imaging of lead-zirconate-titanate thin film by tunneling acoustic microscopy," *Japanese journal of applied physics*, vol. 33, no. 5S, p. 3193, 1994.

[100] P. Jiang, F. Yan, E. Nasr Esfahani, S. Xie, D. Zou, X. Liu, H. Zheng, and J. Li, "Electromechanical Coupling of Murine Lung Tissues Probed by Piezoresponse Force Microscopy," *ACS Biomaterials Science & Engineering*, vol. 3, no. 8, pp. 1827–1835, 2017.

[101] Q. N. Chen, F. Ma, S. Xie, Y. Liu, R. Proksch, and J. Li, "High sensitivity piezomagnetic force microscopy for quantitative probing of magnetic materials at the nanoscale," *Nanoscale*, vol. 5, p. 5747, jun 2013.

[102] A. Eshghinejad, W.-I. Liang, Q. N. Chen, F. Ma, Y. Liu, S. Xie, Y.-H. Chu, and J. Li, "Piezoelectric and piezomagnetic force microscopies of multiferroic bifeo3-limn2o4 heterostructures," *Journal of Applied Physics*, vol. 116, no. 6, p. 066805, 2014.

[103] F. Larché and J. W. Cahn, "A linear theory of thermochemical equilibrium of solids under stress," *Acta metallurgica*, vol. 21, no. 8, pp. 1051–1063, 1973.

[104] B. Nelson and W. King, "Temperature calibration of heated silicon atomic force microscope cantilevers," *Sensors and Actuators A: Physical*, vol. 140, no. 1, pp. 51 – 59, 2007.

[105] S. Somnath and W. P. King, "Heated atomic force cantilever closed loop temperature control and application to high speed nanotopography imaging," *Sensors and Actuators A: Physical*, vol. 192, pp. 27 – 33, 2013.

[106] A. Labuda, J. Cleveland, N. A. Geisse, M. Kocun, B. Ohler, R. Proksch, M. B. Viani, and D. Walters, "Photothermal excitation for improved cantilever drive performance in tapping mode atomic force microscopy," *Microscopy and Analysis28*, vol. 3, pp. S21–S25, 2014.

[107] B. A. Bircher, L. Duempelmann, H. P. Lang, C. Gerber, and T. Braun, "Photothermal excitation of microcantilevers in liquid: effect of the excitation laser position on temperature and vibrational amplitude," *IET Micro & Nano Letters*, vol. 8, no. 11, pp. 770–774, 2013.

[108] D. Y. Abramovitch, S. Hoen, and R. Workman, "Semi-automatic tuning of pid gains for atomic force microscopes," *Asian Journal of Control*, vol. 11, no. 2, pp. 188–195, 2009.

[109] H. Inaba and H. Tagawa, "Ceria-based solid electrolytes," *Solid state ionics*, vol. 83, no. 1-2, pp. 1–16, 1996.

[110] M. Mogensen, N. M. Sammes, and G. A. Tompsett, "Physical, chemical and electrochemical properties of pure and doped ceria," *Solid State Ionics*, vol. 129, no. 1-4, pp. 63–94, 2000.

[111] H. Tuller and A. Nowick, "Small polaron electron transport in reduced ceo2 single crystals," *Journal of Physics and Chemistry of Solids*, vol. 38, no. 8, pp. 859–867, 1977.

[112] A. Tschöpe, J. Y. Ying, and H. L. Tuller, "Catalytic redox activity and electrical conductivity of nanocrystalline non-stoichiometric cerium oxide," *Sensors and Actuators B: Chemical*, vol. 31, no. 1-2, pp. 111–114, 1996.

[113] H. L. Tuller, "Ionic conduction in nanocrystalline materials," *Solid State Ionics*, vol. 131, no. 1-2, pp. 143–157, 2000.

[114] J. Maier, "Defect chemistry at interfaces," *Solid State Ionics*, vol. 70, pp. 43–51, 1994.

[115] S. Kim and J. Maier, "On the conductivity mechanism of nanocrystalline ceria," *Journal of the Electrochemical society*, vol. 149, no. 10, pp. J73–J83, 2002.

[116] J. An, A. L. Koh, J. S. Park, R. Sinclair, T. M. Gur, and F. B. Prinz, "Aberration-corrected tem imaging of oxygen occupancy in ysz," *The journal of physical chemistry letters*, vol. 4, no. 7, pp. 1156–1160, 2013.

[117] A. Kumar, F. Ciucci, A. N. Morozovska, S. V. Kalinin, and S. Jesse, "Measuring oxygen reduction/evolution reactions on the nanoscale," *Nature chemistry*, vol. 3, no. 9, p. 707, 2011.

[118] A. Kumar, S. Jesse, A. N. Morozovska, E. Eliseev, A. Tebano, N. Yang, and S. V. Kalinin, "Variable temperature electrochemical strain microscopy of sm-doped ceria," *Nanotechnology*, vol. 24, no. 14, p. 145401, 2013.

[119] S. D. Stranks and H. J. Snaith, "Metal-halide perovskites for photovoltaic and light-emitting devices," *Nature Nanotechnology*, vol. 10, pp. 391–402, may 2015.

[120] R. Fang, W. J. Zhang, S. S. Zhang, and W. Chen, "The rising star in photovoltaics-perovskite solar cells: The past, present and future," *Science China Technological Sciences*, vol. 59, no. 7, pp. 989–1006, 2016.

[121] J. S. Manser, J. A. Christians, and P. V. Kamat, "Intriguing optoelectronic properties of metal halide perovskites," *Chemical reviews*, vol. 116, no. 21, pp. 12956–13008, 2016.

[122] J. Li, B. Huang, E. Nasr Esfahani, L. Wei, J. Yao, J. Zhao, and W. Chen, "Touching is believing: interrogating halide perovskite solar cells at the nanoscale via scanning probe microscopy," *npj Quantum Materials*, vol. 2, p. 56, dec 2017.

[123] T. Y. Yang, G. Gregori, N. Pellet, M. Grätzel, and J. Maier, "The Significance of Ion Conduction in a Hybrid Organic-Inorganic Lead-Iodide-Based Perovskite Photosensitizer," *Angewandte Chemie - International Edition*, vol. 54, no. 27, pp. 7905–7910, 2015.

[124] C. Li, S. Tscheuschner, F. Paulus, P. E. Hopkinson, J. Kießling, A. Köhler, Y. Vaynzof, and S. Huettner, "Iodine Migration and its Effect on Hysteresis in Perovskite Solar Cells," *Advanced Materials*, vol. 28, no. 12, pp. 2446–2454, 2016.

[125] Y. Yuan and J. Huang, "Ion Migration in Organometal Trihalide Perovskite and Its Impact on Photovoltaic Efficiency and Stability," *Accounts of Chemical Research*, vol. 49, no. 2, pp. 286–293, 2016.

[126] B. Chen, M. Yang, S. Priya, and K. Zhu, "Origin of J-V Hysteresis in Perovskite Solar Cells," *Journal of Physical Chemistry Letters*, vol. 7, no. 5, pp. 905–917, 2016.

[127] Y. Shao, Y. Fang, T. Li, Q. Wang, Q. Dong, Y. Deng, Y. Yuan, H. Wei, M. Wang, A. Gruverman, J. Shield, and J. Huang, "Grain boundary dominated ion migration in polycrystalline organicinorganic halide perovskite films," *Energy Environ. Sci.*, vol. 9, no. 5, pp. 1752–1759, 2016.

[128] W.-J. Yin, J.-H. Yang, J. Kang, Y. Yan, and S.-H. Wei, "Halide perovskite materials for solar cells: a theoretical review," *J. Mater. Chem. A*, vol. 3, no. 17, pp. 8926–8942, 2015.

[129] P. Wang, J. Zhao, L. Wei, Q. Zhu, S. Xie, J. Liu, X. Meng, and J. Li, "Photo-induced ferroelectric switching in perovskite CH ₃ NH ₃ PbI ₃ films," *Nanoscale*, vol. 9, no. 11, pp. 3806–3817, 2017.

[130] Y. Liu, R. K. Vasudevan, K. Pan, S. Xie, W.-I. Liang, A. Kumar, S. Jesse, Y.-C. Chen, Y.-H. Chu, V. Nagarajan, *et al.*, "Controlling magnetoelectric coupling by nanoscale phase transformation in strain engineered bismuth ferrite," *Nanoscale*, vol. 4, no. 10, pp. 3175–3183, 2012.

[131] H. Hayashi, M. Kanoh, C. J. Quan, H. Inaba, S. Wang, M. Dokiya, and H. Tagawa, "Thermal expansion of gd-doped ceria and reduced ceria," *Solid State Ionics*, vol. 132, no. 3-4, pp. 227–233, 2000.

[132] R. K. Kirby, "Thermal expansion of polytetrafluoroethylene (teflon) from- 190 to+ 300 c," *Journal of Research of the National Bureau of Standards*, vol. 57, no. 2, pp. 91–94, 1956.

[133] X. Xu and M. Wang, "Photocurrent hysteresis related to ion motion in metal-organic perovskites," *Science China Chemistry*, vol. 60, no. 3, pp. 396–404, 2017.

[134] J. N. Kutz, X. Fu, and S. L. Brunton, "Multi-Resolution Dynamic Mode Decomposition," *SIAM Journal on Applied Dynamical Systems*, vol. 15, pp. 713–735, jan 2015.

[135] G. J. Snyder and E. S. Toberer, "Complex thermoelectric materials," *Nature materials*, vol. 7, no. 2, p. 105, 2008.

[136] R. Venkatasubramanian, E. Siivola, T. Colpitts, and B. O'quinn, "Thin-film thermoelectric devices with high room-temperature figures of merit," *Nature*, vol. 413, no. 6856, p. 597, 2001.

[137] T. M. Tritt and M. Subramanian, "Thermoelectric materials, phenomena, and applications: a bird's eye view," *MRS bulletin*, vol. 31, no. 3, pp. 188–198, 2006.

[138] M. Zebarjadi, K. Esfarjani, M. Dresselhaus, Z. Ren, and G. Chen, "Perspectives on thermoelectrics: from fundamentals to device applications," *Energy & Environmental Science*, vol. 5, no. 1, pp. 5147–5162, 2012.

[139] L.-D. Zhao, V. P. Dravid, and M. G. Kanatzidis, "The panoscopic approach to high performance thermoelectrics," *Energy & Environmental Science*, vol. 7, no. 1, pp. 251–268, 2014.

[140] M. S. Dresselhaus, G. Chen, M. Y. Tang, R. Yang, H. Lee, D. Wang, Z. Ren, J.-P. Fleurial, and P. Gogna, "New directions for low-dimensional thermoelectric materials," *Advanced materials*, vol. 19, no. 8, pp. 1043–1053, 2007.

[141] B. Poudel, Q. Hao, Y. Ma, Y. Lan, A. Minnich, B. Yu, X. Yan, D. Wang, A. Muto, D. Vashaee, *et al.*, "High-thermoelectric performance of nanostructured bismuth antimony telluride bulk alloys," *Science*, vol. 320, no. 5876, pp. 634–638, 2008.

[142] A. Minnich, M. Dresselhaus, Z. Ren, and G. Chen, "Bulk nanostructured thermoelectric materials: current research and future prospects," *Energy & Environmental Science*, vol. 2, no. 5, pp. 466–479, 2009.

[143] C. J. Vineis, A. Shakouri, A. Majumdar, and M. G. Kanatzidis, "Nanostructured thermoelectrics: big efficiency gains from small features," *Advanced Materials*, vol. 22, no. 36, pp. 3970–3980, 2010.

[144] G. Joshi, H. Lee, Y. Lan, X. Wang, G. Zhu, D. Wang, R. W. Gould, D. C. Cuff, M. Y. Tang, M. S. Dresselhaus, *et al.*, "Enhanced thermoelectric figure-of-merit in nanostructured p-type silicon germanium bulk alloys," *Nano letters*, vol. 8, no. 12, pp. 4670–4674, 2008.

[145] Y. Pei, N. A. Heinz, A. LaLonde, and G. J. Snyder, "Combination of large nanostructures and complex band structure for high performance thermoelectric lead telluride," *Energy & Environmental Science*, vol. 4, no. 9, pp. 3640–3645, 2011.

[146] P. Vaqueiro and A. V. Powell, "Recent developments in nanostructured materials for high-performance thermoelectrics," *Journal of Materials Chemistry*, vol. 20, no. 43, pp. 9577–9584, 2010.

[147] W. Xie, J. He, H. J. Kang, X. Tang, S. Zhu, M. Laver, S. Wang, J. R. Copley, C. M. Brown, Q. Zhang, *et al.*, "Identifying the specific nanostructures responsible for the high thermoelectric performance of (bi, sb) 2te3 nanocomposites," *Nano letters*, vol. 10, no. 9, pp. 3283–3289, 2010.

[148] Y. Cao, X. Zhao, T. Zhu, X. Zhang, and J. Tu, "Syntheses and thermoelectric properties of bi 2 te 3/ sb 2 te 3 bulk nanocomposites with laminated nanostructure," *Applied Physics Letters*, vol. 92, no. 14, p. 143106, 2008.

[149] S. N. Guin, A. Chatterjee, D. S. Negi, R. Datta, and K. Biswas, "High thermoelectric performance in tellurium free p-type agsbse 2," *Energy & Environmental Science*, vol. 6, no. 9, pp. 2603–2608, 2013.

[150] P. F. Poudeu, J. D'Angelo, H. Kong, A. Downey, J. L. Short, R. Pcionek, T. P. Hogan, C. Uher, and M. G. Kanatzidis, "Nanostructures versus solid solutions: Low lattice thermal conductivity and enhanced thermoelectric figure of merit in pb9. 6sb0. 2te10-x se x bulk materials," *Journal of the American Chemical Society*, vol. 128, no. 44, pp. 14347–14355, 2006.

[151] K. Biswas, J. He, I. D. Blum, C.-I. Wu, T. P. Hogan, D. N. Seidman, V. P. Dravid, and M. G. Kanatzidis, "High-performance bulk thermoelectrics with all-scale hierarchical architectures," *Nature*, vol. 489, no. 7416, p. 414, 2012.

[152] H. Li, X. Tang, Q. Zhang, and C. Uher, "High performance in x ce y co 4 sb 12 thermoelectric materials with in situ forming nanostructured insb phase," *Applied Physics Letters*, vol. 94, no. 10, p. 102114, 2009.

[153] C. A. Paddock and G. L. Eesley, "Transient thermoreflectance from thin metal films," *Journal of Applied Physics*, vol. 60, no. 1, pp. 285–290, 1986.

[154] D. G. Cahill, K. Goodson, and A. Majumdar, "Thermometry and thermal transport in micro/nanoscale solid-state devices and structures," *Journal of Heat Transfer*, vol. 124, no. 2, pp. 223–241, 2002.

[155] J. Christofferson and A. Shakouri, "Thermoreflectance based thermal microscope," *Review of Scientific Instruments*, vol. 76, no. 2, p. 024903, 2005.

[156] S. Huxtable, D. G. Cahill, V. Fauconnier, J. O. White, and J.-C. Zhao, "Thermal conductivity imaging at micrometre-scale resolution for combinatorial studies of materials," *Nature Materials*, vol. 3, no. 5, p. 298, 2004.

[157] D. G. Cahill, "Analysis of heat flow in layered structures for time-domain thermoreflectance," *Review of scientific instruments*, vol. 75, no. 12, pp. 5119–5122, 2004.

[158] K. Hatori, N. Taketoshi, T. Baba, and H. Ohta, "Thermoreflectance technique to measure thermal effusivity distribution with high spatial resolution," *Review of scientific instruments*, vol. 76, no. 11, p. 114901, 2005.

[159] M. Nonnenmacher and H. Wickramasinghe, "Scanning probe microscopy of thermal conductivity and subsurface properties," *Applied Physics Letters*, vol. 61, no. 2, pp. 168–170, 1992.

[160] A. Majumdar, J. Carrejo, and J. Lai, "Thermal imaging using the atomic force microscope," *Applied Physics Letters*, vol. 62, no. 20, pp. 2501–2503, 1993.

[161] K. Luo, Z. Shi, J. Varesi, and A. Majumdar, "Sensor nanofabrication, performance, and conduction mechanisms in scanning thermal microscopy," *Journal of Vacuum Science & Technology B: Microelectronics and Nanometer Structures Processing, Measurement, and Phenomena*, vol. 15, no. 2, pp. 349–360, 1997.

[162] G. Mills, H. Zhou, A. Midha, L. Donaldson, and J. Weaver, "Scanning thermal microscopy using batch fabricated thermocouple probes," *Applied physics letters*, vol. 72, no. 22, pp. 2900–2902, 1998.

[163] G. B. M. Fiege, A. Altes, R. Heiderhoff, and L. J. Balk, "Quantitative thermal conductivity measurements with nanometre resolution," *Journal of Physics D: Applied Physics*, vol. 32, no. 5, p. L13, 1999.

[164] W. P. King, T. W. Kenny, K. E. Goodson, G. L. Cross, M. Despont, U. T. Durig, H. Rothuizen, G. Binnig, and P. Vettiger, "Design of atomic force microscope cantilevers for combined thermomechanical writing and thermal reading in array operation," *Journal of Microelectromechanical Systems*, vol. 11, no. 6, pp. 765–774, 2002.

[165] H.-K. Lyeo, A. Khajetoorians, L. Shi, K. P. Pipe, R. J. Ram, A. Shakouri, and C. Shih, "Profiling the thermoelectric power of semiconductor junctions with nanometer resolution," *Science*, vol. 303, no. 5659, pp. 816–818, 2004.

[166] K. Kim, W. Jeong, W. Lee, and P. Reddy, "Ultra-high vacuum scanning thermal microscopy for nanometer resolution quantitative thermometry," *Acs Nano*, vol. 6, no. 5, pp. 4248–4257, 2012.

[167] M. M. Rojo, J. Martín, S. Grauby, T. Borca-Tasciuc, S. Dilhaire, and M. Martin-Gonzalez, "Decrease in thermal conductivity in polymeric p3ht nanowires by size-reduction induced by crystal orientation: new approaches towards thermal transport engineering of organic materials," *Nanoscale*, vol. 6, no. 14, pp. 7858–7865, 2014.

[168] M. E. Pumarol, M. C. Rosamond, P. Tovee, M. C. Petty, D. A. Zeze, V. Falko, and O. V. Kolosov, "Direct nanoscale imaging of ballistic and diffusive thermal transport in graphene nanostructures," *Nano letters*, vol. 12, no. 6, pp. 2906–2911, 2012.

[169] S. Grauby, E. Puyoo, J.-M. Rampnoux, E. Rouviere, and S. Dilhaire, "Si and sige nanowires: fabrication process and thermal conductivity measurement by 3ω-scanning thermal microscopy," *The Journal of Physical Chemistry C*, vol. 117, no. 17, pp. 9025–9034, 2013.

[170] A. Majumdar, "Scanning Thermal Microscopy," *Annual Review of Materials Science*, vol. 29, pp. 505–585, aug 1999.

[171] C. C. Williams and H. K. Wickramasinghe, "Scanning thermal profiler," *Microelectronic Engineering*, vol. 5, no. 1-4, pp. 509–513, 1986.

[172] K. Zhao, H. Zeng, K. Xu, H. Yu, G. Li, J. Song, X. Shi, and L. Chen, "Scanning thermoelectric microscopy of local thermoelectric behaviors in (Bi,Sb)2Te3films," *Physica B: Condensed Matter*, vol. 457, pp. 156–159, 2015.

[173] W. P. King, T. W. Kenny, K. E. Goodson, G. Cross, M. Despont, U. Dürig, H. Rothuizen, G. K. Binnig, and P. Vettiger, "Atomic force microscope cantilevers for combined thermomechanical data writing and reading," *Applied Physics Letters*, vol. 78, no. 9, pp. 1300–1302, 2001.

[174] B. Chui, T. Stowe, T. Kenny, H. Mamin, B. Terris, and D. Rugar, "Low-stiffness silicon cantilevers for thermal writing and piezoresistive readback with the atomic force microscope," *Applied Physics Letters*, vol. 69, no. 18, pp. 2767–2769, 1996.

[175] P. Vettiger, G. Cross, M. Despont, U. Drechsler, U. Durig, B. Gotsmann, W. Haberle, M. Lantz, H. Rothuizen, R. Stutz, *et al.*, "The" millipede"-nanotechnology entering data storage," *IEEE Transactions on nanotechnology*, vol. 99, no. 1, pp. 39–55, 2002.

[176] S. Lefèvre, S. Volz, J. B. Saulnier, C. Fuentes, and N. Trannoy, "Thermal conductivity calibration for hot wire based dc scanning thermal microscopy," *Review of Scientific Instruments*, vol. 74, no. 4, pp. 2418–2423, 2003.

[177] L. Shi and A. Majumdar, "Thermal Transport Mechanisms at Nanoscale Point Contacts," *Journal of Heat Transfer*, vol. 124, no. 2, p. 329, 2002.

[178] M. Hinz, O. Marti, B. Gotsmann, M. Lantz, and U. Dürig, "High resolution vacuum scanning thermal microscopy of hf o 2 and si o 2," *Applied Physics Letters*, vol. 92, no. 4, p. 043122, 2008.

[179] Y. Zhang, C. L. Hapenciuc, E. E. Castillo, T. Borca-Tasciuc, R. J. Mehta, C. Karthik, and G. Ramanath, "A microprobe technique for simultaneously measuring thermal conductivity and seebeck coefficient of thin films," *Applied Physics Letters*, vol. 96, no. 6, p. 062107, 2010.

[180] E. T. Swartz and R. O. Pohl, "Thermal boundary resistance," *Reviews of modern physics*, vol. 61, no. 3, p. 605, 1989.

[181] W. P. King, B. Bhatia, J. R. Felts, H. J. Kim, B. Kwon, B. Lee, S. Somnath, and M. Rosenberger, "Heated Atomic Force Microscope Cantilevers and Their Applications," *Annual Review of Heat Transfer*, vol. 16, no. 1, pp. 287–326, 2013.

[182] X. Zhao, X. Shi, L. Chen, W. Zhang, S. Bai, Y. Pei, X. Li, and T. Goto, "Synthesis of yb y co 4 sb 12/ yb 2 o 3 composites and their thermoelectric properties," *Applied physics letters*, vol. 89, no. 9, p. 092121, 2006.

[183] T. Dahal, Q. Jie, G. Joshi, S. Chen, C. Guo, Y. Lan, and Z. Ren, "Thermoelectric property enhancement in yb-doped n-type skutterudites ybxco4sb12," *Acta Materialia*, vol. 75, pp. 316–321, 2014.

[184] S. Wang, J. R. Salvador, J. Yang, P. Wei, B. Duan, and J. Yang, "High-performance n-type yb x co 4 sb 12: from partially filled skutterudites towards composite thermoelectrics," *NPG Asia Materials*, vol. 8, no. 7, p. e285, 2016.

[185] Y. Tang, S.-w. Chen, and G. J. Snyder, "Temperature dependent solubility of yb in yb–cosb 3 skutterudite and its effect on preparation, optimization and lifetime of thermoelectrics," *Journal of Materiomics*, vol. 1, no. 1, pp. 75–84, 2015.

[186] T. Caillat, "Preparation and thermoelectric properties of ir x co 1-x sb 2 alloys," 1995.

[187] H. Lal and K. Gaur, "Electrical conduction in non-metallic rare-earth solids," *Journal of materials science*, vol. 23, no. 3, pp. 919–923, 1988.

[188] M. H. Shamos and L. S. Lavine, "Piezoelectricity as a fundamental property of biological tissues," *Nature*, vol. 213, no. 5073, p. 267, 1967.

[189] S. V. Kalinin, B. J. Rodriguez, S. Jesse, E. Karapetian, B. Mirman, E. A. Eliseev, and A. N. Morozovska, "Nanoscale electromechanics of ferroelectric and biological systems: a new dimension in scanning probe microscopy," *Annu. Rev. Mater. Res.*, vol. 37, pp. 189–238, 2007.

[190] W. A. Catterall, "Structure and function of voltage-gated ion channels," *Annual review of biochemistry*, vol. 64, no. 1, pp. 493–531, 1995.

[191] L. Cross, S. Jang, R. Newnham, S. Nomura, and K. Uchino, "Large electrostrictive effects in relaxor ferroelectrics," *Ferroelectrics*, vol. 23, no. 1, pp. 187–191, 1980.

[192] L. Li, Y. Cao, S. Somnath, Y. Yang, S. Jesse, Y. Ehara, H. Funakubo, L.-Q. Chen, S. V. Kalinin, and R. K. Vasudevan, "Direct imaging of the relaxation of individual ferroelectric interfaces in a tensile-strained film," *Advanced Electronic Materials*, vol. 3, no. 4, 2017.

[193] E. Strelcov, Y. Kim, J. Yang, Y. Chu, P. Yu, X. Lu, S. Jesse, and S. Kalinin, "Role of measurement voltage on hysteresis loop shape in piezoresponse force microscopy," *Applied Physics Letters*, vol. 101, no. 19, p. 192902, 2012.

[194] J. J. F. Li, J. J. F. Li, Q. Yu, Q. N. Chen, and S. Xie, "Strain-based scanning probe microscopies for functional materials, biological structures, and electrochemical systems," *Journal of Materiomics*, vol. 1, pp. 3–21, mar 2015.

[195] S. Hong, S. Tong, W. I. Park, Y. Hiranaga, Y. Cho, and A. Roelofs, "Charge gradient microscopy," *Proceedings of the National Academy of Sciences*, vol. 111, no. 18, pp. 6566–6569, 2014.

[196] Y.-Y. Choi, S. Tong, S. Ducharme, A. Roelofs, and S. Hong, "Charge collection kinetics on ferroelectric polymer surface using charge gradient microscopy," *Scientific Reports*, vol. 6, no. 1, p. 25087, 2016.

[197] S. Tong, I. W. Jung, Y. Y. Choi, S. Hong, and A. Roelofs, "Imaging Ferroelectric Domains and Domain Walls Using Charge Gradient Microscopy: Role of Screening Charges," *ACS Nano*, vol. 10, no. 2, pp. 2568–2574, 2016.

[198] R. S. Weis and T. K. Gaylord, "Lithium niobate: Summary of physical properties and crystal structure," *Applied Physics A Solids and Surfaces*, vol. 37, no. 4, pp. 191–203, 1985.

[199] V. Gopalan, T. E. Mitchell, Y. Furukawa, and K. Kitamura, "The role of nonstoichiometry in 180 domain switching of linbo 3 crystals," *Applied Physics Letters*, vol. 72, no. 16, pp. 1981–1983, 1998.

[200] Y.-Q. Lu, Z.-L. Wan, Q. Wang, Y.-X. Xi, and N.-B. Ming, "Electro-optic effect of periodically poled optical superlattice linbo 3 and its applications," *Applied Physics Letters*, vol. 77, no. 23, pp. 3719–3721, 2000.

[201] L. Myers, W. Bosenberg, G. Miller, R. Eckardt, M. Fejer, and R. Byer, "Quasi-phase-matched 1.064-μm-pumped optical parametric oscillator in bulk periodically poled linbo 3," *Optics letters*, vol. 20, no. 1, pp. 52–54, 1995.

[202] S. Hong, O. Auciello, and D. Wouters, *Emerging non-volatile memories*. Springer, 2014.

[203] X. Ma and G.-S. Kuo, "Optical switching technology comparison: optical mems vs. other technologies," *IEEE communications magazine*, vol. 41, no. 11, pp. S16–S23, 2003.

[204] S. Hong, S. M. Nakhmanson, and D. D. Fong, "Screening mechanisms at polar oxide heterointerfaces," *Reports on Progress in Physics*, vol. 79, no. 7, p. 076501, 2016.

[205] S. Jesse, B. Mirman, and S. V. Kalinin, "Resonance enhancement in piezoresponse force microscopy: Mapping electromechanical activity, contact stiffness, and Q factor," *Applied Physics Letters*, vol. 89, no. 2, 2006.

[206] H. Bo, Y. Kan, X. Lu, Y. Liu, S. Peng, X. Wang, W. Cai, R. Xue, and J. Zhu, "Drive frequency dependent phase imaging in piezoresponse force microscopy," *Journal of Applied Physics*, vol. 108, no. 4, p. 042003, 2010.

[207] C. Harnagea, A. Pignolet, M. Alexe, D. Hesse, and U. Gösele, "Quantitative ferroelectric characterization of single submicron grains in bi-layered perovskite thin films," *Applied Physics A*, vol. 70, no. 3, pp. 261–267, 2000.

[208] Q. N. Chen, S. B. Adler, and J. Li, "Imaging space charge regions in Sm-doped ceria using electrochemical strain microscopy," *Applied Physics Letters*, vol. 105, p. 201602, nov 2014.

[209] M. Schröder, A. Haußmann, A. Thiessen, E. Soergel, T. Woike, and L. M. Eng, "Conducting domain walls in lithium niobate single crystals," *Advanced Functional Materials*, vol. 22, no. 18, pp. 3936–3944, 2012.

[210] J. L. Proctor, S. L. Brunton, and J. N. Kutz, "Dynamic mode decomposition with control," *SIAM Journal on Applied Dynamical Systems*, vol. 15, pp. 142–161, jan 2014.

[211] A. Labuda and R. Proksch, "Quantitative measurements of electromechanical response with a combined optical beam and interferometric atomic force microscope," *Applied Physics Letters*, vol. 106, p. 253103, jun 2015.

[212] S. Lefèvre and S. Volz, "3 ω-scanning thermal microscope," *Review of scientific instruments*, vol. 76, no. 3, p. 033701, 2005.